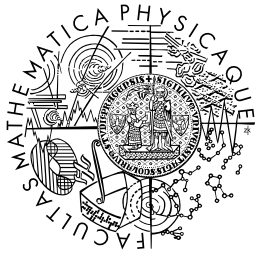

FACULTY
OF MATHEMATICS
AND PHYSICS
Charles University

MASTER THESIS

Bc. Marcel Lamač

Laser-driven hard X-ray source for imaging applications

Department of Chemical Physics and Optics

Supervisor of the master thesis: Ing. Jaroslav Nejdl, Ph.D.
Study programme: Physics
Study branch: Optics and Optoelectronics

Prague 2020

I declare that I carried out this master thesis independently, and only with the cited sources, literature and other professional sources. It has not been used to obtain another or the same degree.

I understand that my work relates to the rights and obligations under the Act No. 121/2000 Sb., the Copyright Act, as amended, in particular the fact that the Charles University has the right to conclude a license agreement on the use of this work as a school work pursuant to Section 60 subsection 1 of the Copyright Act.

In ..... date ....

Author's signature

Acknowledgement

I would like to express immense gratitude to both my supervisor Jaroslav Nejdl and consultant Uddhab Chaulagain, who have both guided and advised me at each step of the process of writing this thesis. Secondly, I would like to thank dearly Tomáš Kerepecký for his work on the radiation calculation code, without which the scope of this thesis would be much more limited. I also wish to thank all my colleagues from RP2 X-ray group at ELI-Beamlines, for providing family like friendly work environment in which it was a delight to work. Lastly, I would like to thank my family and friends, who were always supporting me.

This work is supported by Advanced research using high intensity laser produced photons and particles (reg. no. CZ.02.1.01/0.0/0.0/16019/0000789) from European Regional Development Fund (ADONIS) and from European Regional Development Fund and the project LQ1606, obtained with the financial support of the Ministry of Education, Youth and Sports as part of targeted support from the National Programme of Sustainability II.

To my family

Title: Laser-driven hard X-ray source for imaging applications

Author: Bc. Marcel Lamač

Department: Department of Chemical Physics and Optics

Supervisor: Ing. Jaroslav Nejdl, Ph.D., ELI Beamlines, Institute of Physics of the Czech Academy of Sciences

Consultant: Uddhab Chaulagain, Ph.D., ELI Beamlines, Institute of Physics of the Czech Academy of Sciences

Abstract: With the advent of high-power lasers in recent decades, a unique source of hard X-ray radiation has become availible. This source of collimated, broadband, femtosecond, incoherent and hard X-ray radiation is produced when a focused laser with intensity above 10^{18} W/cm^2 collides with a gas target. The strong electric field of the laser pulse ionizes the gas and interacts with the plasma generating a strong plasma wake wave. This space charge separation inside the target generates longitudal electric fields of the order of 100 GV/m. This resulting electrostatic wakefield accelerates the electrons to relativistic velocities and causes them to travel in oscillatory motion behind the laser pulse, producing hard and collimated X-ray radiation. This thesis is focused on a theoretical evaluation and an experimental design of this laser-plasma X-ray source. Furthermore, we consider the source's unique properties for novel imaging applications.

Keywords: wakefield acceleration x-ray radiation imaging

Contents

Introduction

The physics community celebrated a massive success in the now illustrious experimental confirmation of the Higgs' boson in 2012 by the ATLAS Collaboration [1]. Apart from providing yet another validation of the Standard Model of particle physics, this widely celebrated success showcased to the world the state-of-the-art technological maturity and the particle accelerating capabilities of the *Large Hadron Collider*. In past years, particle accelerators were mostly presented to the general public as a tool for studying the most fundamental questions regarding our universe, such as it's history and evolution, or the elementary structure of mass, energy, space and their various interactions.

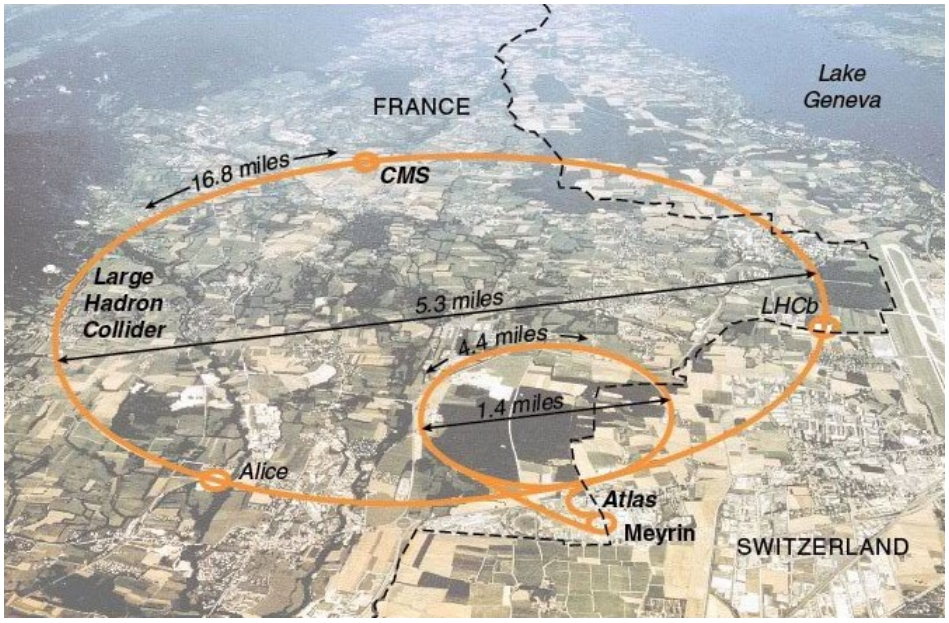

Figure 1: The scale of Large Hadron Collider in Geneva. Reproduced from the website of Dr. Helen Klus *thestargarden.co.uk*

Apart from these worthy goals, it might not be that clear to the general public, thanks to such publicity, that almost all accelerators in operation around the world are used for many other fields, some quite different from high energy physics, such as materials science, biological research, chemistry, oncology, medical imaging, radiotherapy, nuclear power and many more [2]. In fact, it wouldn't be too big of a stretch to say that most people have in some way interacted with a particle accelerator, notably when being irradiated by conventional medical X-ray machines. In many of the applications of particle acceleration in these fields, the electromagnetic radiation resulting from the particle's motion is the desired product, not the particles themselves.

When we look more than a century back in history, it is also quite clear that X-ray radiation has been interwoven with particle acceleration since it's accidental discovery in 1895 by W. C. Röntgen [3]. He noticed during his experiments with *a Crookes tube*, evacuated glass tube with electrodes encapsulated within, that fluorescent green glow was being emitted from an accidentally placed board covered with phosphorus a meter away. This persistent glow lasted even after

he covered the cathode ray emitting tube with a heavy black paper, covering it's ghastly glow. To his surprise, the board was still emitting a fluorescent glow while tube was in operation even though, as he presumed, cathode rays couldn't leave the tube. This accidental 1901 Nobel Prize winning discovery was followed by a flurry of similar experimentation, one of which his wife was involved in, resulting in the following historically first medical X-ray.

Figure 2: Medical X-ray of Mrs. Röntgen's hand. Reproduced from *commons.wikimedia.org*

As we understand now, these luminiscent tubes are, in fact, nothing but small particle accelerators. The residual gas in the evacuated glass tube is ionized due to high enough voltage being present, which results in the electrons being accelerated towards the anode. Upon collision with the anode, bremsstrahlung and electroluminiscent radiation characteristic of the anode material is emitted. Modern high vacuum X-ray tubes operate on a similar principle. The electrons are however generated not by gas ionization, but through thermionic emission from a tungsten cathode, which is heated up to 2000 K, more recent designs also include a rotating anode which provides improved cooling in continuous operation. High vacuum in these tubes is necessary to reduce the detrimental effect the neutral and ionized gas atoms would have on the propagation of the electrons emitted from the cathode, as shown by W. Coolidge in his pioneering work [4]. The decades following Röntgen's discovery were characterized by continous research and development of X-ray tubes providing a reliable scientific instrument for generations to follow.

In the year 1944, a couple of russian scientists named Iwanenko and Pomeranchuk predicted a new limitation in the form of generated radiation on the recently conceived accelerator *Betatron*, *"Indeed, electrons moving in a magnetic field will be accelerated and must radiate in accordance with the classical electrodynamics."* [5] These theoretical predictions followed R. Widerøe's realization of the first radio-frequency linear accelerator in 1928 [6], which further motivated new accelerator concepts, like E. Lawrence's 1929 *Cyclotron*, patented in 1932 [7], and *Betatron*, which was succesfully realized by D. Kerst in 1940 [8].

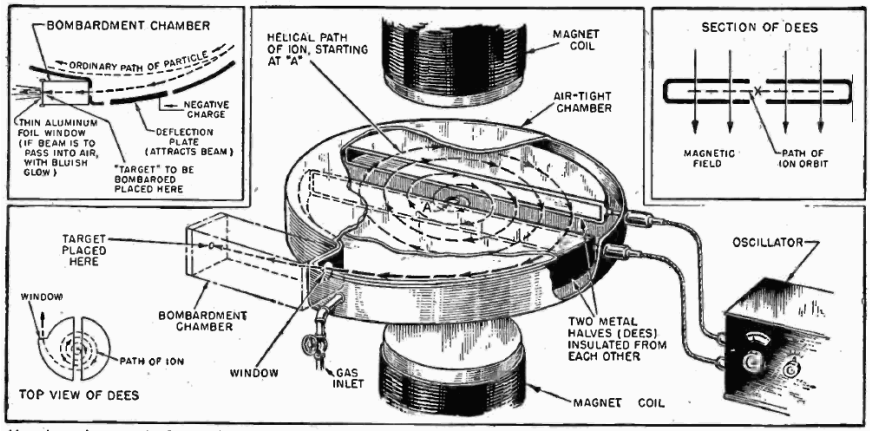

(a) Diagram of Lawrence's Cyclotron. Retrieved from [9]

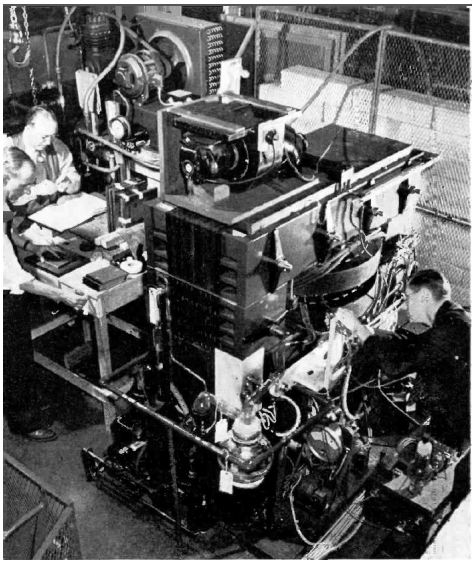

(b) Betatron at the U. of Illinois. D. Kerst at the right examining vacuum chamber between the 4-ton magnet. Retrieved from [10]

Figure 3: Accelerators of the first half of the 20th century.

These accelerators allowed scientists to observe particles with energies previously unreached. The *Cyclotron* utilized high frequency alternating voltage and a constant perpendicular magnetic field to keep particles on a outward spiralling orbit during acceleration. This concept was more cost and space effective compared to previous linear accelerators. However, due to the limitations on the magnetic fields at the time availible, the accelerated ion energy was limited to few MeVs. Therefore, more energetic ions simply could not be kept on this outward spiral trajectory. The *Betatron*, essentialy a transformer, utilized changing magnetic field in the core due to "primary coil" to generate tangential electric field in the "secondary coil" - a toroidal vacuum tube. This resulted in circling motion of electrons in the vacuum torus, which were injected into it once again from thermionic emission. These relativistic electrons were then made to strike a tungsten rod, generating X-rays.

In 1944 and 1945, the *Synchrotron* concept was independently invented by V. Veksler [11] and E. McMillan [12], the latter of which managed to construct a first operational machine in 1945. This accelerator is essentially a hybrid of the ones previously mentioned. The synchrotron utilizes accelerating radio frequency field and alternating magnetic field synchronized to the increasing energy of the particles to guide them and keep them on a stable orbital trajectory. This allows the vacuum chamber containing the particles to be of a thin toroidal shape, instead of a disk as in cyclotron. The key principle is that unlike the cyclotron, synchrotrons cannot accelerate particles from rest due to their toroidal shape and therefore alredy relativistic particles in phase with the accelerating radio-frequency field need to be injected into the rings for acceleration to happen.

In the same year of 1945, another pivotal study on the accelerator radiation generation was produced in preprint form by J. Schwinger and distributed only to few selected colleagues [13], the full work was however published in 1949 [14]. In this work he concludes, after the analysis of an electron moving in an alternating magnetic field, *"Hence the betatron is a source of visible radiation, rather than ultra-high frequency radio waves."* This first step in the validation of synchrotrons as viable lightsources, at the time considered only limitations on particle energy gain by most, was confirmed in the historic discovery of synchrotron radiation in the visible spectral region by F. R. Elder et al. in 1947 [15] using the prototype General Electric 70 MeV synchrotron.

National Bereau of Standards comissioned Synchrotron Ulatrivolet Radiation Facility (SURF) in 1961, starting the age of 1st generation synchrotrons. Deutsches Elektronen-Synchrotron (DESY) in Hamburg produced 6 GeV electrons in 1964 and the radiation wavelength barrier of 0.1 Å was broken. This synchrotron generation was marked by the fact that they were operated as sources of both high energy particles and radiation. The emergance of 2nd generation synchrotrons begun in 1970 with the comissioning of Synchrotron Radiation Source (SRS) in Daresbury Laboratory, United Kingdom. These resulted in operational shift, since the synchrotrons were now operated as dedicated sources of high energy radiation. The 3rd generation synchrotron lightsources emerged with the first installation of undulator for radiation generation in 1970 on the synchrotron in Lebedev Institute in Moscow. Modern synchrotron light sources currently in operation are 3rd generation facilities utilizing insertion devices.

Another paradigm shift came with the theoretical prediction by J. M. Madey in 1971 [16], when he theoretically described a device that is essentially a linear accelerator with a very long undulator. The big size of the undulator allows for longer emission of radiation, which in turn spatially modulates the emitting electron bunch, producing microbunches separated by wavelength of the radiation. This turns the radiation generation into a fully coherent process which causes the intensity of the radiation to scale as a square of the number of radiating electrons, dramatically increasing it's power output. The device was named Free Electron Laser (FEL). In 1997, first free electron laser was realized at Stanford University beginning the age of 4rd generation light sources. Since then, many other accelerators and FELs were developed, notably LCLS in Stanford, European XFEL in Hamburg, LHC in Geneva and many more. Figures 4 and 5 showcase the dramatic evolution X-ray sources underwent during the 20th century.

(a) European Synchrotron Radiation Facility (ESRF) in Grenoble, France. Perimeter of the storage ring is 844 m.

(b) European X-Ray Free Electron Laser (XFEL) in Hamburg. Length roughly 3 km.

Figure 4: Contemporary accelerators. Source *xfel.desy.de*

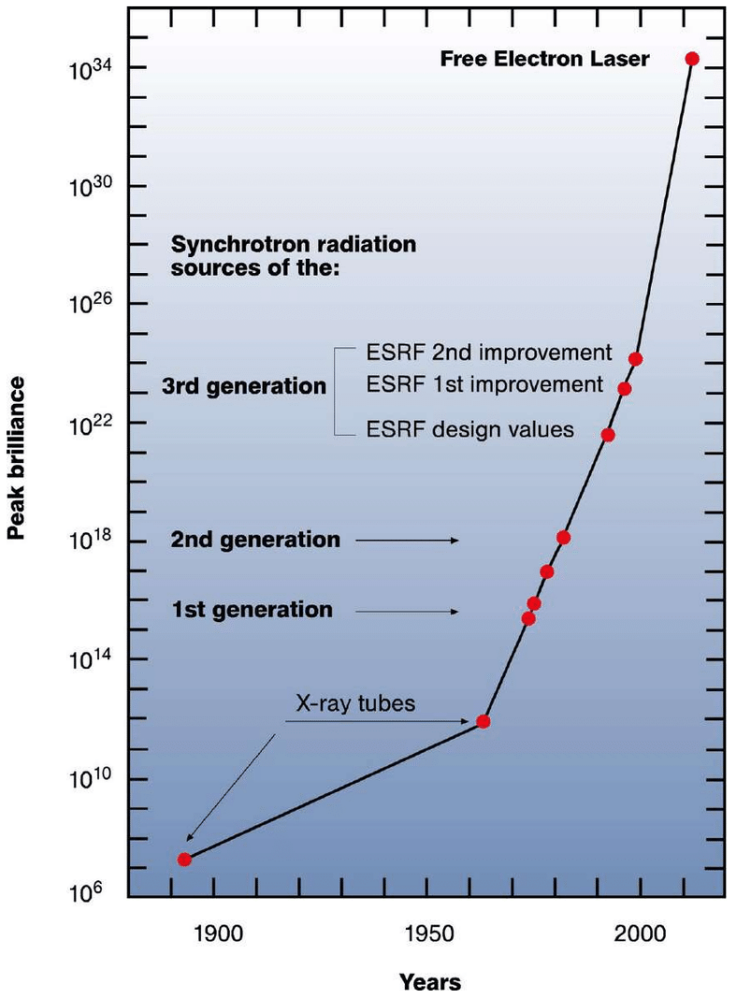

Figure 5: Evolution of peak brilliance of X-ray sources over the years. In units of photons/s·mrad^2·mm^2·0.1%BW. Source *xfel.desy.de*

In the introduction so far, we've been trying to highlight the tight bond between accelerators and radiation sources throughout the history of last century and today. The kind reader might have also noticed the enormous scale of contemporary facilities shown in Fig. 4. This large size doesn't come without reason, which is two-fold.

The first principal problem of accelerators arises because state-of-the-art facilities like the XFEL or LHC utilize accelerating electric fields provided by evacuated niobium radio-frequency (RF) cavities made to resonate with RF field in the GHz range, which is produced by RF antennas inside the cavity. State-of-the-art RF cavities are able to sustain electrical gradients of less than $\sim$ 50 MV/m (15 MV/m in normal operation), because increasing the voltage induces electrical breakdown of the RF cavity walls through field emission, permanently damaging the cavities. This forces the accelerator to be $\sim$ 100s of meters long for particles to reach $\sim$ GeV energies [17].

The second reason is more specific to light-source facilities like Synchrotrons and FELs. Magnets in insertion devices like undulators cannot be manufactured arbitrarily small and usually provide minimum magnet period in milimeters. Achieving more electron oscillations is therefore possible once again only through length increase of the undulator. It would seem that the way towards higher brilliance and particle energies lies in increasing the length of the accelerators, a notable example being LHC, XFEL or the International Linear Collider (ILC), which will be 10s of km long with estimated costs reaching 20 billion Euro.

A New Way through Plasma

The issue of electrical breakdown can be avoided by using plasma as the accelerating medium, since it is alredy electrically broken down to it's charged constituents. This idea was first conceived by V. I. Veksler in 1956 [18] with following research on acceleration of charged particles by Ya. B. Fainberg in 1967 [19]. The two key steps of plasma acceleration are to ionize neutral gas and then create large accelerating electric gradient through separation of electrons and ions.

In 1979, Tajima and Dawson proposed an all-optical scheme of plasma acceleration through their "Laser Electron Accelerator" [20]. Their simplified scheme combined the previous two steps into one. Ionization and charge separation of electrons and ions were envisioned by an intense laser pulse exceeding 10^{18} W/cm^2, yielding accelerating gradients of $\sim$ 100s GV/m, four orders of magnitude higher than conventional RF accelerators. Such accelerator could effectively shrink the accelerating distance necessary to boost electrons to GeV energy range to milimeters, dramatically reducing the costs and size demands of new accelerators at the same time. This concept is today called *Laser Wakefield Acceleration* (LWFA) and has been extensively studied both theoretically and experimentally in the last two decades. Newest research at the time of writing reports 60 pC quasimonoenergetic electron beams with 8 GeV energies within 0.5 mrad x 0.5 mrad divergence achieved with petawatt-class laser systems [21].

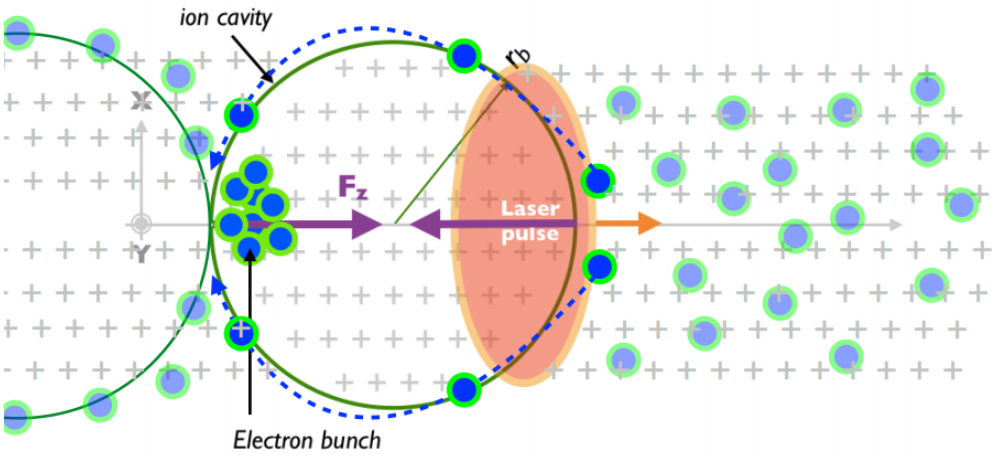

Figure 6: Schematic of LWFA. Intense laser pulse ionizes the neutral gas at the front edge and ponderomotive force pushes the electrons away while heavy ions stay immobile. This plasma generated "wakefield" accelerates electrons caught in it. Source *Corde et al. RMP 85.1 (2013).*

The historical pact between accelerators and novel radiation sources revealed itself once again in the case of LWFA, when in 2004 a breakthrough was achieved in ultrashort X-ray generation. A. Rousse measured ultrafast synchrotron-like X-ray pulses being generated from the inside of the plasma bubble [22]. This was named *Betatron X-ray radiation* due to the similarity of the nature of it's generation, which is oscillatory motion of the electrons throughout their propagation, to the Betatron (fig. 3). Extensive research followed [23] [24] [25] and continues, with latest reports of femtosecond X-ray flashes with peak brightness of 10^{22-23} photons/s/mm^2/mrad^2/0.1% BW [26] rivaling 3rd generation Synchrotron facilites and opening the possibility for all-optical, spatially coherent and Synchrotron-like facilities with femtosecond time-resolution capabilities for fraction of the cost.

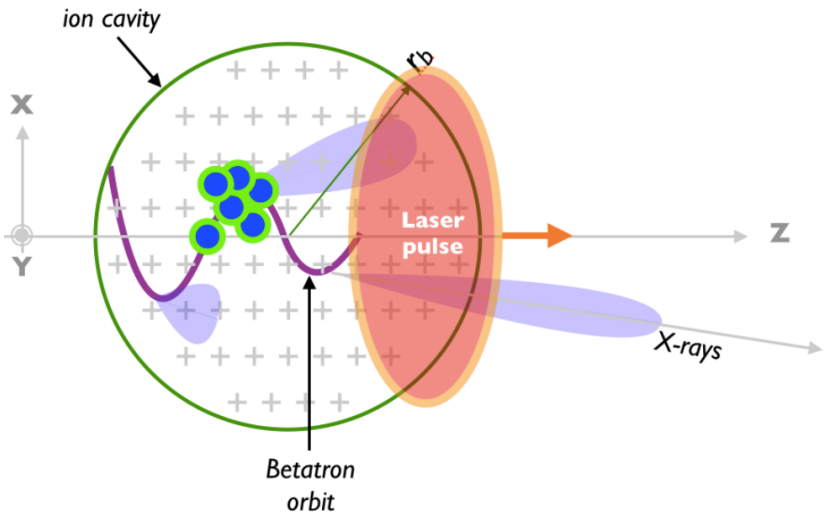

Figure 7: Schematic of Betatron X-ray radiation. Electrons with transverse momentum get injected into the accelerating phase of the wakefield, resulting in Betatron oscillations due to the radial electric field inside the ion cavity. Source *Corde et al. RMP 85.1 (2013).*

Thesis Outline

In **Chapter 1**, we will present a theoretical summary of LWFA descending from relativstic electrodynamics. **Chapter 2** will present theory explaining the mechanisms behind radiation generation from relativistic electrons. In **Chapter 3**, we will present numerical methods used for laser-plasma interactions and my work on the development of radiation post-processing routines, which allowed me to obtain numerical results used for theoretical support of the experiments. In **Chapter 4**, we will present experimental design and setup, which I was a part of, for an upcoming Betatron X-ray generation experiment with the L3 petawatt-class laser system at ELI Beamlines, Prague. In the last **Chapter 5**, we will provide a summary of various X-ray imaging applications and consider their feasibility when employed with the Betatron X-ray source.

Role of the Author

The role of the author was to theoretically and numerically investigate laser produced Betatron X-ray sources, become part of the experimental design, and find out whether these X-ray sources are suitable for imaging applications. I have done a thorough research of availible literature, compiled and recasted parts of the availible theory in fashion which I hope is a bit more lucid and modern. I have mainly conducted numerical simulations investigating laser-plasma interactions and co-developed radiation post-processing and data visualization routines which allow for theoretical analysis and wider understanding of the underlying processes in the laser-plasma interactions and radiation generation during the experiment. I have been part of the design of the experimental setup inside the P3 interaction chamber at ELI Beamlines, notably I've designed and set up the in-vacuum gas supply for the gas jet target and electron charge and energy diagnostics. These results are presented in **Chapter 3** and **4**. In **Chapter 5**, I have summarized imaging methods and estimated their feasibility with the Betatron X-ray source.

1. Laser Wakefield Acceleration

The dynamics involved in LWFA force relativistic velocities upon the accelerated particles. For this reason, relativistic mechanics have to be considered for complete description of the phenomenon. In this chapter, we will attempt to summarize physical theory describing LWFA, often in a fashion naturally manifesting Lorentz covariance. This approach will include relativistic effects affecting the dynamics and showcase possible generalizations into the realm of quantum electrodynamics (QED), which is increasingly relevant in modern facilities and non-trivially alters the dynamics in laser-plasma interactions in many experimental schemes. Some exceptions will be made to improve lucidity of the presented theory to the kind reader. Most of the work in this chapter is a compilation of availible literature, often with some modifications. In the first part, we will familiarize ourselves with the emergance of relativistic mechanics from first principles, and then proceed to describe the relevant physics involved in laser-plasma interactions. At the end of the chapter, we will thoroughly discuss the various methods of electron injection into the accelerating phase of the wakefield, which was experimentally shown to be the the most important way of influencing energies achieved by particles accelerated through plasma wakefields [27].

1.1 Relativistic Electrodynamics

The guiding principles of physical theories in the last century have, among few others, proven to be the postulates of theories of special and general relativity by A. Einstein. We will consider only the special case, since the gravitational forces can be generously neglected compared to the strengths of electromagnetic fields involved. This leaves us with the assumptions of the existence of physically equivalent inertial reference frames and the finite and Lorentz invariant speed of light, which will simplify some calculations later on. The dynamics of the evolution of physical system satisfying previous postulates are then invoked mathematically through Hamilton's principle of stationary action, which dictates that for a given physical system, only such evolution is physically realized whose action is extremalized. Mathematically speaking

$$\boxed{\delta S = 0} \tag{1.1}$$

where the action of the system S is defined as the functional

$$S = \int_{\tau_i}^{\tau_f} \mathcal{L}(q^\mu, \dot{q}^\mu, \tau)\mathbf{d}\tau \tag{1.2}$$

where the Lagrangian $\mathcal{L}$ with dimension of energy is integrated with respect to proper time between fixed end points τ_f and τ_i. q^μ and $\dot{q}^\mu$ are respectively the configuration coordinate and it's proper time τ derivative. The logical conjunction of previously mentioned postulates forces the action to be Lorentz invariant,

otherwise the dynamics of the system would change with respect to different inertial reference frames, negating our postulates.

In classical mechanics, Lagrangian is defined to be the difference of kinetic and potential energy $T - V$. However, if we consider relativistic postulates, we have to be a bit more careful. Kinetic energy can be different depending on the choice of inertial reference frame. This forces us to describe our physical system only by Lorentz invariant Lagrangians, since proper time is alredy invariant. The necessary condition for the extremalization of action is then expressed through the Euler-Lagrange (E-L) equations

$$\boxed{\frac{\partial \mathcal{L}}{\partial q^\mu} - \frac{\mathbf{d}}{\mathbf{d}\tau}\left(\frac{\partial \mathcal{L}}{\partial \dot{q}^\mu}\right) = 0} \tag{1.3}$$

Where we didn't consider any dynamical constraints and made an assumption of $\delta \mathbf{d}\tau = 0$, which is justified in Appendix A.1. The construction of manifestly covariant theory describing relativistic electrodynamics then demands that we find possible Lorentz invariant Lagrangians.

First, we define the principal quantities which describe electrodynamics. The fields are prescribed through the four-potential A^μ and sources through the four-current J^μ as

$$A^\mu = \left(\frac{\phi}{c}, \boldsymbol{A}\right) \tag{1.4}$$

$$J^\mu = (\rho c, \boldsymbol{j}) = \frac{\rho}{\gamma}\gamma\,(c, \boldsymbol{v}) = \frac{\rho}{\gamma}\dot{x}^\mu = \rho_0 u^\mu \tag{1.5}$$

where ϕ is the electric potential, $\boldsymbol{A}$ is the magnetic vector potential, c is the speed of light in vacuum, ρ is the charge density, $\boldsymbol{j}$ is the current density, $\gamma = 1/\sqrt{1 - \frac{v^2}{c^2}}$ is the Lorentz factor, $\boldsymbol{v}$ is velocity and $x^\mu = (ct, \boldsymbol{x})$ and $u^\mu = (\gamma c, \gamma \boldsymbol{v})$ are the four-position and four-velocity respectively. The observable fields are given by the electromagnetic tensor $F_{\mu\nu}$ defined through the antisymmetric differentiation of the four-potential

$$F_{\mu\nu} = \partial_\mu A_\nu - \partial_\nu A_\mu = \begin{pmatrix} 0 & -E_x/c & -E_y/c & -E_z/c \\ E_x/c & 0 & B^z & -B^y \\ E_y/c & -B^z & 0 & B^x \\ E_z/c & B^y & -B^x & 0 \end{pmatrix} \tag{1.6}$$

where $\boldsymbol{E} = -\partial \boldsymbol{A}/\partial t - \nabla\phi$ is the electric field strength and $\boldsymbol{B} = \nabla \times \boldsymbol{A}$ is the magnetic flux density. A more complete discussion of the following lies in Appendix A.2. The Lagrangian describing the dynamics of the fields is selected by the criterion of Lorentz invariance, which simply means that all the terms it contains must necessarily be Lorentz invariant. Since Lagrangian has the dimension of energy, we must select only those invariant combinations of $(A^\mu, J^\mu, F^{\mu\nu})$, whose dimension is the same. If we check the dimension of these quantities, we find that the only non-vanishing unique scalars are $F^{\mu\nu}F_{\mu\nu}$ and $J^\mu A_\mu$. We also note that throughout this whole thesis we are using Einstein's summation convention. We can see that the first quantity describes only the free fields and the

second couples the fields to the sources. We can therefore recognize the correct *Lagrangian density* describing relativistic electrodynamics as sum of a free term and an interaction term

$$\mathcal{L} = \mathcal{L}_{fields} + \mathcal{L}_{int} = -\frac{1}{4\mu} F^{\mu\nu} F_{\mu\nu} + J^{\mu} A_{\mu} \tag{1.7}$$

where the vaccum permeability μ was added for correct dimensionality of the Lagrangian *density*. Once again, we guide the kind reader towards Appendix A.2 for a more thorough approach of the following result. A correct extremalization of the action or the application of equations (1.3) leads to the covariant formulation of Maxwell's equations of electrodynamics

$$\boxed{\partial_{\mu} F^{\mu\nu} = \mu J^{\nu}} \tag{1.8}$$

$$\boxed{F_{[\mu\nu,\rho]} = 0} \tag{1.9}$$

where the two Maxwell's equations with sources (1.8) follow from (1.3). The other two source-less equations (1.9) are fulfilled automatically thanks to the definition of the electromagnetic tensor (1.6). From the theory built so far, we can model the behaviour of fields in the presence of sources, but Maxwell's equations alone aren't complete for the full dynamical description, since we also need to model the behaviour of sources in the presence of fields. We will once again rely on Hamilton's principle to derive correct mechanics. Since we alredy identified the term that is responsible for the interaction of matter and fields $\mathcal{L}_{int} = J^{\mu} A_{\mu}$, we only need to find the correct Lagrangian of free matter. We will focus on the special case where we only consider a point charged particle. In Appendix A.3, we present to the kind reader that there exists a most trivial choice which requires a slightly more complete treatment of (1.1) than previously presented. This allows the Lagrangian of a free particle to be intuitively chosen as $\mathcal{L}_{matter} = -m_0 c^2$, which gives the Lagrangian of a particle interacting with electromagnetic fields as

$$\mathcal{L} = \mathcal{L}_{matter} + \mathcal{L}_{int} = -m_0 c^2 + J^{\mu} A_{\mu} \tag{1.10}$$

The application of Euler-Lagrange equations then gives the equations of motion for the particle interacting with fields as

$$\boxed{\frac{\mathbf{d}p_{\mu}}{\mathbf{d}\tau} = q F_{\mu\nu} u^{\nu}} \tag{1.11}$$

where q is the charge of the particle. We recognize the right-hand side as the Lorentz force. Equations (1.8), (1.9) and (1.11) now form a closed system of equations. We have to warn the kind reader that there are some inconsistencies within the classical regime, which will be discussed in 1.1.3.

1.1.1 Electron Motion in Laser Field

If we consider the Lorenz gauge condition $\partial_\mu A^\mu = 0$, we immediatelly obtain the non-homogeneous wave equation from the equation (1.8) via the definition of the electromagnetic tensor (1.6)

$$\Box A^\nu = -\mu J^\nu \tag{1.12}$$

where $\partial/\partial x^\mu = \partial_\mu = (\partial_t/c, \nabla)$ is the covariant four-gradient, $\Box = \partial_\mu \partial^\mu = \partial^\mu \partial_\mu = \eta_{\mu\nu}\partial^\nu\partial^\mu = \left(-\frac{1}{c^2}\frac{\partial^2}{\partial t^2} + \triangle\right)$ is the d'Alembert operator and $\eta^{\mu\nu} = \eta_{\mu\nu} = diag(-1, 1, 1, 1)$ is the Minkowski metric. We will consider now the case of an electromagnetic plane wave, which is the solution of the source-less homogeneous wave equation $\Box A^\nu = 0$. Since there are no sources, static fields can also be neglected (we assume electron's field to be too weak compared to the laser) and thus we obtain plane wave solutions in the form of $A^\nu = (0, \boldsymbol{A}(k_\mu x^\mu)) = (0, \boldsymbol{A}(\boldsymbol{kx} - \omega t))$. We will consider a system where such generally polarized plane wave $\boldsymbol{A} = (A_x, A_y, 0)$ propagating in the z direction interacts with an electron.

We will now enjoy the fruits of our Lagrangian approach to electrodynamics, since we will be able to trivially reveal all the symmetries of the system very easily. With the plane wave $\boldsymbol{A}(z - ct)$, the Lagrangian (1.10) doesn't depend on the x and y coordinates, since the first term in (1.10) only depends on four-velocity (see Appendix A.3). Let us now apply the Euler-Lagrange equations to reveal all the symmetries and equations of motion of our system. First, since the Lagrangian doesn't depend on x and y, we obtain conservation of x and y generalized momenta ($\mu = 1, 2$) from E-L equations.

$$\frac{\mathbf{d}}{\mathbf{d}\tau}\left(\frac{\partial \mathcal{L}}{\partial u^\mu}\right) = \frac{\mathbf{d}}{\mathbf{d}\tau}\left(p_\mu + qA_\mu\right) = 0 \tag{1.13}$$

In other words, if we consider the electron to be initally at rest, we obtain after integration

$$p_x = eA_x$$

$$p_y = eA_y$$

The E-L equation in the z-direction ($\mu = 3$) is

$$\frac{\mathbf{d}p_z}{\mathbf{d}t} = -e\boldsymbol{v} \cdot \frac{\partial \boldsymbol{A}}{\partial z} \tag{1.14}$$

And finally for the time component ($\mu = 0$) we have for the energy of the particle from the E-L equation

$$\frac{\mathbf{d}}{\mathbf{d}t}(\gamma m_e c^2) = -e\boldsymbol{v} \cdot \boldsymbol{E} = e\boldsymbol{v} \cdot \frac{\partial \boldsymbol{A}}{\partial t} = -ec\boldsymbol{v} \cdot \frac{\partial \boldsymbol{A}}{\partial z} \tag{1.15}$$

Where we've transformed from proper to observer time and used the chain rule $\frac{\partial}{\partial t} = -c\frac{\partial}{\partial z}$ valid for plane wave travelling in vacuum in the positive direction. By combining (1.14) and (1.15), we obtain another conserved quantity

$$\frac{\mathbf{d}}{\mathbf{d}t}(\gamma m_e c^2 - cp_z) = 0 \tag{1.16}$$

If we integrate (1.16) from t_i to t with the initial condition that the electron was initially at rest, we get

$$\gamma m_e c^2 - cp_z = m_e c^2 \tag{1.17}$$

A usual and practical convention in relativistic physics is to work within normalized units, since they often clearly define relativistic regimes. Therefore, we define the normalized vector potential $\boldsymbol{a} = e\boldsymbol{A}/m_e c$, velocity $\boldsymbol{\beta} = \boldsymbol{v}/c$ and momentum $\overline{\boldsymbol{p}} = \boldsymbol{p}/m_e c = \gamma\boldsymbol{\beta}$. Reaching values of ~ 1 in all of these normalized quantities indicates a shift towards relativistic dynamics. With previous definitions, we have

$$\overline{p}_x = a_x \tag{1.18}$$

$$\overline{p}_y = a_y \tag{1.19}$$

$$\overline{p}_z = \gamma - 1 \tag{1.20}$$

By evaluating the energy-momentum relation $E^2 = (pc)^2 + (m_e c^2)^2$ with the previous three results we get $\overline{p}_z = \boldsymbol{a}^2/2$ which gives us dependence of the particle energy on the intensity of the laser field as

$$\gamma = 1 + \frac{a^2}{2} \tag{1.21}$$

where we have used $a^2 = a_x^2 + a_y^2$. Equations (1.21) and (1.20) tell us that the particle gains energy in the laser propagation direction. This acceleration scheme is sometimes called $\boldsymbol{j} \times \boldsymbol{B}$ heating. This result couldn't be obtained in the non-relativistic limit, since the magnetic part of the Lorentz force $\boldsymbol{v} \times \boldsymbol{B}$ is the driving force and in the non-relativistic limit we have $|\boldsymbol{v} \times \boldsymbol{B}|/|\boldsymbol{E}| \doteq v/c \ll 1$. We will now focus on the simplest case of a linearly polarized plane wave in the form $\boldsymbol{a} = a_0 \cos(kz - \omega t)\boldsymbol{e}_x = a_0 \cos(\eta)\boldsymbol{e}_x$ where $\eta/k = z - ct$ is the coordinate in the co-moving frame of the laser.

$$\overline{p}_x = \frac{\gamma}{c}\frac{\partial x}{\partial t} = a_0 \cos(\eta) \tag{1.22}$$

$$\overline{p}_y = \frac{\gamma}{c}\frac{\partial y}{\partial t} = 0 \tag{1.23}$$

$$\overline{p}_z = \frac{\gamma}{c}\frac{\partial z}{\partial t} = \frac{\boldsymbol{a}^2}{2} = \frac{a_0^2}{2}\cos^2(\eta) \tag{1.24}$$

Integration with respect to time of the co-moving frame τ with the usage of $\partial t/\partial\tau = \gamma$ yields the solution

$$x = \frac{a_0}{k}\sin(\eta) \tag{1.25}$$

$$z = \frac{a_0^2}{4k}\left(\eta + \frac{1}{2}\sin(2\eta)\right) \tag{1.26}$$

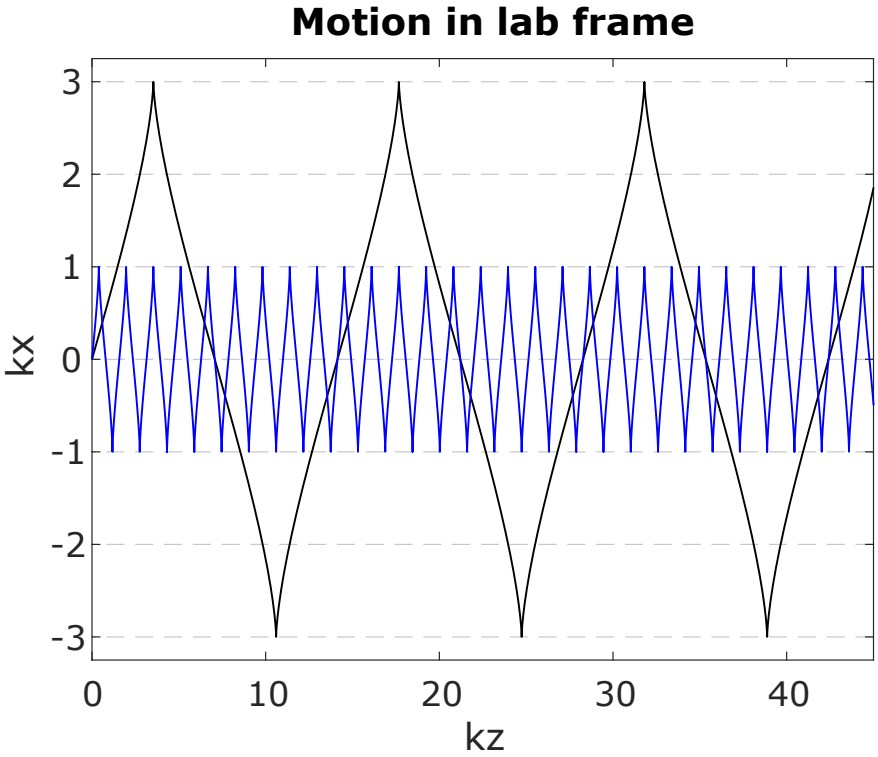

Figure 1.1: Trajectory of electron observed within the laboratory reference frame. Corresponding laser strength was $a_0 = 1$ (blue) and $a_0 = 3$ (black).

In Fig. 1.1, we have plotted the solutions (1.25) and (1.26) for $a_0 = 1$ and $a_0 = 3$. As observed from the laboratory frame, the electron conducts a sharply oscillating saw-like motion with twice the laser frequency in the longitudal direction, the amplitude of the longitudal oscillations also increases as $\sim a_0^2/2$ compared to the transverse amplitude $\sim a_0$. If we take the time average of the equations (1.22), (1.23), (1.24) we observe that there is an average drift velocity of the electron $\langle v_z\rangle = ca_0^2/(4+a_0^2)$. The motion of the electron within the reference frame moving with the drift velocity can be acquired in the same fashion as (1.25), (1.26), except we substract the cycle-averaged longitudal momentum from (1.24), that is $\overline{p}_z^{'} = \overline{p}_z - \langle\overline{p}_z\rangle = a^2/2 - a_0^2/4$. The notorious figure of eight motion reveals itself in the drift frame and is plotted for different values of a_0 in the Fig. 1.2. As a quick note, solving (1.18), (1.19), (1.20) for circular polarization gives helical trajectory in the lab frame and no oscillations in the z direction in the drift frame.

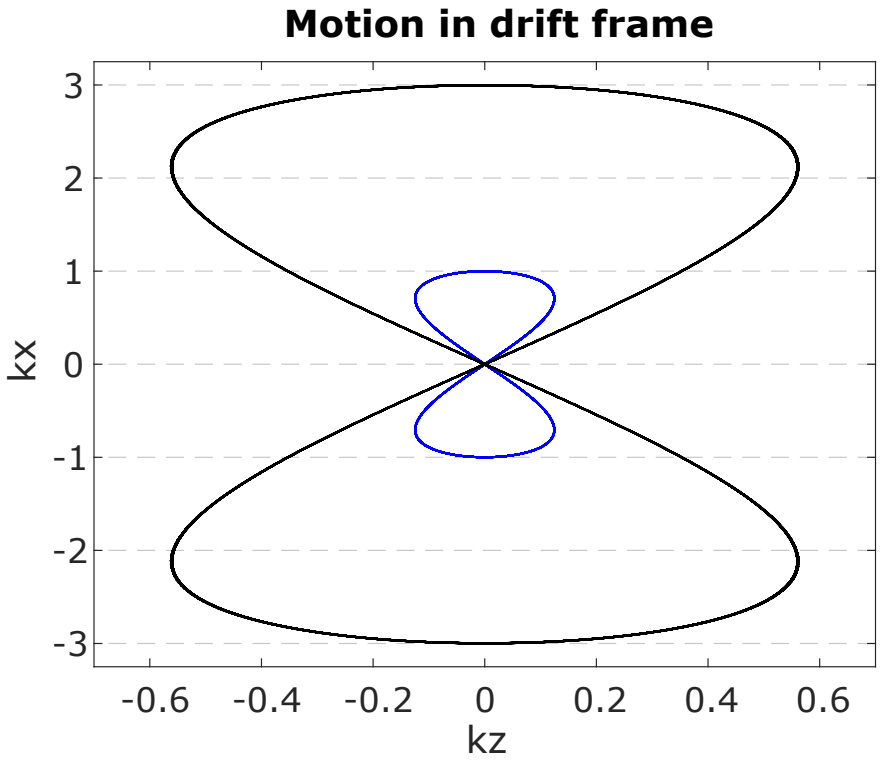

Figure 1.2: Trajectory of the electron observed within the co-moving electron drift frame. Corresponding laser strength was $a_0 = 1$ (blue) and $a_0 = 3$ (black).

To consider energy the electron can obtain with availible lasers, let us first return to SI units to connect the normalized vector potential to intensity.

$$a_0 = \frac{eA_0}{m_e c} = \frac{eE_L}{m_e c\omega} = \sqrt{\frac{e^2\lambda_L^2 I_0}{2\pi\epsilon_0 m_e^2 c^5}} \doteq 0.855\sqrt{I[10^{18}W/cm^2]\lambda_L^2[\mu m]} \tag{1.27}$$

Many laser systems are now able to operate at focused peak intensities above 10^{20} W/cm^2, which for a laser with wavelength 800 nm corresponds to $a_0 \doteq 6.9$. Cycle-averaged momentum within the lab frame is $\langle p \rangle = \frac{m_e c a^2}{4}$, which corresponds to momentum gain of 6 MeV/c. While this is still worse than conevntional accelerators, it is 5 orders of magnitude worse compared to the momentum achievable by LWFA as put forward in the introduction. Previous results also inherently assume the laser beam is infinite. In reality, as can be also seen in the co-moving drift frame, the electron is only pushed by the presence of the laser to a new longitudal position, but doesn't gain any net energy over one laser cycle. Once the laser stops, the acceleration stops as well and no net energy gain is achieved, which is the case with a real laser pulse. These results summarize the Lawson-Woodward theorem, which states that the net energy of an electron interacting with electromagnetic radiation in vacuum is zero [28]. However, in the next section we will maybe surprisingly see that the spatial distribution of the intensity is a crucial and necessary part of plasma accelerators.

1.1.2 Ponderomotive Force

We've briefly mentioned at the end of the previous subsection that the spatial distribution of intensity plays a dominant effect during the interaction of the laser field and the electron. This effect manifests itself through the *Ponderomotive Force*, which pushes all charged particles from the regions of high intensity. Before we once again utilize the Lagrangian approach to derive a fully relativistic treatment, we will quickly offer an intuitive feel for it's non-relativistic emergance.

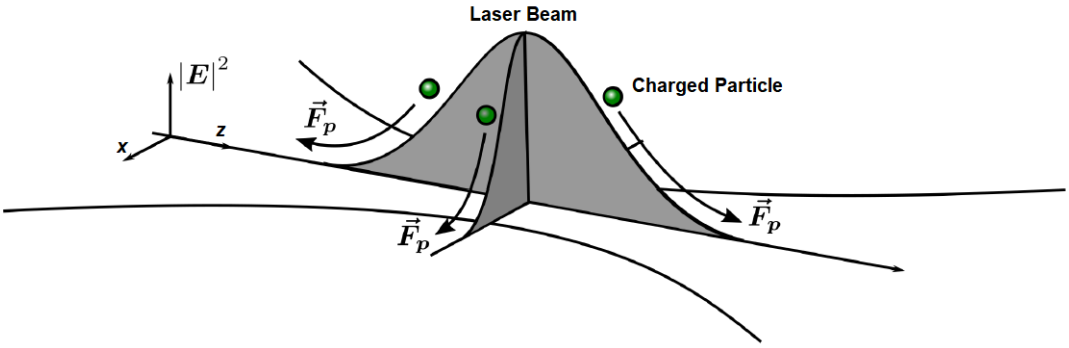

Figure 1.3: Ponderomotive force pushing all charged particles from the region of the laser beam.

Non-relativistic case

Let us consider the motion of a charged particle in the laser field as presented in the previous subsection. If we consider the non-relativistic case where $a_0 \ll 1$, we have $p_z = a^2/2 \approx 0$. The quivering motion of the particle is then described by equations (1.18), (1.19), which gives the velocity as

$$\boldsymbol{v} = \frac{c}{\gamma}\boldsymbol{a} \approx c\boldsymbol{a} \tag{1.28}$$

We then define the ponderomotive or cycle-averaged quiver energy of the particle as the cycle-averaged kinetic energy of such motion

$$U_p = \frac{1}{2}mc^2\langle \boldsymbol{a}^2 \rangle \tag{1.29}$$

If we now consider the laser field described by $\boldsymbol{a}$ to have a slowly varying envelope and consider this ponderomotive energy to be the potential energy of the particle, we obtain the ponderomotive force in the non-relativistic case

$$\boxed{\boldsymbol{F}_p = -\frac{1}{2}m_e c^2 \nabla \langle \boldsymbol{a}^2 \rangle = -\frac{q^2}{4m\omega^2}\nabla |E|^2} \tag{1.30}$$

where q and m are the particle's charge and mass and ω is the angular frequency of the laser. This heuristic derivation shows us that the existence of a spatial distribution of the electromagnetic field gives rise to the ponderomotive force.

Relativistic case

In the relativistic regime where $a_0 \gg 1$, the longitudal momentum p_z becomes dominant and previous result is invalid. The following result is a highly simplified approach to the rigorous treatment presented in [29]. We will once again shift into the drift frame with center corresponding to the electron oscillation center. Once again with the substitution $\eta/k = z - ct$ valid for a monochromatic plane wave. We can assume the existence of $\eta(x^\nu)$ for a general electromagnetic field when an oscillation center exists. We will obtain the Lagrangian transformed into the drifting wave frame from Lorentz invariance of the action

$$\delta S = \delta \int_{\tau_i}^{\tau_f} \mathcal{L}(q^\mu, \dot{q}^\mu, \tau)\mathbf{d}\tau = \delta \int_{\tau_i}^{\tau_f} \mathcal{L}(q^\mu, \dot{q}^\mu, \tau)\frac{\mathbf{d}\tau}{\mathbf{d}\eta}\mathbf{d}\eta = \delta \int_{\tau_i}^{\tau_f} L(\eta)\mathbf{d}\eta = 0 \quad (1.31)$$

The cycle-averaged Lagrangian in the drift frame is then

$$\langle L(\eta)\rangle = \frac{1}{2\pi}\int_{\eta}^{\eta+2\pi} L(\zeta)\mathbf{d}\zeta \quad (1.32)$$

The non-trivial and lengthy proof in [29] then presents that the motion of the particle's oscillation center is given by the cycle-averaged E-L equations

$$\frac{\partial\langle\mathcal{L}\rangle}{\partial\langle q^\mu\rangle} - \frac{\mathbf{d}}{\mathbf{d}\tau}\left(\frac{\partial\langle\mathcal{L}\rangle}{\partial\langle\dot{q}^\mu\rangle}\right) = 0 \quad (1.33)$$

where $\langle q^\mu\rangle$ and $\langle\dot{q}^\mu\rangle$ are configuration coordinate and velocity of the particle's oscillation center and generally $\langle\mathcal{L}\rangle = \langle L(\eta)\rangle(\mathbf{d}\eta/\mathbf{d}\tau)$. In the case of a charged particle interacting with a laser field, the Lagrangian describing the dynamics of the particle's oscillation center (treated as described in A.3) is

$$\langle\mathcal{L}\rangle = -m_{eff}c^2 \quad (1.34)$$

where $m_{eff} = m\langle\gamma\rangle$ and $\langle\gamma\rangle$ corresponds to the oscillating particle's cycle-averaged gamma as observed within the drift frame. We can obtain $\langle\gamma\rangle$ immediatelly from (1.18), (1.19), (1.20) and the energy-momentum relation, since

$$\langle\gamma^2\rangle = \langle 1 + \overline{\boldsymbol{p}}^2\rangle = 1 + \langle\boldsymbol{a}^2\rangle \Rightarrow \langle\gamma\rangle = \sqrt{1 + \langle\boldsymbol{a}^2\rangle} \quad (1.35)$$

where we've used the fact that cycle-averaged longitudal momentum (1.20) vanishes within the drift frame, $\langle\overline{p}'_z\rangle = \langle\overline{p}_z - \langle\overline{p}_z\rangle\rangle = 0$. The fully relativistic case of the ponderomotive force then easily follows from the E-L equations (1.33) for the spatial components $\mu = 1, 2, 3$ as

$$\boxed{\boldsymbol{F}_p^{rel.} = -mc^2\nabla\sqrt{1 + \langle\boldsymbol{a}^2\rangle}} \quad (1.36)$$

We also note that for linear polarization $\langle\boldsymbol{a}^2\rangle = \boldsymbol{a}^2/2$ and for circular polarization $\langle\boldsymbol{a}^2\rangle = \boldsymbol{a}^2$.

In the formula (1.36), we can see with the definiton of $\boldsymbol{a} = q\boldsymbol{A}/mc$ that $\boldsymbol{F}_p^{rel.} \sim \frac{1}{\sqrt{m^2+1}} \sim \frac{1}{m}$, which means that the exerted force on protons will be at least three orders of magnitude weaker than on electrons. This is an important observation, because within the ultrafast interaction of LWFA, protons or even heavier ions won't be able to move during the few femtosecond long interactions with a laser pulse compared to the electrons. This means that the positive ions effectively don't affect the dynamics of the interaction and we are able to separate and simplify the dynamics of electrons and ions in the following sections by taking the ions as an immobile, charged background.

We can see that for a laser pulse with the wavelength 800 nm and peak intensity $I \approx 10^{20}$ W/cm^2 corresponding to $a_0 \doteq 6.9$, the ponderomotive potential is $U_p^{rel.} = m_{eff}c^2 = 2.5$ MeV, which in combination with the short time scale of interaction renders the ponderomotive force useless for direct acceleration purposes. However, as we've previously mentioned the ponderomotive force is still critical for the acceleration scheme of LWFA, because it excites plasma waves due to the fast expulsion of electrons from the high intensity regions.

1.1.3 Radiation Reaction

Before we move onto collective laser-plasma phenomena, we need to inform the kind reader that there are some inconsistencies within the classical regime of relativistic electrodynamics that we've described. These inconsistencies mainly stem from the fact that, as we will see in **Chapter 2**, Maxwell equations (1.8), (1.9) describe that an accelerating charged particle radiates electromagnetic waves. As radiation carries momentum, there must be some back-reaction causing the radiating particle to lose energy due to conservation laws. This is often called *radiation reaction*.

Non-relativistic case

In **Chapter 2**, we will derive the classical result of Larmor [30] which gives the radiated power by a non-relativistic charged particle as

$$\boxed{\mathcal{P} = \frac{q^2}{6\pi\epsilon_0 c^3}\mathbf{a}^2} \tag{1.37}$$

from the radiated power we can obtain the radiation back-reaction force acting on the radiating particle by considering the energy it loses due to radiation emission over some time interval (t_i, t_f) as

$$\begin{aligned}\mathcal{E} &= \int_{t_i}^{t_f} (\mathbf{F}_{rad}\cdot\mathbf{v})\,\mathbf{d}t = \int_{t_i}^{t_f} -\mathcal{P}\mathbf{d}t = \int_{t_i}^{t_f}\left(-\frac{q^2}{6\pi\epsilon_0 c^3}\dot{\mathbf{v}}\cdot\dot{\mathbf{v}}\right)\mathbf{d}t \\ &= \left[-\frac{q^2}{6\pi\epsilon_0 c^3}\dot{\mathbf{v}}\cdot\mathbf{v}\right]_{t_i}^{t_f} - \int_{t_i}^{t_f}\left(-\frac{q^2}{6\pi\epsilon_0 c^3}\ddot{\mathbf{v}}\cdot\mathbf{v}\right)\mathbf{d}t = \int_{t_i}^{t_f}\left(\frac{q^2}{6\pi\epsilon_0 c^3}\ddot{\mathbf{v}}\cdot\mathbf{v}\right)\mathbf{d}t\end{aligned} \tag{1.38}$$

Where we assumed that the velocity or acceleration is zero at the beginning or end of the motion over some time interval. By comparing the first and the last integrand in the previous derivation, the radiation reaction force can be then assigned in the non-relativistic case as

$$\mathbf{F}_{rad} = \frac{q^2}{6\pi\epsilon_0 c^3}\dot{\mathbf{a}} \tag{1.39}$$

A particle moving in a cyclotron orbit will experience jerk $\dot{\mathbf{a}}$ in the opposite direction of velocity, so we see that this force indeed provides a braking action for the radiating particle. However, a quick comparison with the radiated power (1.37) immediatelly tells us that this must be dynamically wrong, since radiation is emitted during constant acceleration, but particle's dynamics are unchanged due to (1.39) being zero. Another unsatisfactory behaviour of this solution is the fact that Newton's equations of motion become third order differential equations in time and therefore also need to provide the initial acceleration of the particle. This increase in the order of the differential equations unfortunately introduces an even worse offender in the form of pathological *runaway solutions*, which emerge due to the third derivative in time.

We can easily see this pathology when we solve Newton's equations of motion with constant external force $\boldsymbol{F}_{ext}$ acting on an initally inertial particle $\boldsymbol{a}(0) = 0$

$$m_e \mathbf{a} = \frac{q^2}{6\pi\epsilon_0 c^3}\dot{\mathbf{a}} + \boldsymbol{F}_{ext} \Rightarrow \mathbf{a}(t) = \boldsymbol{F}_{ext}\left(1 - e^{t/\tau_{rad}}\right) \tag{1.40}$$

where $\tau_{rad} = e^2/6m_e\pi\epsilon_0 c^3$ tells us that the electron being acted upon even by weak external forces could accelerate to relativistic energies in few $\tau_{rad} = 6.26 \cdot 10^{-24}$ s. This obviously doesn't satisfy conservation of energy and we are forced to look for a more complete description of the radiation reaction force in the relativistic regime.

Relativistic case

The total radiated power (1.37) is Lorentz invariant as shown in [28] and therefore we can do a straightforward generalization to the relativistic regime by simply switching towards Lorentz invariant product of four-acceleration through $\mathbf{a} \to a^\mu$, which will be properly validated in Chapter 2, then the radiated power becomes

$$\boxed{\mathcal{P}_{rel.} = -\frac{q^2}{6\pi\epsilon_0 c^3} a_\mu a^\mu} \tag{1.41}$$

where $a^\mu = \mathbf{d}u^\mu/\mathbf{d}\tau$ is four-acceleration. If we use the definition of four-velocity in (1.5), the radiated power from a relativistic charged particle is given as

$$\begin{aligned} \mathcal{P}_{rel.} &= -\frac{q^2}{6\pi\epsilon_0 c^3}\left(\frac{\mathbf{d}u^\mu}{\mathbf{d}\tau}\cdot\frac{\mathbf{d}u^\mu}{\mathbf{d}\tau}\right) = \frac{q^2}{6\pi\epsilon_0 c^3}\gamma^6\mathbf{a}^2(1-\beta^2\sin^2\theta) \\ &= \frac{q^2}{6\pi\epsilon_0 c^3}\gamma^6\left(\mathbf{a}^2 - \left|\frac{\mathbf{v}\times\mathbf{a}}{c}\right|^2\right) = \frac{q^2}{6\pi\epsilon_0 c}\gamma^6\left(\dot{\boldsymbol{\beta}}^2 - \left|\boldsymbol{\beta}\times\dot{\boldsymbol{\beta}}\right|^2\right) \end{aligned} \tag{1.42}$$

The last equation tells us that radiated power scales with γ^6, which means that radiative energy losses can be potentially neglected for non-relativistic or non-accelerating particles, but they get increasingly relevant once accelerating particles enter relativistic regime. Classical electrodynamics therefore predict significant radiative losses for accelerating relativistic particles, however these losses are not accounted for in the description of particle dynamics by Lorentz force (1.11), since we inherently assumed that the electromagnetic tensor $F^{\mu\nu}$ describes only fields generated externally, as a laser for example. If we wanted to modify the Lorentz' force to account for the particle's own generated field, we would have to include them into the electromagnetic tensor $F^{\mu\nu} = F^{\mu\nu}_{ext} + F^{\mu\nu}_{rad}$, producing a modified Lorentz force law

$$\frac{\mathbf{d}p^\mu}{\mathbf{d}\tau} = \frac{q}{mc}(F^{\mu\nu}_{ext} + F^{\mu\nu}_{rad})p_\nu = \frac{q}{mc}F^{\mu\nu}_{ext}p_\nu + \mathcal{F}^\mu_{rr} \tag{1.43}$$

Where $\mathcal{F}^\mu_{rr}$ is the radiation reaction force acting on the charged particle. Unfortunately, with this modification we face our first obstacle. For a point-like

charged particle, which we assume is the case for elementary particles like electron, $F^{\mu\nu}_{self}$ is divergent, as shown in [28]. It is possible to derive the radiation reaction force by considering a charged object of finite volume and then taking a point-like limit, however in Appendix A.4 we offer a derivation that simply rests on conservation laws and symmetry. The result is

$$\mathcal{F}^{\mu}_{rr} = \frac{q^2}{6\pi\epsilon_0 c^3}\left(\frac{\mathbf{d}a^{\mu}}{\mathbf{d}\tau} + \frac{u^{\mu}}{c^2}(a^{\nu}a_{\nu})\right) \tag{1.44}$$

Combining (1.43) with (1.44) gives the fully relativistic Lorentz-Abraham-Dirac (LAD) equation [31]

$$\frac{\mathbf{d}p_{\mu}}{\mathbf{d}\tau} = qF_{\mu\nu}u^{\nu} + \frac{q^2}{6\pi\epsilon_0 c^3}\left(\frac{\mathbf{d}a^{\mu}}{\mathbf{d}\tau} + \frac{u^{\mu}}{c^2}(a^{\nu}a_{\nu})\right) \tag{1.45}$$

Note that (1.44) now forces the charged particle to experience drag even in constant acceleration, which was impossible with the non-relativistic version (1.39). The LAD equation enables radiative drag in arbitrary accelerating cases, however it is still addled with the runaway solutions that violate conservation of energy. This pathology can be removed by demanding that acceleration tends to zero after long enough time duration. This in turn introduces another pathology in the form of *pre-acelerated solutions*, where acceleration at some time depends on acceleration in the future. These pathologies are the result of the first term in (1.44), called Shott term, which depends on jerk, as it was the case in the non-relativistic regime. These problems of LAD equation are still to this day being adressed, some succesfully through corrections, as reviewed in [32].

One such approach to the treatment of radiation reaction was proposed by Landau and Lifshitz in [33]. This approach lies in the reduction of order of the differential equations, which we will now follow. The fact that τ_{rad} is of such small order allows us to iteratively obtain a solution correct to the first order in τ_{rad}. If we substitute $\mathbf{d}p^{\mu}/\mathbf{d}\tau \to (q/mc)F^{\mu\nu}p_{\nu}$ to (1.44), we obtain the Landau-Lifshitz force, which approximates the LAD equation to first order in τ_{rad} and eliminates dependence on jerk, which consequentely eliminates the pathologies. If we add this Landau-Lifshitz force to (1.43), an exact solution can be obtained for the motion of an electron in a plane wave [34], similarly to how we proceeded in 1.1.1. This solution works as a very useful reference for the effect of the radiation reaction. In Fig. 1.4, we can see that at very high intensities, the exclusion of the radiation reaction would lead to neglection of the radiative drag the particle experiences during acceleration.

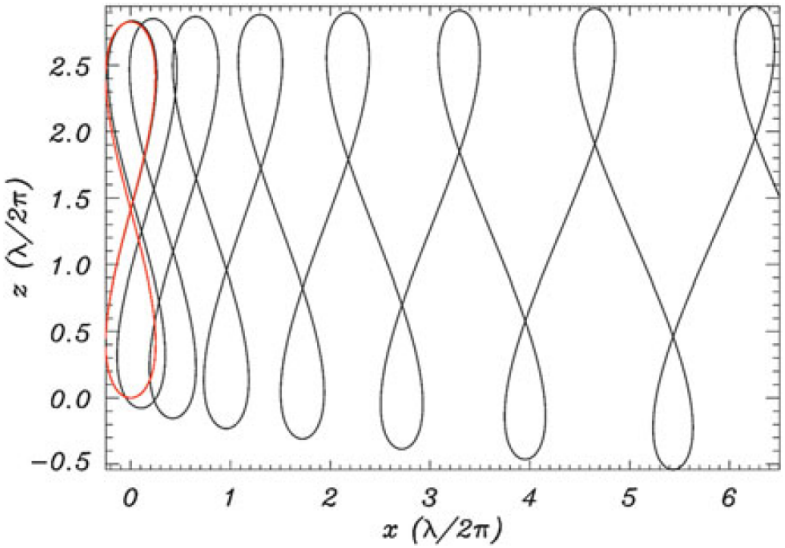

Figure 1.4: The black trajectory describes the disturbed figure-of-eight motion in the drift frame due to the Landau-Lifshitz force. The red trajectory corresponds to the case when radiation reaction is neglected. Laser strength was set at $a_0 = 100$. Reprinted from [35]

If we inspect closely the radiation reaction force in (1.44), we can see that the radiation reaction is strongest during transverse acceleration, since

$$\mathcal{F}^{\mu}_{rr} \sim a^{\nu} a_{\nu} = -\gamma^6 \mathbf{a}^2 (1 - \beta^2 \sin^2\theta) = \begin{cases} -\gamma^6 \mathbf{a}^2, & \text{if } \mathbf{v} \parallel \mathbf{a} \\ -\gamma^4 \mathbf{a}^2, & \text{if } \mathbf{v} \perp \mathbf{a} \end{cases} \tag{1.46}$$

We can expect to observe strong signatures of radiation reaction during experiments with counter propagating electron and laser beams, which could be realized in an all-optical setup thanks to LWFA. If we also consider electric field strong enough to do work equal to the rest energy of the electron $m_e c^2$ over the Compton wavelength $\lambda_c = h/2\pi m_e c$, we get

$$E_s = \frac{m_e c^2}{\lambda_c} = \frac{m_e^2 c^3}{eh/2\pi} = 1.3 \times 10^{16} \text{ V.cm}^{-1} \tag{1.47}$$

which is the *Schwinger field*. This corresponds to the intensity $I_s = 2.3 \times 10^{29}$ W.cm^{-2}, still around 7 orders of magnitude away from intensities currently achievable in laboratory conditions. If the electric field approaches E_s in the rest frame of an electron, non-linear effects of the quantum electrodynamics (QED) in vacuum like pair-production will begin manifesting [36]. However, this QED regime can be explored experimentally with much lower intensities. In the rest frame of an relativistic electron travelling with velocity $\boldsymbol{\beta}$, electric field of a laser is Lorentz transformed to $E' = \gamma(1+\beta)E \sim 2\gamma E$. The frequency of the field also becomes Doppler upshifted, $\omega' = \gamma(1+\beta)\omega$. If the photon energy becomes of the same order as electron rest energy $h\nu' = m_e c^2$, or the electric field in the rest frame approaches Schwinger field, QED effects need to be considered.

We will conclude this section with the following observations. As shown in [36], the LAD equation and the Landau-Lifshitz reduction are equivalent in the first order of fine-structure constant $\alpha \doteq 1/137$ to a perturbative QED result. We can see that the radiative time we introduced is comparable to the time it takes light to traverse the classical electron radius r_e

$$\tau_{rad} = \frac{2}{3}\frac{r_e}{c} = \alpha\frac{2}{3}\frac{\lambda_c}{c} = \alpha\tau_{QED} \tag{1.48}$$

This means that the pathological radiative time scales of the LAD equation are smaller than the time scales of QED interactions, by a factor of α. This tells us that the onset of radiation reaction effects during these time scales where pathologies manifest must be necessarilly tied in with the QED effects. It would seem reasonable to explore the radiation reaction within the QED framework, where the quantization of fields and particles naturally enforces momentum and energy conservation during interactions. The QED regime also introduces effects like *straggling*, where the stochastic nature of radiation emission allows higher energetic electrons to propagate significantly longer distances without radiating, which in turn enhances emission of higher energy photons and further deviates the radiation emission spectrum and particle dynamics from the classical regime [37]. Upcoming high energy experiments involving collisions of laser and electron beams will therefore require complete description within the QED regime to sufficiently describe energy spectra of measured photons and electrons.

1.2 Plasma Interacting with Electromagnetic Field

The dynamics of many particles interacting with electromagnetic field will reveal collective behaviour that is inexplicable within the single particle framework we have developed in the previous section. This collective behaviour will reveal accelerating schemes dramatically superior to the possibilities of direct acceleration by the laser field.

1.2.1 Plasma Generation

Plasma is the fourth state of matter and probably the most abundant one in the universe, if we neglect the existence of dark matter [38]. The plasma can be generated in laboratory, for example if we focus an intense laser beam upon a gas target. In 1965 L. V. Keldysh pioneered theory describing the interaction of a bound electron with electromagnetic wave [39]. This theory identifies possible regimes of laser induced ionization for given laser field intensity through the Keldysh parameter

$$\Gamma = \sqrt{\frac{I_p}{2U_p}} \tag{1.49}$$

where I_p is the ionization potential, the energy necessary to ionize the bound electron and $U_p \sim I_{laser}$ is the ponderomotive energy (1.29). The value of Γ compares the strength of the laser field quivering with the electron to the energy that must be given to the bound electron so it becomes free from it's parent atom. $\Gamma \ll 1$ identifies the perturbative regime where laser field effectively doesn't affect the atomic Coulomb potential that bounds the electron. This perturbative regime however still allows ionization through non-linear absorption of multiple photons, this is called *multiphoton ionization*. Reaching $\Gamma \sim 1$, which for lighter gases corresponds to laser intensity of $I \approx 10^{14-15}$ W.cm^{-2} brings us to the regime of *tunnel ionization*. The perturbation of the Coulombic potential is now strong enough to allow the electron to tunnel through the induced potential barrier. $\Gamma \gg 1$ identifies the regime of *barrier-suppressed ionization*, where the electric field is strong enough to completely suppress the Coulombic potential and directly release the bound electron. As an example, 808 nm laser pulse with focused intensity $\sim 10^{16}$ W.cm^{-2} completely ionizes both hydrogen and helium [40].

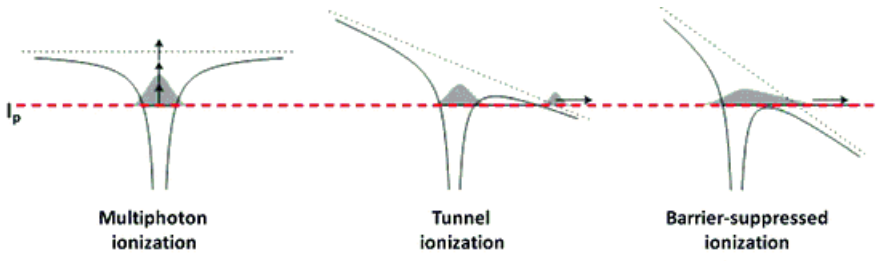

Figure 1.5: Changing ioniziation regimes with respect to increasing electric field intensity. Reprinted from [40]

1.2.2 Electromagnetic Waves in Plasma

The plasma consisting of electrons and ions generated through mechanisms of gas ionization we've presented is a very different medium compared to empty vacuum. By combining Maxwell equations (1.8), (1.9) re-arranging for $\boldsymbol{E}$ and applying the curl operator, we obtain

$$\nabla \times \nabla \times \boldsymbol{E} = -\frac{1}{c^2}\frac{\partial^2 \boldsymbol{E}}{\partial^2 t} - \mu \frac{\partial \boldsymbol{j}}{\partial t} \tag{1.50}$$

By applying the Fourier-Laplace transform on the field $\boldsymbol{E}(\boldsymbol{r}, t)$, we obtain for each Fourier-Laplace mode $\boldsymbol{E}(\boldsymbol{k}, \omega) = \boldsymbol{E}_{\boldsymbol{k},\omega}$ the following condition

$$\boldsymbol{k} \times \boldsymbol{k} \times \boldsymbol{E}_{\boldsymbol{k},\omega} = \frac{1}{c^2}\left(\frac{n_e e^2}{m_e \epsilon_0} - \omega^2\right)\boldsymbol{E}_{\boldsymbol{k},\omega} \tag{1.51}$$

Where we've made the assumption that electrons are freely moving in the presence of the electromagnetic field and the source term then became $\boldsymbol{j} = -e n_e \langle \boldsymbol{v} \rangle = -e^2 n_e \dot{\boldsymbol{E}}/m_e \omega^2$. These equations describe allowed electromagnetic field modes in plasma. We can easily obtain dispersion relations for two boundary cases. If we consider only modes satisfying $\boldsymbol{k} \parallel \boldsymbol{E}$, the left hand side is identically zero and the right hand side produces the only possible oscillation frequency as

$$\omega_p = \sqrt{\frac{n_e e^2}{m_e \epsilon_0}} \tag{1.52}$$

which is called *plasma frequency*. Since generally electromagnetic modes satisfy $\boldsymbol{k} \times \boldsymbol{E} = \omega \boldsymbol{B}$, we see that this mode is a longitudal electrostatic wave. We can immediatelly see that it must be these waves that will produce plasma acceleration, since they carry electric intensity in the direction of the wave propagation. The second boundary case corresponds to electromagnetic waves in vacuum, that is $\boldsymbol{k} \perp \boldsymbol{E}$. For this condition, (1.51) produces dispersion relations for transverse electromagnetic waves in plasma as

$$\boxed{\omega^2 = \omega_p^2 + c^2 k^2} \tag{1.53}$$

these dispersion relations allow us to compute the phase and group velocities of electromagnetic waves inside plasma. If $\omega > \omega_p$, k is real and the wave can propagate through the medium. For $\omega < \omega_p$, k is imaginary and the electromagnetic wave must be reflected upon reaching the plasma interface and exponentially attentuated inside the plasma due to conservation of energy. For a given electromagnetic wave frequency, only the plasma density n_e can affect this behaviour. This defines the critical density separating the real and evanescent wave cases as

$$n_c = \frac{\omega^2 m_e \epsilon_0}{e^2} \tag{1.54}$$

If $n_e < n_c$, electromagnetic wave propagation is allowed and we say that the plasma is *underdense*. On the other hand, if $n_e > n_c$, electromagnetic wave proapgation is unfavoured and the plasma is called *overdense*.

1.2.3 Relativistic Nonlinear Optics

Let us focus now on the effect the plasma medium has on propagating lasers. From dispersion relations for electromagnetic waves in plasma (1.53) we obtain the phase and group velocity as

$$v_p = \frac{\omega}{k} = c \Big/ \sqrt{1 - \left(\frac{\omega_p}{\omega}\right)^2} \tag{1.55}$$

$$v_g = \frac{\mathbf{d}\omega}{\mathbf{d}k} = c \cdot \sqrt{1 - \left(\frac{\omega_p}{\omega}\right)^2} \tag{1.56}$$

we can therefore easily see that the refractive index of plasma is

$$\boxed{n = \frac{c}{v_p} = \sqrt{1 - \left(\frac{\omega_p}{\omega}\right)^2} = \sqrt{1 - \left(\frac{n_e}{n_c}\right)}} \tag{1.57}$$

for this formula to work there's a hidden assumption we would like to remind the kind reader of, which is that the response of electrons is much quicker than the heavier ions. For laser frequency we have $\omega \gg \omega_{ions}$ at low temperatures. The contribution of ions is reached at frequencies well below ω_p, therefore interaction with electromagnetic waves is inaccessible. We can therefore safely neglect the contribution of ions and neutrals to the refractive index in this case at low temperatures [38]. Furthermore, we note that $n < 1$ always during low temperature laser-plasma interactions. Relativistic nonlinear optical effects come into picture when we include the increase of electron relativistic mass $m_e \to \gamma m_e$ into the plasma frequency

$$\omega_p^2 = \frac{n_e e^2}{\gamma m_e \epsilon_0} \tag{1.58}$$

which naturally modifies the index of refraction due to relativistic electrons

$$n = \frac{c}{v_p} = \sqrt{1 - \left(\frac{\omega_p}{\gamma\omega}\right)^2} \approx 1 - \frac{1}{2}\left(\frac{\omega_p}{\omega}\right)^2 \left(1 - \frac{a^2}{4}\right) \tag{1.59}$$

where we've used the result $\gamma = 1 + \boldsymbol{a}^2/2$ of our model of electron interacting with laser (1.21) and used gamma averaged over some time period to account for various electrons at different phases, that is $\gamma \to \langle\gamma\rangle = 1 + a^2/4$, valid for linear polarization. The ponderomotive force discussed previously can cause variations in the electron density. These density variations naturally correspond to variations in the refractive index (1.59), which causes perturbations in laser frequency. If we consider small perturbations of electron density δn_e and due frequency $\delta\omega$, we have $n_e \approx n_0 + \delta n_e$ and $\omega \approx \omega_0 + \delta\omega$. If we neglect second order perturbations we obtain the relativistic nonlinear refractive index of plasma

$$n \approx 1 - \frac{1}{2}\left(\frac{\omega_p}{\omega}\right)^2 \left(1 - \frac{a^2}{4} + \frac{\delta n_e}{n_0} - 2\frac{\delta\omega}{\omega_0}\right) \tag{1.60}$$

Self-focusing

The increase in relativistic mass with intensity (1.21) produces intensity dependence in refractive index. If we consider a laser pulse with gaussian spatial distribution $a(r) = a_0 e^{-(r/w_0)^2}$, the refractive index gains transverse dependence

$$\frac{\partial n}{\partial r} \doteq \frac{1}{4}\left(\frac{\omega_p}{\omega}\right)^2 \frac{\partial a(r)}{\partial r} < 0 \tag{1.61}$$

where we've neglected small perturbations of density from ponderomotive force $\partial \delta n_e / \partial r \doteq 0$ and used $\partial a / \partial r < 0$. (1.61) tells us that laser wavefront becomes curved in relativistic plasma since phase velocity increases further away from propagation axis. This effect is called *relativistic self-focusing*. Relativistic cold plasma essentially acts as a convex lens. Critical laser power P_c necessary for self-focusing to overpower laser diffraction to achieve self-guiding was shown to be [41].

$$P_c = \frac{8\pi\epsilon_0 c^5 m_e^2}{e^2}\left(\frac{\omega}{\omega_p}\right)^2 \doteq 17\left(\frac{\omega}{\omega_p}\right)^2 \text{ [GW]} = 17\left(\frac{n_c}{n_e}\right) \text{ [GW]} \tag{1.62}$$

Refractive index also depends on electron density modulations from ponderomotive force (1.60), therefore critical power necessary to achieve self-guiding is slightly decreased due to the fact that electrons are pushed from the regions of high intensity and therefore generate higher density off-axis $\partial n / \partial r \sim -\partial \delta n_e / \partial r < 0$. Due to this *ponderomotive self-focusing*, critical power necessary to achieve self-guiding is slighlty relaxed to [41]

$$P_c \doteq 16.8\left(\frac{\omega}{\omega_p}\right)^2 \text{ [GW]} \tag{1.63}$$

where ω is laser frequency. Self-focusing over tens of Rayleigh lenghts was observed in [42].

Self-compression

Refractive index (1.60) causes the pulse to *self-compress*. Shifting into the laser frame by substitution $\xi = z - ct$, the group velocity satisfies

$$\frac{\partial v_g}{\partial \xi} = c\frac{\partial n}{\partial \xi} =\sim \frac{1}{2}\frac{\partial a}{\partial \xi} - \frac{1}{n_0}\frac{\partial \delta n_e}{\partial \xi} = \begin{cases} \ll 0, & \text{at the pulse front} \\ > 0, & \text{at the pulse back} \end{cases} \tag{1.64}$$

the first case is due to the fact that for a guassian pulse $\partial a / \partial \xi < 0$ at the front. The ponderomotive force causes accumulation of electrons at the front edge and there is a steep plasma density increase $\partial \delta n_e / \partial \xi \gg 0$, which is the reason laser pulse compresses and dramatically steepens at the leading edge in plasma. In the second case, at the pulse back, once again $\partial a / \partial \xi < 0$. Small plasma density at the back is due to the fact that electrons are expelled from this region by ponderomotive force, therefore $\partial \delta n_e / \partial \xi \leq 0$. Such compression in plasma of 38 fs laser pulse to 10 - 14 fs was measured in [43].

Self-induced transparency

If a high intensity laser beam strikes a plasma target, electrons in the target may become accelerated due to the presence of the field as discussed in the previous subsections, increasing critical density observed in the laboratory frame (1.54) to

$$n_c' = \frac{\omega^2 m_e \gamma \epsilon_0}{e^2} = \gamma n_c \tag{1.65}$$

this effectively causes the target to become transparent for the high intensity laser beam, an effect called *self-induced transparency* [35].

Photon acceleration

Plasma naturally introduces dispersion through (1.57), the group velocity then tells us that high frequency waves travel faster than lower frequency waves within plasma. We might expect blueshift in the laser pulse front, but as we will see, this natural dispersion is outweighed within non-homogeneous plasma. Within the laser reference frame $\xi = z - ct$ we have

$$\frac{\partial \omega}{\partial \tau} \approx c \frac{\omega}{n^2} \frac{\partial n}{\partial \xi} \tag{1.66}$$

where we've estimated the change of frequency as $\Delta\omega = 2\pi c/\Delta\lambda$ with $\Delta\lambda = (-2\pi c^2/\omega^2)\Delta\omega = \Delta v_p \Delta\tau$, $\Delta v_p \approx \lambda \partial v_p/\partial z$ and used (1.55). Laser pulse propagating away from a co-propagating density decrease will therefore experience blueshift in time, this is called *photon acceleration*, evidence of which was found in [44]. However, high intensity pulses in plasma mostly experience an increasing density at the laser front due to ponderomotive force as discussed previously, in this case the dependency $\partial n/\partial \xi$ is completely identical in (1.66) as in (1.64) and we therefore conclude that high intensity laser pulses become redshifted at the front and blueshifted at the back while propagating in plasma, as was experimentally confirmed in [45].

1.2.4 Plasma Dynamics

To see the emergence of accelerating plasma wakefields from collective behaviour of electrons, we will first need to describe system consisting of many particle systems like electrons and ions. Since we're mostly interested in macroscopic quantities like density and related electromagnetic field, we don't have to consider a full microscopic description and a kinetic description based on particle distribution function $f(\boldsymbol{r}, \boldsymbol{p}, t)$ will suffice. Evolution of such a non-equilibrium thermodynamic system is generally described by the Boltzmann equation, but we're mostly interested in the response of the plasma to the propagating electromagnetic fields and therefore if we neglect the short-range Coulombic collisions between particles and work within field strengths where no particles are created or annihilated as mentioned in 1.1.3, we obtain the collisionless Boltzmann equation, also known as Vlasov equation

$$\frac{\mathbf{d}f(\boldsymbol{r}, \boldsymbol{p}, t)}{\mathbf{d}t} = \frac{\partial f}{\partial t} + \boldsymbol{v} \cdot \nabla_{\boldsymbol{r}} f + \boldsymbol{F} \cdot \nabla_{\boldsymbol{p}} f = 0 \tag{1.67}$$

which tells us that the distribution function is constant along any trajectory in phase space or equivalently that phase space volume occupied by a collection of particle systems evolving in time is constant. If we consider multiple particle systems, for example electrons and ions, distribution function of each particle system $f_i(\boldsymbol{r}, \boldsymbol{p}, t)$ must satisfy equation (1.67). Coupling Vlasov equations of the particle systems to the Maxwell equations gives the full kinetic description of plasma through the *Vlasov-Maxwell equations*

$$\boxed{\begin{aligned} \frac{\partial f_i}{\partial t} + \boldsymbol{v} \cdot \nabla_{\boldsymbol{r}} f_i + \frac{q_i}{m_i} (\boldsymbol{E} + \boldsymbol{v} \times \boldsymbol{B}) \cdot \nabla_{\boldsymbol{v}} f_i = 0 \\ \nabla \times \boldsymbol{E} = -\frac{\partial \boldsymbol{B}}{\partial t} \\ \nabla \times \boldsymbol{B} = \frac{1}{c^2} \frac{\partial \boldsymbol{E}}{\partial t} + \mu \boldsymbol{j} \\ \nabla \cdot \boldsymbol{E} = \frac{\rho}{\epsilon} \\ \nabla \cdot \boldsymbol{B} = 0 \end{aligned}} \tag{1.68}$$

where the current density $\boldsymbol{j}$ and charge density ρ are associated with the first two velocity moments of f_i as

$$\begin{aligned} \rho = \sum_i q_i n_i = \sum_i q_i \int f_i(\boldsymbol{x}, \boldsymbol{v}, t) \mathbf{d}^3 v \\ \boldsymbol{j} = \sum_i q_i n_i \overline{\boldsymbol{v}}_i = \sum_i q_i \int \boldsymbol{v} f_i(\boldsymbol{x}, \boldsymbol{v}, t) \mathbf{d}^3 v \end{aligned} \tag{1.69}$$

This Vlasov-Maxwell system of equations self-consistently describes dynamics of collisionless relativistic plasma on the kinetic scale if we neglect collisions, reaction forces or quantum effects. These effects can still be somehow included into the collisionless Boltzmann equation (1.67) through the force term, inclusion of

the collison term [35] or through Monte Carlo algorithms [46], [47]. Analytical solutions to these equations are extremely rare and for general boundary conditions they have to be solved numerically. Usually the way to solve them is through the Particle-In-Cell (PIC) method which we will describe in Chapter 3, where we will also present our numerical solutions to such equations.

Fluid Description

While numerical solutions of the Vlasov-Maxwell system (1.68) completely describe plasma dynamics on the kinetic scale, they are often computationally demanding and non-intuitive. We can however obtain analytic solutions if we make another reductive approximation from the microscopic description, where we move from the kinetic to the fluid description of plasma. The fluid model of plasma is an Eulerian description where we focus on macroscopic quantities of the particle distributions, which are the first velocity moments, respectively particle density, mean velocity density and energy density [35]. By integrating (1.67) over momentum, we get

$$\frac{\partial n}{\partial t} + \nabla \cdot (n\boldsymbol{v}) = 0 \tag{1.70}$$

which is the equation of continuity. By first multiplying (1.67) with $\boldsymbol{v}$ and then integrating over momentum, we also get

$$m_e \left(\frac{\partial \boldsymbol{v}}{\partial t} + \boldsymbol{v} \cdot \nabla \boldsymbol{v} \right) = -e(\boldsymbol{E} + \boldsymbol{v} \times \boldsymbol{B}) \tag{1.71}$$

which is the equation of motion for a fluid element. By combining these equations with Maxwell's equations where different species are coupled to each other and the electromagnetic fields through the source terms ρ and $\boldsymbol{j}$, we have a closed system of equations. This gives us hydrodynamic description of plasma.

1.2.5 Relativistic Nonlinear Plasma Waves

As we've briefly discussed in 1.2.2, we wish to describe the longitudal wakefields, which means we are mostly interested in describing an electrostatic wave propagating in relativistic plasma, which can be obtained by Gauss' law

$$\nabla \cdot \boldsymbol{E} = -\Delta\phi = \frac{\rho}{\epsilon} = \frac{-e(n_e - n_i)}{\epsilon} \tag{1.72}$$

where ρ is the charge density, n_e is the electron density and n_i is the ion density. Since we assume the ions to be a homogenously charged immobile background due to their heavy mass, ion density is unperturbed, constant, and equal to equilibrium electron density $n_i = n_0$. If we assume the wave to be propagating in the z direction, we can shift into the wave frame with $\xi = z - v_p t$, where v_p

is the phase velocity of the plasma wave (1.55). Spatial derivatives transform as $\partial_\xi = \partial_z$ and Poisson equation in the wave frame becomes

$$\frac{\partial^2 \phi}{\partial \xi^2} = \frac{e n_0}{\epsilon_0} \left(\frac{n_e}{n_0} - 1 \right) \tag{1.73}$$

To find the dependence of the electric potential ϕ on density perturbations n_e/n_0, we will work within the fluid description of plasma. We therefore need to include the continuity equation (1.70), which by transforming into the wave frame becomes

$$e v_p \frac{\partial n_e}{\partial \xi} + \frac{\partial \boldsymbol{j}}{\partial \xi} = 0 \tag{1.74}$$

for relativistic electrons propagating in the z direction, we have $j = -e n_e v_z$. After integration with the initial condition $n_e(\xi = 0) = n_0$, we get

$$n_e v_p - n_0 v_p = n_e v_z \rightarrow \frac{n_e}{n_0} = \frac{1}{1 - v_z/v_p} \approx \frac{1}{1 - \beta_z} \tag{1.75}$$

where we assumed the plasma waves to be relativistic $v_p \approx c$. This gives the Poisson equation (1.73) as

$$\frac{\partial^2 \overline{\phi}}{\partial \xi^2} = k_p^2 \left(\frac{1}{1 - \beta_z} - 1 \right) \tag{1.76}$$

where we introduced the plasma wave vector $k_p = \omega / v_p$ and the normalized electric potential $\overline{\phi} = e\phi / m_e c^2$ which is once again normalized to signify relativistic electric field potential energy, notably when $e\phi \gg m_e c^2$. Let us also note that since $\overline{p}_z = \gamma \beta_z$, we have

$$\frac{1}{1 - \beta_z} - 1 = \frac{\beta_z}{1 - \beta_z} \frac{\gamma}{\gamma} = \frac{\overline{p}_z}{\gamma - \overline{p}_z} \tag{1.77}$$

Now we only need to find how the normalized longitudal momentum $\overline{p}_z$ of the electrons generating current $\boldsymbol{j}$ depends on electric potential ϕ. With some work, we can retrieve this similarly to how we obtained momenta for an electron interacting with laser (1.18), (1.19), (1.20). The whole approach is completely analogic, except now we also have to include the longitudal electrostatic part described by the electric potential ϕ in the four-potential $A^\nu = (\phi/c, \boldsymbol{A})$. A very important observation in the following derivation comes from the fact that by $\boldsymbol{A} = (A_x, A_y, 0)$, we are describing the transverse electromagnetic wave that generates the plasma density perturbations through ponderomotive force. On the other hand by $\phi(z - v_p t)$, we only describe the electrostatic longitudal field response to these density perturbations, which are correlated through Poisson equation (1.76).

Now we proceed analogically as in 1.1.1, first by applying the Euler-Lagrange equations (1.3) on the Lagrangian (1.10). With the electric potential included in the four-potential, we get

$$p_x = eA_x \tag{1.78}$$

$$p_y = eA_y \tag{1.79}$$

$$\frac{\mathbf{d}p_z}{\mathbf{d}t} = -e\boldsymbol{v}\frac{\partial \boldsymbol{A}}{\partial z} + e\frac{\partial \phi}{\partial z} \tag{1.80}$$

$$\frac{\mathbf{d}}{\mathbf{d}t}(\gamma m_e c^2 - e\phi) = e\boldsymbol{v}\frac{\partial \boldsymbol{A}}{\partial t} - e\frac{\partial \phi}{\partial t} \tag{1.81}$$

once again by combining the last two equations and using the chain rule $\partial/\partial t = -c\partial/\partial z$ valid for modes propagating in the positive direction, we get a new constant of motion, which also includes the electric potential

$$\frac{\mathbf{d}}{\mathbf{d}t}(\gamma m_e c^2 - cp_z - e\phi) = 0 \tag{1.82}$$

After integration this becomes in normalized units

$$\gamma = 1 + \overline{\phi} + \overline{p}_z \tag{1.83}$$

By squaring γ, we have

$$\gamma^2 = (1 + \overline{\phi} + \overline{p}_z)^2 = (1 + \overline{\phi})^2 + 2(1 + \overline{\phi})\overline{p}_z + \overline{p}_z^2 \tag{1.84}$$

Energy-momentum relation $E^2 = (pc)^2 + (m_0c^2)^2$ with the combination of (1.78), (1.79) produces in normalized units

$$\gamma^2 = 1 + \overline{\boldsymbol{p}}^2 = 1 + \boldsymbol{a}^2 + \overline{p}_z^2 \tag{1.85}$$

If we equate (1.84) and (1.85) and solve for $\overline{p}_z$, alas, we obtain the dependence of the longitudal momentum of the electrons on the normalized electric potential

$$\overline{p}_z = \frac{1 + \overline{\phi}}{2}\left(\frac{1 + a^2}{(1 + \overline{\phi})^2} - 1\right) \tag{1.86}$$

Now that we know the dependence of the longitudal momentum, the Poisson equation (1.76) with the fact that $\gamma - \overline{p}_z = 1 + \overline{\phi}$ becomes thanks to (1.77)

$$\boxed{\frac{\partial^2 \overline{\phi}}{\partial \xi^2} = \frac{k_p^2}{2}\left(\frac{1 + a^2}{(1 + \overline{\phi})^2} - 1\right)} \tag{1.87}$$

which is the *relativistic non-linear one-dimensional plasma wave equation.*

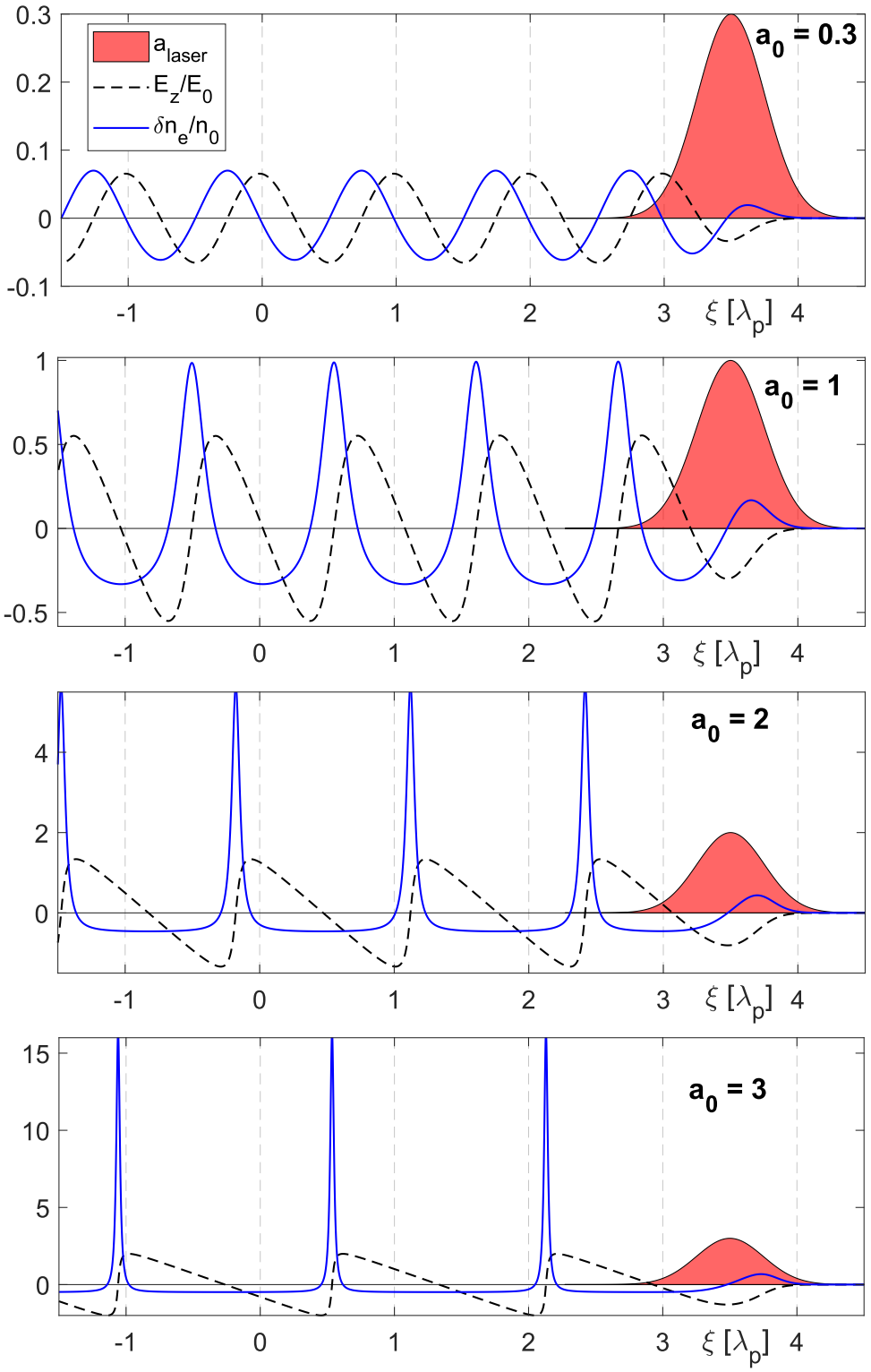

Figure 1.6: Solutions to the relativistic plasma wave equation (1.87) with increasing laser strength. n_0 is the equilibrium electron density and $E_0 = m_e\omega_p c/e$ is the non-relativistic wavebreaking limit (1.90).

Solving equation (1.87) gives us the normalized electric potential $\overline{\phi}$ due to presence of the laser pulse described by $a(\xi)$. First derivative of the potential in the direction of propagation gives us the electric field of the plasma wave, the second derivative gives us the perturbed density $\delta n_e = n_e - n_0$ through equation (1.73). If we describe the laser pulse as $a(\xi) = a_0 e^{-2(\xi/\pi)^2}$, which corresponds to the pulse length condition $c\tau_L = \lambda_p/2$, we obtain with increasing laser field strength solutions shown in 1.6. Fig. 1.7 shows that the following pulse length condition must be satisfied for optimal wakefield generation

$$\boxed{\tau_L \simeq \frac{\tau_p}{2} = \frac{\lambda_p}{2c}} \tag{1.88}$$

This condition characterizes the resonance between the ponderomotive force and the oscillatory response of electrons [48].

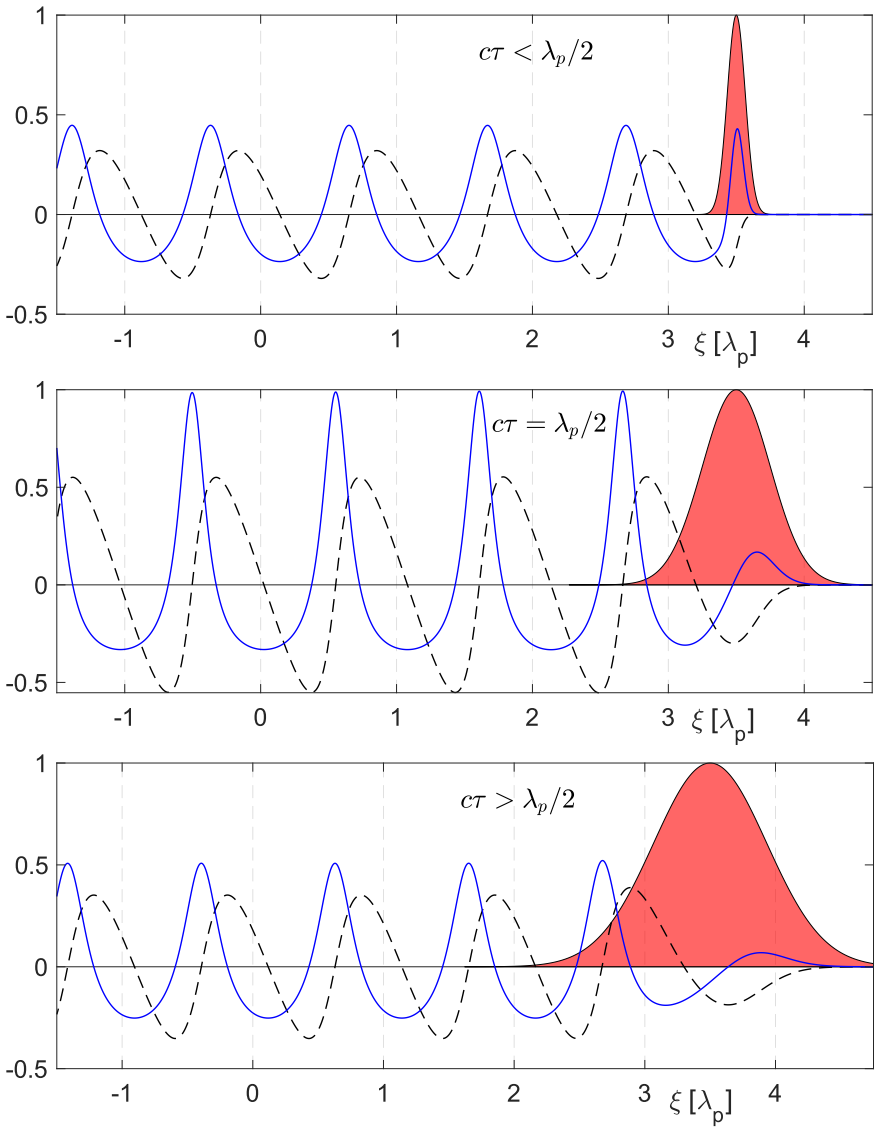

Figure 1.7: Plasma wakefield response to variations of pulse length. $a_0 = 1$, $c\tau = 0.3, 1, 1.6 \cdot \lambda_p/2$.

Fig. 1.6 show us that within the non-relativistic peak laser strength $a_0 < 1$, we're observing linear response of the plasma and the electrons are oscillating in a sinusoidal fashion. Entering the relativistic regime produces sharp electron density peaks and the plasma wave assumes a sawtooth-like shape. Equations (1.73) and (1.76) tell us that

$$\frac{n_e}{n_0} \sim \frac{\partial^2 \phi}{\partial \xi^2} \sim \frac{1}{1-\beta_z} \to \infty \iff \beta_z = v_e/v_p \to 1 \tag{1.89}$$

This tells us that as the phase velocity of the individual electrons that build the plasma wave approaches phase velocity of the plasma wave $v_e \to v_p$, the sharp plasma density peaks become unbounded $n_e \to \infty$. This is called *wavebreaking*, since the phase velocity of individual electrons reaches or overtakes the phase velocity of the plasma wave and thus the longitudal electrostatic plasma wave breaks, similarly to an ocean wave crashing upon a beach. This mechanism also sets the *cold relativistic wavebreaking limit*, which dictates the maximum attainable longitudal electrostatic field of the plasma wave in cold plasma as [49]

$$\boxed{E_0^{max} = \frac{m_e \omega_p c}{e}\sqrt{2(\gamma_p - 1)}} \tag{1.90}$$

where $\gamma_p = (1-\beta_p^2)^{-1/2} = \omega/\omega_p$ due to (1.55). (1.90) gives us a simple tool to check for the maximum possible theoretically achievable accelerating gradient. As an example, let us consider Ti:Sapphire laser with central wavelength of 0.808 μm shooting into a gas target with particle density 5×10^{18} cm^{-3}, this gives us $\gamma_p \doteq 5.8$ and the maximum achievable electric intensity of the plasma wave is therefore $E_0^{max} \doteq 2$ TV/m. We will briefly remind the kind reader that previous analysis of laser wakefields was only considered in the 1D case. The complete 3D description must be solved numerically as done in Chapter 3. We must however mention the *blowout regime*, in which a laser pulse with $a_0 \geq 2$ generates approximatelly spherical plasma cavity with radius r_b, as shown in introduction of this thesis on Fig. 6. This bubble shape is assumed when the ponderomotive force acting on the electrons is balanced by the radial electrostatic attraction caused by the ions behind the laser pulse. Through 3D simulations it was found in [50] that this balance emerges when the laser waist w_0 satisfies

$$\boxed{k_p r_b \approx k_p w_0 = 2\sqrt{a_0}} \tag{1.91}$$

Within this blowout regime, electrons experience a radial electrostatic force from the ions, keeping the electrons that are injected into the accelerating phase roughly on axis, which makes this scheme ideal for acceleration due to reduced transverse emittance. (1.88) and (1.91) combined with sufficient laser strength $a_0 \geq 2$ give us three rules of thumb for achieving optimal electron laser wakefield acceleration. We've shown that enormous accelerating gradients can be generated within these laser produced plasma wakefields, however as is the case in other contemporary accelerators, particles to be accelerated need to be injected into the accelerating phase of the field. In the next section, we will see that although wavebreaking limits the maximum electric intensity of the plasma wave, it provides one of the methods for such electron injection.

1.2.6 Electron Trapping

As we've previously mentioned, electrons need to be trapped within the accelerating phase of the field to accelerate and gain energy. We will follow the results of [51] to characterize this trapping into the accelerating phase. The Hamiltonian of a relativistic electron in a plasma wave transformed into the wave frame is

$$H(\xi, p_z) = \gamma m_e c^2 (1 - \beta_z \beta_p) - e\phi \tag{1.92}$$

Where $\beta_p = v_p c$ is the normalized phase velocity of the plasma wave. Since the total mechanical energy along any electron trajectory doesn't change, the Hamiltonian is constant and we can rewrite it in terms of the normalized electron momentum $\overline{p}_z$

$$\overline{H} + \overline{\phi} = \gamma - \overline{p}_z \beta_p = \sqrt{1 + \overline{p}_z^2} - \overline{p}_z \beta_p \tag{1.93}$$

where we've introduced the normalized Hamiltonian $\overline{H} = H/(m_e c^2)$. Solving the equation for $\overline{p}_z$ gives

$$\overline{p}_z = \beta_p \gamma_p^2 \left(\overline{H} + \overline{\phi}\right) \pm \gamma_p^2 \sqrt{\left(\overline{H} + \overline{\phi}\right)^2 - 1/\gamma_p^2} \tag{1.94}$$

Employing the potential $\overline{\phi}$ for $a_0 = 0.2$ obtained from solving (1.87) produces phase space evolution for electrons with various initial energies by setting different initial kinetic energy thanks to the conservation of energy for every trajectory $\overline{H} = \overline{H}_0 = const$. Different trajectories are sampled like this in Fig. 1.8.

We can see that there are two kinds of trajectories, closed (solid black) and open (dashed black) orbits which are separated by a *separatrix* (red). The separatrix trajectory is obtained when an electron is moving within minimum of the plasma wave potential. That means it's Hamiltonian satisfies $H_s = 1/\gamma_p - \overline{\phi}_{min}$. The open orbits $H_0 < H_s$ correspond to electrons conducting fluid motion within the plasma wave whose initial energy was either too small or too high to be trapped by the longitudal field. The orbits close when $H_0 > H_s$, which corresponds to the case of electrons that have just right initial kinetic energy, therefore they are trapped by the plasma wave. To see that these electrons are accelerated inside the plasma, let us assume that an electron has initial velocity $\beta_z < \beta_p$ and large enough initial energy to become trapped, then it will eventually start gaining energy, reaching a point when $\beta_z = \beta_p$ (green arrow tip). Subsequent energy gain results in $\beta_z > \beta_p$ and the electron obtains maximum energy at some point during it's evolution (blue arrow tip). At this point the acceleration should ideally stop, however without any changes to the system the electron begins losing energy (red arrow tip), giving it back to the plasma wave, which eventually completes the rotation in phase space. This deceleration is known as *dephasing* and is one of the limitations of energy gain, it can be however prevented through various methods, such as tuning the plasma density and target length to prevent it completely.

We can see that wavebreaking is a necessary condition for acceleration, since for both $\beta_z > \beta_p$. As seen in Fig 1.8, the separatrix orbit is the one that requires least initial kinetic energy and produces the most energy from all the closed orbits.

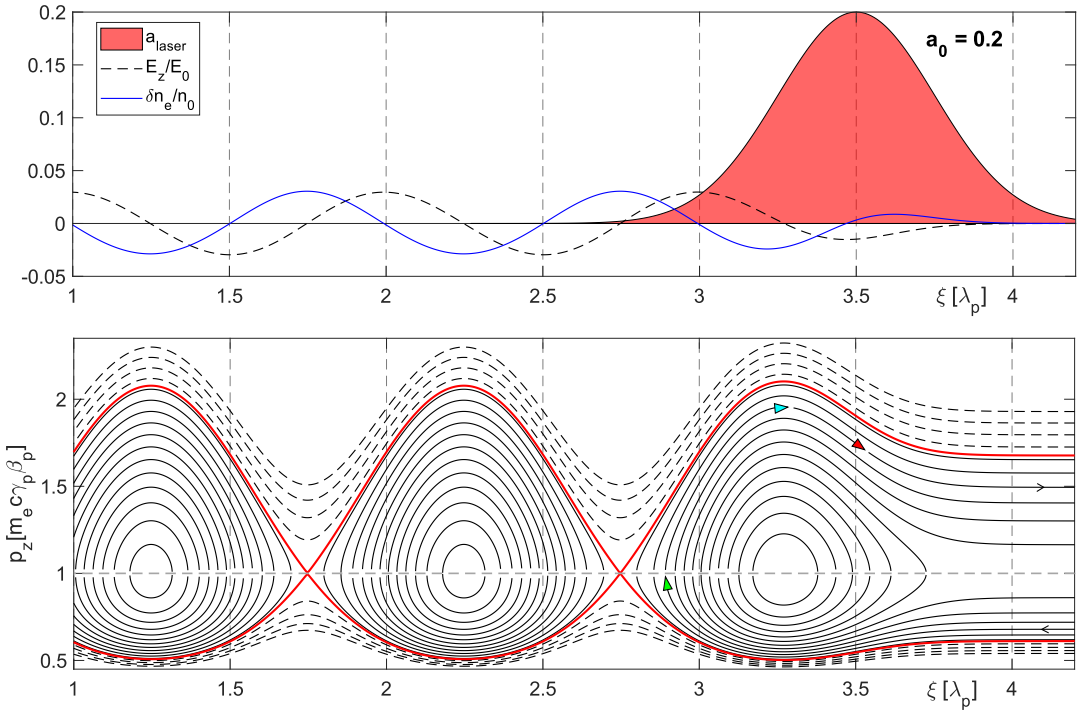

Figure 1.8: Top: Wakefield excitation as shown in previous figures. Bottom: Corresponding phase space (ξ, p_z) evolution of electrons with different initial energies. Each line is electron trajectory corresponding to different initial energy. Description in text.

The conditions for electron trapping can be also summarized generally in 3D, as was done in [52]. The first condition also results from our previous analysis and that is that the trapped electrons must have axial velocity larger than the phase velocity of the plasma wave $v_z > v_p$. The second condition dictates that the trapped electron trajectories cross the plasma sheath. This comes from the ponderomotive force, which forces electrons from near the radial axis to cross electrons from the plasma sheath. They can then be attracted inwards and arrive on axis before the bulk of the electrons that constitute the sheath. These conditions are generally satisfied when there are large wake amplitudes, which facilitates easier wavebreaking, therefore large $a_0 \geq 2$ is often necessary. Plasma density n_e determines the phase velocity of the plasma wave v_p, which decreases with decreasing density, therefore trapping of accelerated electrons is also favorable with sudden density decrease. These conditions have been experimentally shown to be satisfied when the laser power satisfies [53]

$$P > \frac{P_c}{16}\left(\ln\left(\frac{2n_c}{3n_e}\right) - 1\right)^3 \tag{1.95}$$

where P_c is the critical power necessary for self-focusing (1.62).

1.2.7 Electron Injection

In previous section we've talked about how electrons can be trapped within the accelerating regime and mostly we've described a regime where an electron has enough initial kinetic energy to be broken out of the plasma fluid motion within the wakefield and become trapped without any external changes to the physical system, this is called *Self-injection*. The downside of this method is that the electron self-injection occurs in random phase of the plasma wave and therefore is difficult to control. These random injections result in an electron beam with a high relative energy spread. Large advantage of this scheme is the fact that it all occurs inherently within one laser shot and doesn't necessiate any temporal synchronization of the laser [54].

Ionization injection occurs when we mix a light gas, for example He, with a heavier gas like O, N, Ar. This technique is based on the fact that the laser pulse ionizes the lighter gas and the L-shell electrons of the heavier gas to create plasma, but the peak intensity inside the laser pulse is also high enough to allow for tunnel ionization of the K-shell electrons from the heavier gas, allowing for spatially controlled electron injection directly into the accelerating phase. This method generates temporally and spatially well defined electron beams, often also with small relative energy spread compared to self-injection [55].

Optical injection is a scheme where a second laser pulse triggers the electron injection. The second laser is often propagating at an angle to the main laser which excites the wakefield. The second pulse's ponderomotive force can perturb the plasma sheath enough to break out electrons and allow them to inject into the accelerating phase. The second pulse must not be too strong otherwise it may destroy the wakefield [27].

Density modulation injection occurs when we work with a non-homogeneous gas density target and use additional tools like wires across the target to create density bow shocks, tilting the gas nozzle to create density ramps or utilize a custom manufactured gas nozzle with tailored gas density [56], [57]. All of this allows us to tune density and therefore plasma wave phase velocity, which allows us to define spatial regions where wavebreaking and therefore trapping occurs due to sudden plasma wave phase velocity changes [58].

2. Electromagnetic Radiation from Relativistic Electrons

In the introduction, we've alredy briefly mentioned the fact that relativistic electrons within the accelerating phase oscillate transversely, due to the distribution of charge. In this section, we will describe how charged particles generate radiation and we will especially analyze the special case of an electron undertaking transverse oscillations.

Maxwell's equations with the application of Lorenz gauge condition $\partial_\mu A^\mu = 0$ produce, as in (1.12), the non-homogeneous wave equation

$$\Box A^\nu = -\mu J^\nu \tag{2.1}$$

This equation is Lorentz covariant, but this more importantly also means that all changes within the potentials travel at the speed of light. General solution to the non-homogeneous wave equation is found by convolving the right hand side of (2.1) with the Green function of (2.1), which is the solution of

$$\Box G(\boldsymbol{r}, t) = \delta(\boldsymbol{r})\delta(t) \tag{2.2}$$

Through Fourier transform, it can be found to be

$$G(\boldsymbol{r}, t) = \frac{1}{4\pi|\boldsymbol{r}|}\delta\left(t - \frac{|\boldsymbol{r}|}{c}\right) \tag{2.3}$$

the solution to (2.1) for arbitrary source configuration is therefore

$$A^\nu(\boldsymbol{r}, t) = \mu(G \star J^\nu) = \frac{\mu}{4\pi}\int \frac{J^\nu(\boldsymbol{r}', t')}{|\boldsymbol{r} - \boldsymbol{r}'|}\delta\left(t - t' - \frac{|\boldsymbol{r} - \boldsymbol{r}'|}{c}\right)\mathbf{d}t'\mathbf{d}^3r' \tag{2.4}$$

2.1 Radiation from a Moving Charge

Electron is considered to be an elementary particle within the Standard Model, which makes it a non-composite point charge. We can therefore describe the source terms for a relativistic charge, such as electron, moving with arbitrary trajectory $\boldsymbol{x}(t)$ and velocity $\boldsymbol{v}(t) = c\boldsymbol{\beta}(t)$ as

$$\begin{aligned} \rho(\boldsymbol{r}, t) &= q\delta(\boldsymbol{r} - \boldsymbol{x}(t)) \\ \boldsymbol{j}(\boldsymbol{r}, t) &= qc\boldsymbol{\beta}(t)\delta(\boldsymbol{r} - \boldsymbol{x}(t)) \end{aligned} \tag{2.5}$$

plugging (2.5) into (2.4) and evaluating the integral, which is done in Appendix A.5, gives the famous Liénard-Wiechert potentials for a moving charge

$$\phi(\boldsymbol{r},t) = \frac{q}{4\pi\epsilon_0}\left[\frac{1}{(1-\boldsymbol{\beta}\cdot\boldsymbol{n})|\boldsymbol{R}|}\right]_{ret.} \tag{2.6}$$

$$\boldsymbol{A}(\boldsymbol{r},t) = \frac{qc\mu_0}{4\pi}\left[\frac{\boldsymbol{\beta}}{(1-\boldsymbol{\beta}\cdot\boldsymbol{n})|\boldsymbol{R}|}\right]_{ret.} \tag{2.7}$$

where $\boldsymbol{R}(t) = \boldsymbol{r} - \boldsymbol{x}(t)$ is the distance vector between the observer and the radiating charge and $\boldsymbol{n}(t) = \boldsymbol{R}(t)/|\boldsymbol{R}(t)|$ is the direction towards observer. Both potentials are evaluated at retarded time t', which is the time at which the signal reaches the observer

$$t' = t - |\boldsymbol{r} - \boldsymbol{x}(t)|/c \tag{2.8}$$

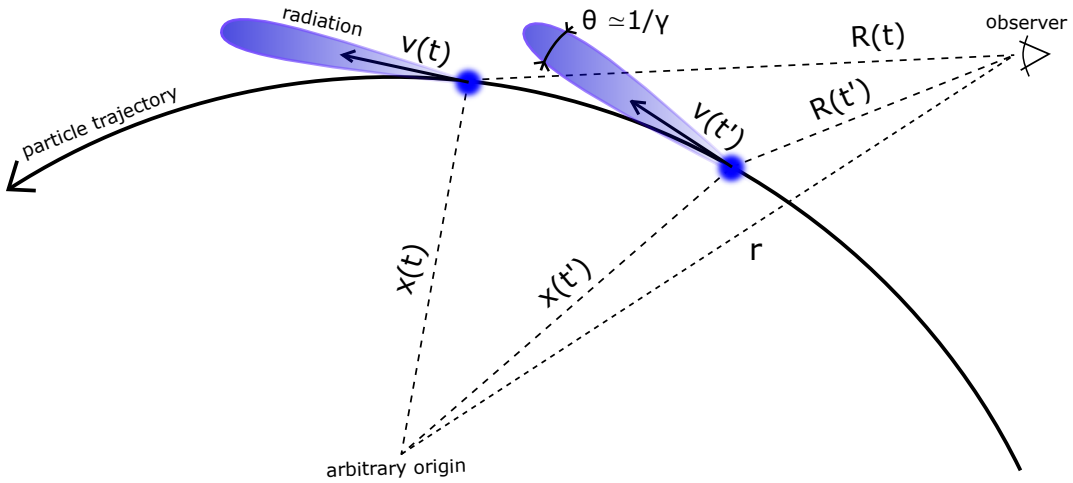

Figure 2.1: A charged particle travelling in the present at $\boldsymbol{x}(t)$ is seen by the observer to be at $\boldsymbol{x}(t')$ due to the fact that the radiation signal travels at finite speed of light c. At each instantaneous moment, radiation of a relativistic charge is emitted in a collimated forward cone with opening angle $\theta \simeq 1/\gamma$.

From the definition of potentials, we obtain the electric and magnetic fields of a moving charge as

$$\boldsymbol{E}(\boldsymbol{r},t) = \frac{q}{4\pi\epsilon_0}\left[\frac{\boldsymbol{n}-\boldsymbol{\beta}}{\gamma^2|\boldsymbol{R}|^2(1-\boldsymbol{n}\cdot\boldsymbol{\beta})^3} + \frac{\boldsymbol{n}\times((\boldsymbol{n}-\boldsymbol{\beta})\times\dot{\boldsymbol{\beta}})}{c|\boldsymbol{R}|(1-\boldsymbol{n}\cdot\boldsymbol{\beta})^3}\right]_{ret.} \tag{2.9}$$

$$\boldsymbol{B}(\boldsymbol{r},t) = -\frac{qc\mu_0}{4\pi}\left[\frac{\boldsymbol{n}\times\boldsymbol{\beta}}{\gamma^2|\boldsymbol{R}|^2(1-\boldsymbol{n}\cdot\boldsymbol{\beta})^3} + \frac{\boldsymbol{n}\times(\dot{\boldsymbol{\beta}}+\boldsymbol{n}\times(\boldsymbol{\beta}\times\dot{\boldsymbol{\beta}}))}{c|\boldsymbol{R}|(1-\boldsymbol{n}\cdot\boldsymbol{\beta})^3}\right]_{ret.} \tag{2.10}$$

It's easy to check that $\boldsymbol{B} = (\boldsymbol{n}\times\boldsymbol{E})/c$ holds. Let us now discuss the two terms in these fields. We can see that in the rest frame of the particle, $\boldsymbol{\beta}, \dot{\boldsymbol{\beta}} = 0$, the magnetic field and the second term of the electric field is zero and the first term reduces to the electrostatic Coulomb law. With constant velocity, the term gets

diminished by γ^2 and the field is tilted in the direction of particle propagation by $\boldsymbol{n}-\boldsymbol{\beta}$ in the numerator. This first term is therefore the generalized relativistic Coulomb law for a moving charge. Similarly, the first term in the magnetic field is the generalized relativistic Biot-Savart law. The second terms are the only ones that depend on acceleration, which means that they are responsible for the dynamic changes in fields, which is electromagnetic radiation. It is also clear that these second terms become dominant far away from the charged particle $|\boldsymbol{R}| \gg 1$. If the charged particle is relativistic, the static terms of the fields can also be neglected. Being interested only in the radiation by relativistic charged particles, we can safely neglect these terms. If we denote the second terms as $\boldsymbol{E}_{rad}$, $\boldsymbol{B}_{rad}$, it can be easily checked that these raditative fields are indeed perpendicular to the radiation propagation direction $\boldsymbol{n}$

$$\boldsymbol{n}\cdot\boldsymbol{E}_{rad}=\boldsymbol{n}\cdot\boldsymbol{B}_{rad}=0 \tag{2.11}$$

The radiative energy flux is then given by the Poynting vector as

$$\boldsymbol{S}(\boldsymbol{r},t)=\frac{1}{\mu_0}\boldsymbol{E}_{rad}\times\boldsymbol{B}_{rad}=\frac{1}{\mu_0 c}\boldsymbol{E}_{rad}\times(\boldsymbol{n}\times\boldsymbol{E}_{rad})=\sqrt{\frac{\epsilon_0}{\mu_0}}\left[|\boldsymbol{E}_{rad}|^2\boldsymbol{n}\right]_{ret.} \tag{2.12}$$

The magnitude of the energy flux in the direction of propagation $\boldsymbol{n}$ is then

$$\boldsymbol{S}\cdot\boldsymbol{n}=\frac{q^2}{16\pi^2\epsilon_0 c}\left(\frac{\boldsymbol{n}\times((\boldsymbol{n}-\boldsymbol{\beta})\times\dot{\boldsymbol{\beta}})}{|\boldsymbol{R}|(1-\boldsymbol{n}\cdot\boldsymbol{\beta})^3}\right)^2_{ret.} \tag{2.13}$$

The total power radiated per unit solid angle follows

$$\frac{\mathbf{d}^2W}{\mathbf{d}\Omega\mathbf{d}t}=\left[|\boldsymbol{R}|^2(\boldsymbol{S}\cdot\boldsymbol{n})\right]_{ret.}=c\epsilon_0\left[|\boldsymbol{E}_{rad}\cdot\boldsymbol{R}|^2\right]_{ret.} \tag{2.14}$$

A lenghty integration over the solid angle yields the total radiated power by the charged particle in the form [28]

$$\boxed{\mathcal{P}_{rel.}=\frac{\mathbf{d}W}{\mathbf{d}t}=\frac{q^2}{6\pi\epsilon_0 c}\gamma^6\left(\dot{\boldsymbol{\beta}}^2-|\boldsymbol{\beta}\times\dot{\boldsymbol{\beta}}|^2\right)} \tag{2.15}$$

which validates our comments about Lorentz invariance of radiated power (1.41), discussion of the features of the total radiated power is the same. We also point out that the non-relativistic limit $\beta \ll 1$ reduces (2.15) to the well known classical Larmor's formula (1.37). We are often more interested in spectral distribution of radiated energy, which can be retrieved from Plancherel's theorem ($\star$)

$$\begin{aligned}\frac{\mathbf{d}W}{\mathbf{d}\Omega}&=\int_{-\infty}^{\infty}\frac{\mathbf{d}^2W}{\mathbf{d}\Omega\mathbf{d}t}\mathbf{d}t=c\epsilon_0\int_{-\infty}^{\infty}|\boldsymbol{R}\cdot\boldsymbol{E}_{rad}|^2(t)\mathbf{d}t\\&\overset{(\star)}{=}\frac{c\epsilon_0}{2\pi}2\int_0^{\infty}\mathcal{F}|\boldsymbol{R}\cdot\boldsymbol{E}_{rad}|^2(\omega)\mathbf{d}\omega=\int_0^{\infty}\frac{\mathbf{d}^2W}{\mathbf{d}\Omega\mathbf{d}\omega}\mathbf{d}\omega\end{aligned} \tag{2.16}$$

where we've used the fact since the integrand $f(t)$ is real, $f(-\omega) = f^*(\omega)$ and $|f(\omega)|^2$ is even in ω. This allowed us to reduce the integration domain to non-negative values. The angular spectral distribution of radiated energy is then

$$\boxed{\frac{\mathbf{d}^2W}{\mathbf{d}\Omega\mathbf{d}\omega} = \frac{c\epsilon_0}{\pi}\left|\mathcal{F}\left[\boldsymbol{R}\cdot\boldsymbol{E}_{rad}\right]_{ret.}\right|^2} \tag{2.17}$$

With the knowledge of position, velocity and acceleration of a moving charged particle, (2.17) completely describes the angular spectral distribution. By plugging $\boldsymbol{E}_{rad}$ into (2.17), we get the well known *radiation integral* [28] [59]

$$\frac{\mathbf{d}^2W}{\mathbf{d}\Omega\mathbf{d}\omega} = \frac{q^2}{16\pi^3\epsilon_0 c}\left|\int_{-\infty}^{\infty}\frac{\boldsymbol{n}\times((\boldsymbol{n}-\boldsymbol{\beta})\times\dot{\boldsymbol{\beta}})}{(1-\boldsymbol{n}\cdot\boldsymbol{\beta})^2}e^{i\omega(1-\boldsymbol{n}\cdot\boldsymbol{R}/c)}\mathbf{d}t\right|^2 \tag{2.18}$$

which is entirely evaluated within the retarded time t'. Integral (2.18) can be used to characterize some basic features of radiation emitted by charged particles. Finding analytic solutions to this integral is generally very hard and it is usually solved numerically [60]. We also note that numerically computing the Fourier transform in (2.17) directly is a viable and equivalent alternative to numerical solutions of (2.18). We have used the first approach based on (2.17) to produce radiation results in Chapter 3.

Without any analytic computation of the integral (2.18), let us first proceed to point out some characteristics of radiation of relativistic electrons that the integrand indicates. The denominator in the integrand tells us that most energy is radiated in the direction of electron's velocity and that relativistic electrons radiate dramatically more, since $\mathbf{d}^2W/\mathbf{d}\Omega\mathbf{d}\omega \to \infty \iff \boldsymbol{\beta}\cdot\boldsymbol{n} \to 1 \iff \boldsymbol{\beta} \sim 1 \wedge \boldsymbol{\beta} \parallel \boldsymbol{n}$. From the numerator, we also see that radiation vanishes for zero acceleration $\dot{\boldsymbol{\beta}} = 0$. Therefore we see that, as expected, acceleration is responsible for radiation generation. The expression $(\boldsymbol{n}-\boldsymbol{\beta})\times\dot{\boldsymbol{\beta}}$ also tells us that transverse acceleration generates more radiation than longitudal acceleration. Lastly, the phase factor $\exp[i\omega(t-|\boldsymbol{R}|/c)]$ can give us an estimate for the frequency of emitted radiation. Observing the field near electron $|\boldsymbol{r}-\boldsymbol{x}(t)| = \Delta x \ll 1$ allows us to approximate $\omega(1-|\boldsymbol{R}|/tc) \approx \omega(1-\beta)$. Integration over time is maximized only when the exponential phase factor and the integrand, excluding the exponential, oscillate at the same frequency. Therefore, if the electron oscillates along it's propagation with some frequency ω_e, the integration and therefore radiated energy is maximized for radiation at frequencies near $\omega \doteq \omega_e/(1-\beta) \sim 2\gamma^2\omega_e$. This tells us that the frequency of the emitted radiation, as observed within the laboratory frame, is double Doppler upshifted from the frequency of the electron's motion.

Previous estimate tells us that X-ray radiation in the exahertz region can be generated by electrons oscillating along their propagation with $\sim$ cm wavelengths. If these electron trajectories were also mostly longitudal, we could possibly create a very collimated X-ray beam. As we have foreshadowed in the introduction, such beams can be generated by electrons being accelerated through laser wakefields, as we will show in the following section.

Before we conclude this section, we have to mention the effects of Lorentz transformation through relativistic aberration on observed radiation emitted by charged particles. Let us consider an inertial frame where the observer and a charged partcile don't move longitudally and the charge oscillates transversally. This acceleration generates radiation that has a doughnut-like appearance, which can be easily checked by plugging the sinusoidal acceleration into the Larmor formula (1.37). The emitted power is then $\mathcal{P} \sim \sin^2(\theta')$, which gives the distintinctive look portrayed in figure 2.2 [59].

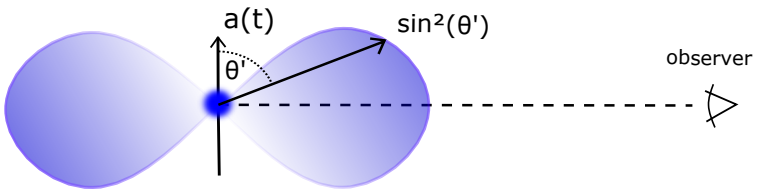

Figure 2.2: Radiation pattern as seen in the average electron drift frame where the longitudal velocity is zero.

If the observer now moves into the laboratory frame of reference, the emitted power gets folded into a narrow forward radiation cone [59]. A simple argument for this can be made through Lorentz transformation. In [59], it is shown that the angles that are measured from the direction of motion are related due to relativistic aberration as

$$\tan\theta = \frac{\sin\theta'}{\gamma(\beta + \cos\theta')} \tag{2.19}$$

where the angle θ corresponds to the average drift frame portrayed in figure 2.2 and θ' corresponds to the laboratory frame of reference portrayed in figure 2.3. For a highly relativistic electron, we have $\beta \doteq 1$ and $\gamma \gg 1$, thus for radiation emitted at arbitrarily large angles θ' in the electron frame, the corresponding angle θ at which we observe the emitted radiation within the laboratory frame of reference becomes

$$\boxed{\theta \simeq \frac{1}{2\gamma}} \tag{2.20}$$

which means that for a relativistic charged particle, the radiation is collimated to a cone with half opening angle (2.20). This radiation pattern is often described as a *"searchlight beam"* [59].

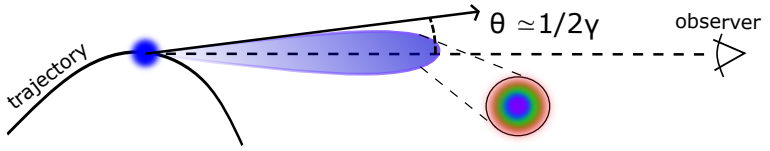

Figure 2.3: Radiation pattern as seen in the laboratory frame of reference. The inset shows that maximum photon energy drops off-axis.

2.2 Radiation from Wakefield Electrons

Radiation generated by laser wakefield accelerated electrons has many features which can be related to synchrotron radiation [23], [24], [25], [26], [28]. We will now proceed to solve the equations of motion for an electron travelling within the wakefield in simplified geometry and then provide these solutions for (2.18) to obtain angularly resolved spectral distribution of radiated energy. We will simplify the problem by working in cylindrical coordinates. The electrostatic potential affecting the accelerated electron can be found by solving the Poisson's equation

$$\frac{1}{r}\frac{\partial}{\partial r}\left(r\frac{\partial \phi}{\partial r}\right) = \frac{e(n_e - n_0)}{\epsilon} \Longrightarrow \phi = -r^2\frac{en_0}{4\epsilon} \tag{2.21}$$

Where we've assumed that the electron will be moving inside the ion cavity, therefore $n_e \approx 0$. We further simplify this problem by considering the potential in (2.21) as the source of the radial restoring force of the ion channel and include the acceleration in the form of a longitudal constant electric field E_z. By including these terms into the Lagrangian (1.10), we get from the Euler-Lagrange equations, in observer time and rewritten to normalized units,

$$\frac{\mathbf{d}}{\mathbf{d}t}(\gamma m_e \dot{r}) = -\frac{en_0}{2\epsilon}r \tag{2.22}$$

$$\frac{\mathbf{d}}{\mathbf{d}t}(\gamma m_e \dot{z}) = eE_z \tag{2.23}$$

Let us first consider an alredy accelerated relativistic particle close to dephasing, that is oscillating with small amplitude. Then $E_z \approx 0$ and we have $\dot{\gamma} \approx 0$, therefore

$$\frac{\mathbf{d}}{\mathbf{d}t}(\gamma \dot{r}) = \dot{\gamma}\dot{r} + \gamma\ddot{r} \approx \gamma\ddot{r} \tag{2.24}$$

then (2.22) becomes

$$\ddot{r} + \omega_\beta^2 r = 0 \tag{2.25}$$

where $\omega_\beta = \omega_p/\sqrt{2\gamma}$ is the betatron frequency. The solution shows that the electron is conducting radial *betatron oscillations*

$$r = r_\beta \sin(\omega_\beta t) \tag{2.26}$$

where r_β is the amplitude of the betatron oscillations, which is related to the maximum normalized electron transverse momentum, called *betatron strength parameter* $K_\beta = \gamma\beta_r^{max} = \gamma r_\beta k_\beta$. As we will see, this parameter distinguishes various radiation regimes. In this ultra relativistic limit, it can be perturbatively shown that these transverse oscillations modify the longitudal motion and a familiar figure-of-eight motion, as seen in 1.1.1, is conducted [23]. If we consider

an electron that is still under the effect of the strong accelerating field $E_z \neq 0$, then we have to consider (2.23) without any approximations. Then we have from (2.23)

$$\frac{\mathbf{d}}{\mathbf{d}t}(\gamma m_e \dot{z}) = eE_z \Longrightarrow \gamma\beta_z = \frac{e}{m_e c}E_z t + \gamma_0\beta_0 \tag{2.27}$$

If we consider the electron to be relativistic, which is often the case right after injection, we get $\beta_z \approx 1$ and (2.27) becomes

$$\dot{\gamma} = \frac{eE_z}{m_e c} \tag{2.28}$$

If we take (2.28) and insert it into the equation for radial motion (2.22), we get the equation for radial oscillations of an accelerating electron

$$\left(\frac{eE_z}{m_e c}t + \gamma_0\beta_0\right)\ddot{r} + \left(\frac{eE_z}{m_e c}\right)\dot{r} + \left(\frac{\omega_p^2}{2}\right)r = 0 \tag{2.29}$$

We can solve this equation numerically, as shown in figure 2.4. We can see that as the electron accelerates, it gains energy linearly according to (2.28). The increase of relativistic mass diminishes the amplitude of oscillations, but also increases the wavelength. This makes accelerating relativistic electrons an ideal radiator due to their diminishing source size. We can also estimate the dependency of the energy of radiated photons on the electron energy, since at the beginning of this chapter we've shown $\omega \approx 2\gamma^2\omega_e$. Since the electrons oscillate at the betatron frequency ω_β in the relativistic limit, the photon frequency becomes $\omega \approx 2\gamma^2\omega_\beta = \sqrt{2}\gamma^{3/2}\omega_p$. This tells us that higher energy electrons conducting betatron oscillations radiate much higher energy radiation.

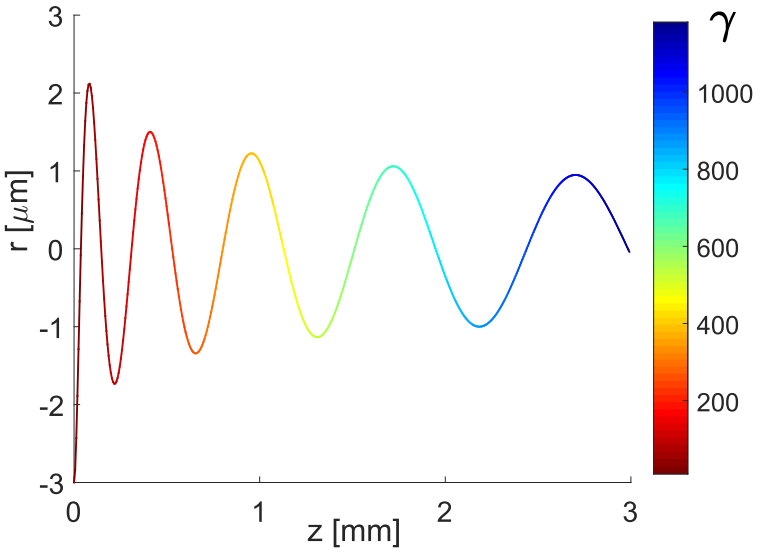

Figure 2.4: Solution of (2.29). We've chosen parameters typically achieved in experiments, $E_z = 200$ GV/m, $n_0 = 2 \cdot 10^{18}$ cm^{-3}. We've considered an electron injected with $\gamma_0 = 10$, $\beta_0 \doteq 1$, $\dot{r}(0) = 0$, $r(0) = r_\beta = -2.5$ μm.

We've mentioned that the ultra-relativistic small amplitude limit produces a second harmonic oscillation in the longitudal direction identical to motion in 1.1.1. This longitudal oscillation necessarily generates radiation of a moving charge in transverse direction, which generates a second harmonic component in the observed radiated spectrum. Such motion corresponds to motion of electrons in inserted devices which produces synchrotron radiation [23]. However, during the injection of the electron and it's acceleration, there are various trajectories and radiating regimes the electron can undertake. We can quantitatively analyze the different radiation regimes by defining the deflection parameter $K = \Omega/\theta$, which is the ratio of the maximum angle between the electron velocity and the axis of propagation Ω, and the opening angle of the radiation cone $\theta \sim 1/\gamma$. The deflection parameter separates the wiggler and the undulator radiation regimes, as shown in figure 2.5.

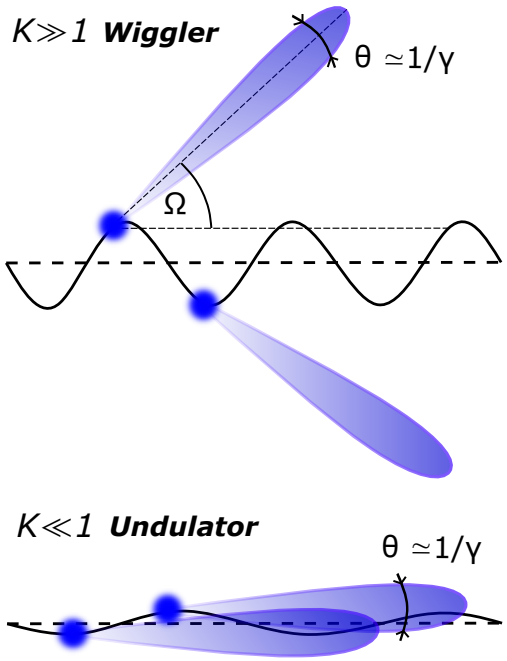

Figure 2.5: Illustration of the wiggler and undulator radiation regimes as separated by the deflection parameter K.

The deflection parameter is also defined for various insertion devices like bending magnets, undulators and wigglers, which are used in synchrotrons [59]. For betatron radiation, the deflection parameter K can be easily obtained. First, let's find the maximum angle Ω by comparing the longitudal and tangential velocity of a relativistic electron $\beta_z \approx 1$

$$\tan\vartheta = \frac{\beta_r}{\beta_z} \approx \beta_r = r_\beta k_\beta \cos\omega_\beta t \tag{2.30}$$

where $k_\beta = \omega_\beta/c$ is the betatron wavenumber. Thanks to the fact that betatron oscillations are usually $r_\beta \sim \mu m$ and the wavenumber is $k_\beta = 2\pi/\lambda_\beta \sim mm^{-1}$, small-angle approximation $\tan\theta \doteq \theta$ is valid and we get the maximum angle as $\Omega = r_\beta k_\beta$. Since the opening angle of the radiation cone is $\theta \simeq 1/\gamma$, we

see that the deflection parameter is the betatron strength parameter mentioned previously

$$\boxed{K = \frac{\Omega}{\theta} = \gamma r_\beta k_\beta = 1.33 \cdot 10^{-10} \sqrt{\gamma n_e [\mathrm{cm}^{-3}]} r_\beta [\mu\mathrm{m}]} \tag{2.31}$$

This equation tells us what kind of radiaton regime can we generally expect for given experimental and electron parameters. As we've previously mentioned, the injected electrons undertake various trajectories and the radiating regime can change even throughout their propagation. The observed radiation spectrum is then often a sum of both the wiggler and the undulator regimes, it is therefore necesary to describe characteristics of both.

Wiggler regime

For $K \gg 1$, the radiation by the electron is emitted within the maximum opening angle $\Omega = K\theta = K/\gamma$. In most cases, this also has the consequence that over the whole trajectory of the radiating particle, the radiation is not constructively interfering. Due to the numerator in radiation integral (2.18), most radiation will be emitted at the turning points, where the electron accelerates the most. The "searchlight beam" flashes emitted at these turning points do not interfere constructively. This allows us to treat the radiation emitted similarly to a charged particle undergoing at any instantaneous moment circular motion along some radius of curvature ρ. Such radiation emitted along the curved turning points is at any instantaneous moment described by (2.18). Following [28], radiation emitted along curvature can be computed analytically as

$$\frac{\mathbf{d}^2 W}{\mathbf{d}\Omega \mathbf{d}\omega} = \frac{e^2}{16\pi^2 \epsilon_0 c} \left(\frac{2\omega\rho}{3c}\right)^2 \left(\frac{1}{\gamma^2} + \theta^2\right)^2 \left[K_{2/3}^2(\xi) + \frac{\theta^2}{1/\gamma^2 + \theta^2} K_{1/3}^2(\xi)\right] \tag{2.32}$$

where ρ is the local radius of curvature, θ is the off-axis angle and $K_{2/3}$, $K_{1/3}$ are the modified Bessel functions of the second kind. The argument ξ is

$$\xi = \frac{\omega\rho}{3c} \left(\frac{1}{\gamma^2} + \theta^2\right)^{3/2} \tag{2.33}$$

Radiation distribution (2.32) tells us that the radiation becomes negligible for $\xi \gg 1$ due to the behaviour of the modified Bessel functions. Critical frequency is defined on-axis $\theta = 0$ for $\xi = 1/2$, which follows from (2.23) as

$$\omega_c = \frac{3c}{2\rho} \gamma^3 \tag{2.34}$$

The critical frequency is the typical frequency up to which most radiation is emitted. In Appendix A.6, it is derived for a wiggler as

$$\boxed{\omega_c = \frac{3}{2} K \gamma^2 \omega_\beta} \tag{2.35}$$

The calculation of (2.23) from the radiation integral shows that the radiated field is composed of two independent polarization components perpendicular to the radiation propagation direction $\boldsymbol{n}$. The parallel polarization is within the orbital plane and the perpendicular polarization is perpendicular to parallel polarization. The terms in (2.23) can be accordingly re-written as

$$\frac{\mathbf{d}^2 W}{\mathbf{d}\Omega \mathbf{d}\omega} = \frac{\mathbf{d}^2 W_{\parallel}}{\mathbf{d}\Omega \mathbf{d}\omega} + \frac{\mathbf{d}^2 W_{\perp}}{\mathbf{d}\Omega \mathbf{d}\omega} \tag{2.36}$$

these distributions are plotted in figure 2.6. As the figure shows, the generated radiation is linearly polarized in the orbital plane $\theta = 0$. For $\theta \neq 0$, the radiation is generally eliptical. We also note that, as previously mentioned, most radiation is emitted within a radiation cone with opening angle $\theta \sim 1/\gamma$. The total radiation distribution (2.32) without any polarization distinction is plotted in figure 2.7.

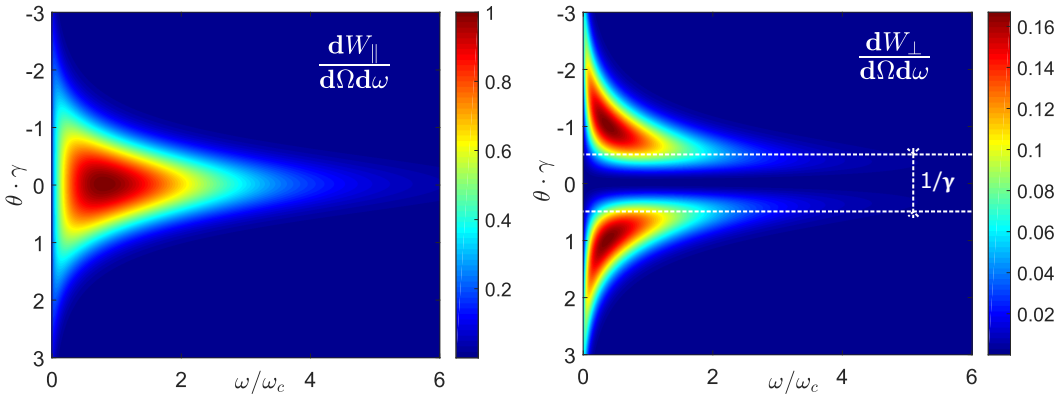

Figure 2.6: Radiation distribution for parallel polarization (left) and perpendicular polarization (right). In normalized units.

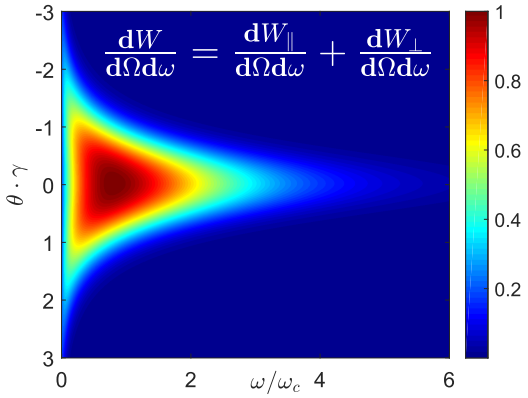

Figure 2.7: Radiation distribution (2.32). In normalized units.

If we're only interested in the spectral content of emitted radiation, we can integrate (2.32) over all angles and obtain the radiation spectrum [28]

$$\frac{\mathbf{d}W}{\mathbf{d}\omega} = \gamma \frac{\sqrt{3}e^2}{4\pi\epsilon_0 c}\left(\frac{\omega}{\omega_c}\right)\int_{\omega/\omega_c}^{\infty} K_{5/3}(x)\mathbf{d}x \tag{2.37}$$

this clearly shows the meaning of critical frequency. Half of total energy emitted by the charged particle is at frequencies below ω_c and half is above ω_c, since it can be numerically verified that

$$\int_0^{\omega_c} \frac{\mathbf{d}W}{\mathbf{d}\omega} = \int_{\omega_c}^{\infty} \frac{\mathbf{d}W}{\mathbf{d}\omega} \tag{2.38}$$

The spectral distribution (2.37) plotted in figure 2.8 gives us evidence to believe that, indeed, we can expect synchrotron-like betatron radiation within the wiggler regime, as was experimentally observed in [23], [24], [25], [26].

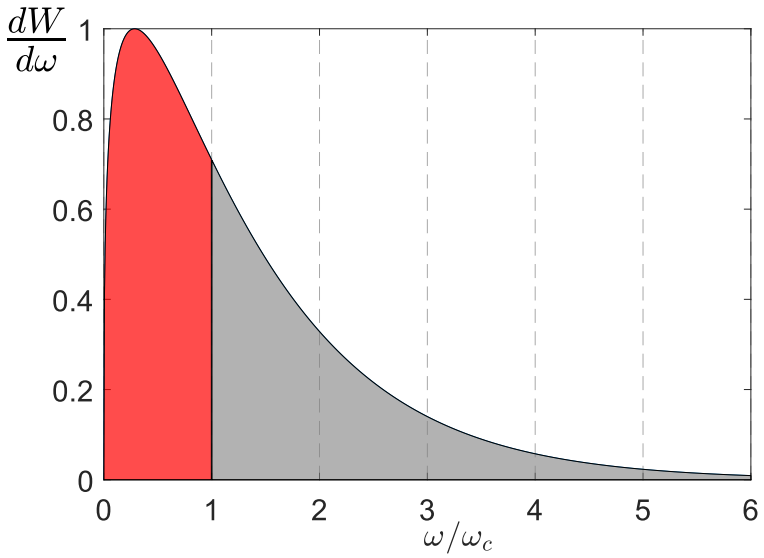

Figure 2.8: Betatron radiation spectrum in the wiggler regime (2.37). In normalized units. Red area is equal to grey area.

Undulator regime

While it is often the case that experimental parameters are set such that wiggler regime is dominant, mostly due to the use of high-powered lasers, there is also the possibility of reaching the undulator regime $K \ll 1$. Interference from overlapping radiation cones emitted during electron's trajectory, as shown on Fig. 2.5, then has to be taken into consideration. We can derive a very important characteristic of undulator radiation by simply considering the effects of constructive interference of radiation emitted at various points.

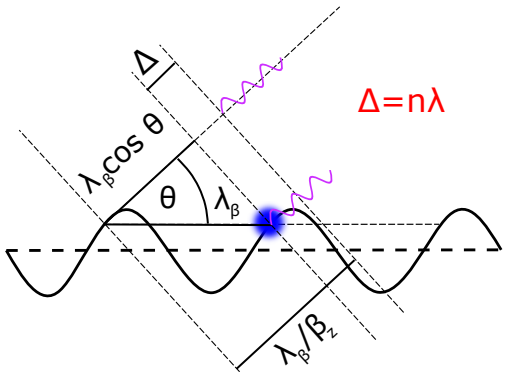

Figure 2.9: Schematic useful for derivation of undulator equation.

From figure 2.9, we see that after oscillating electron traverses one betatron wavelength λ_β, radiation will interfere constructively if the path difference between the respective wavefronts is equal to integer multiple of their wavelength $\Delta = n\lambda$. The electron traverses one wavelength λ_β after time $\lambda_\beta/\langle v_z\rangle$. Therefore, the first emitted wave traverses, during the same time, the length $c\lambda_\beta/\langle v_z\rangle = \lambda_\beta/\langle\beta_z\rangle$. The first wave therefore overtakes the second wave by the path difference between their wavefronts, which for them to interfere constructively must equal

$$\Delta = \lambda_\beta \cos\theta - \frac{\lambda_\beta}{\langle\beta_z\rangle} = \lambda_\beta \cos\theta - \frac{\lambda_\beta}{\langle\beta_z\rangle} = n\lambda \tag{2.39}$$

from (2.30) and (2.31), we know that $\beta_r = (K/\gamma)\cos(\omega_\beta t)$. We can use this to find the averaged longitudal normalized velocity $\langle\beta_z\rangle$, since

$$\beta_z = \sqrt{1 - \frac{1}{\gamma^2} - \left(\frac{K}{\gamma}\right)^2 \cos^2(\omega_\beta t)} \approx 1 - \frac{1 + K^2/2}{2\gamma^2} - \frac{K^2}{4\gamma^2}\cos(2\omega_\beta t) \tag{2.40}$$

averaging over time makes the last term zero. After plugging back to (2.39) with small-angle approximation $\cos\theta \approx 1 - \theta^2/2$ valid for the undulator regime, we get after some algebraic manipulation the famous *undulator equation* [59]

$$\boxed{\lambda_n = \frac{\lambda_\beta}{2\gamma^2 n}\left(1 + \frac{K^2}{2} + \theta^2\gamma^2\right)} \tag{2.41}$$

where n is a natural number and λ_β is the betatron wavelength. This equation describes the harmonic spectrum characteristic for the undulator regime and gives quantitative estimates for wavelengths emitted due to the interference effects.

Calculating the angularly resolved spectral radiation distribution through the radiation integral (2.18) is possible and it was first done by D. F. Alferov in 1974 [61], however due to the sheer cardinality of the result, we will not force the kind reader to read through it and instead refer to mentioned original paper. We however must mention a general result that odd harmonics $n = 1, 3, ...$ described by (2.41) are emitted on-axis and even harmonics $n = 2, 4, ...$ are emitted off axis. We will now instead only present the on-axis $\theta = 0$ spectrum and show how it relates to the wiggler regime. The on-axis radiation spectrum is [28]

$$\left.\frac{\mathbf{d}^2W}{\mathbf{d}\Omega\mathbf{d}\omega}\right|_{\theta=0} = \frac{e^2\gamma^2N^2}{4\pi\epsilon_0 c}\sum_{n=1}^{\infty}\frac{\sin^2[\pi N(\omega/\omega_1 - n)]}{[\pi N(\omega/\omega_1 - n)]^2}\frac{(\omega/\omega_1)K^2}{(1+K^2/2)^2}\left[J_{\frac{n-1}{2}}(Z) - J_{\frac{n+1}{2}}(Z)\right]^2 \tag{2.42}$$

where K is the betatron strength parameter (2.31), N is the number of oscillation periods, $n = 1, 3, ...$ is the odd harmonic number, ω_1 is the fundamental frequency and J_m is the Bessel functions of the first kind. The argument Z is

$$Z = \frac{(\omega/\omega_1)K^2}{4(1+K^2/2)} \tag{2.43}$$

from the undulator equation (2.41) the fundamental frequency ω_1 also follows as

$$\omega_n = 2\gamma^2\omega_\beta\frac{n}{1+K^2/2} \approx 2\gamma^2\omega_\beta n \rightarrow \omega_1 = 2\gamma^2\omega_\beta \tag{2.44}$$

which validates our estimates for frequencies emitted by radiating relativistic charges in (2.1). On-axis radiation distribution for various regimes is showcased in figure 2.10. We see that within the undulator regime, spectrum is pure and only the fundamental harmonic is being emitted. The spectral width can be directly deduced from (2.42) as $\Delta\omega/\omega_1 = 1/N$. This tells us that with more oscillations, we can obtain very narrow spectral lines. Increasing the number of oscillations enough within this regime could possibly even lead to free electron lasing. With increasing strength parameter K, more harmonic frequencies are being present due to the diminishing interference effects and eventually, wiggler regime is reached and the spectrum approaches the continuous synchrotron spectrum (2.32) evaluated for $\theta = 0$. We also note that this transition introduces radiation emitted at dramatically higher energies. This transition can also be explained analytically, as it has been shown in [28] that for $K \gg 1$, (2.42) approaches the on-axis value of (2.32)

$$\left.\frac{\mathbf{d}^2W}{\mathbf{d}\Omega\mathbf{d}\omega}\right|_{\theta=0,K\gg1} \approx \frac{e^2}{16\pi^2\epsilon_0 c}\gamma^2\left(\frac{\omega}{\omega_c}\right)^2 K_{2/3}^2\left(\frac{\omega}{\omega_c}\right) \tag{2.45}$$

where the critical frequency ω_c is (2.35).

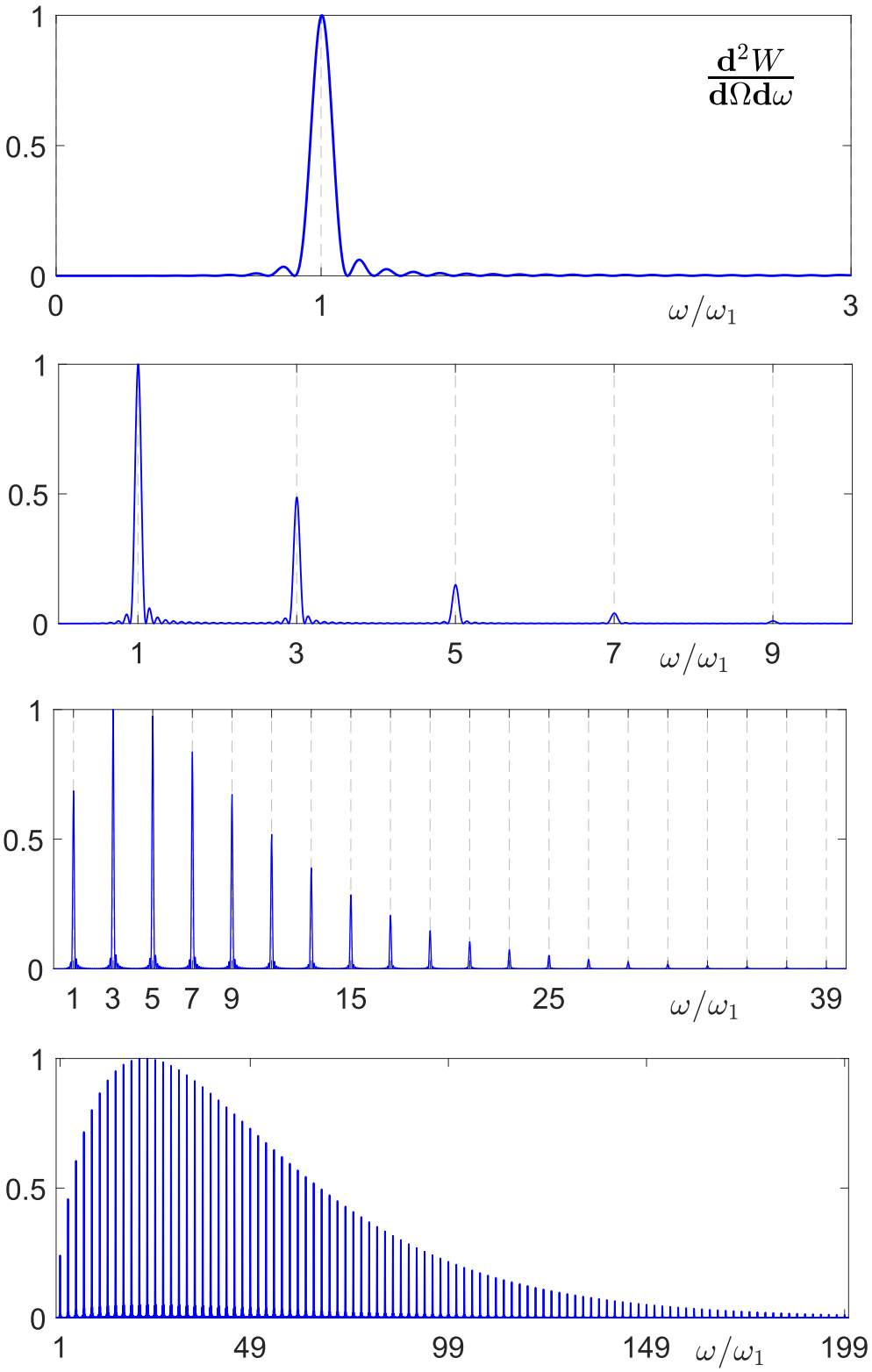

Figure 2.10: Radiation spectrum (2.42). Here we've shown the transition from the undulator to the wiggler regime with increasing deflection parameter K. Number of oscillations was selected as N = 10. From top to bottom K = 0.2, 1, 2, 4

3. Numerical Methods and Results

In this chapter, I will describe numerical methods modeling physical processes in plasma as described by the Maxwell-Vlasov equations (1.68) and calculating radiation emitted by interacting particles through (2.17). This will be done mostly thanks to the Particle-in-Cell (PIC) method, for which many codes are availible. The PIC method will be described in the first section. In the second section, I will proceed to describe the radiation calculation procedure which was initially developed in [62]. My work included developing a particle tracking algorithm generating particle trajectories from PIC code data outputs and upgrading the original code in [62] to fully handle even complicated trajectories from large PIC code data outputs. In the last section, I present my numerical results simulating plasma processes and radiation generation utilizing both of these methods.

3.1 Particle-in-Cell Method

The PIC method represents one of the most powerful and popular algorithms simulating collisionless plasma on the kinetic scale [63], [64], [65]. The PIC method utilizes computational *macro-particles* with finite size within the phase space that represent a number of real particles. These macro-particles discretize the distribution function in (1.68) for each particle species present in the system. The distribution function f_s for species s is given as the sum of distribution functions of macro-particles $f_{s,i}(\boldsymbol{r}, \boldsymbol{v}, t)$. Therefore distribution function of species s with N_s macroparticles is

$$f_s(\boldsymbol{r}, \boldsymbol{v}, t) = \sum_{i=1}^{N_s} f_{s,i} = \sum_{i=1}^{N_s} w_i S_r(\boldsymbol{r} - \boldsymbol{r}_i(t)) S_v(\boldsymbol{v} - \boldsymbol{v}_i(t)) \tag{3.1}$$

where w_i is the particle's weight, which represents the number of real particles the macro-particle i represents and often reaches values above 10^9. S_r and S_v are the *shape functions*, which determine the macro-particle's size within the phase space. The introduction of macro-particles instead of real physical particles dramatically improves the computation time for large-scale simulations, but it also allows us to probe the dynamics of real particles, since the macro-particles representing some number of real particles obey the same dynamics. This is indeed true, because the Lorentz force depends only on the particle's charge to mass ratio q/m, which for macro-particles is the same as for any number of real particles they represent. The shape functions are usually chosen to reduce the computational costs at desired physical resolution. The velocity phase function is often simply a delta function $S_v = \delta(\boldsymbol{v} - \boldsymbol{v}_i(t))$, while the spatial shape function is chosen usually as b-spline basis of order n. With higher order n, numerical stability, accuracy and computational costs are increased [64].

Substituting (3.1) into the first Vlasov equation in (1.68), multiplying by v and integrating over velocity and position respectivelly results in equations of motion for the macro-particles

$$\begin{aligned} \frac{\mathrm{d}\boldsymbol{x}_i}{\mathrm{d}t} &= \frac{\boldsymbol{u}_i}{\gamma_i} \\ \frac{\mathrm{d}\boldsymbol{u}_i}{\mathrm{d}t} &= \frac{q_s}{m_s}\left(\boldsymbol{E}_i + \frac{\boldsymbol{u}_i}{\gamma_i} \times \boldsymbol{B}_i\right) \end{aligned} \tag{3.2}$$

where $\boldsymbol{u}_i = \gamma_i \boldsymbol{v}_i$, $\gamma_i = \sqrt{1 + \boldsymbol{u}_i^2/c^2}$ is the gamma factor for the macro-particle and $\boldsymbol{E}_i$ and $\boldsymbol{B}_i$ are the electric and magnetic fields acting on the macro-particle. While equations (3.2) track macro-particles in the continuous phase-space, we also need to calculate how the fields change due to macro-particle dynamics. This requires solving the Maxwell equations, which are often solved through discretization of spatial coordinates to an equidistant spatial grid $\boldsymbol{r} \to \boldsymbol{r}_{ijk}$. Numerical solution of Maxwell equations also requires discretization of time to equidistant timesteps $t \to t_n$. We note here that the PIC method therefore combines Eulerian frame of reference for fields and Lagrangian frame of reference for particles.

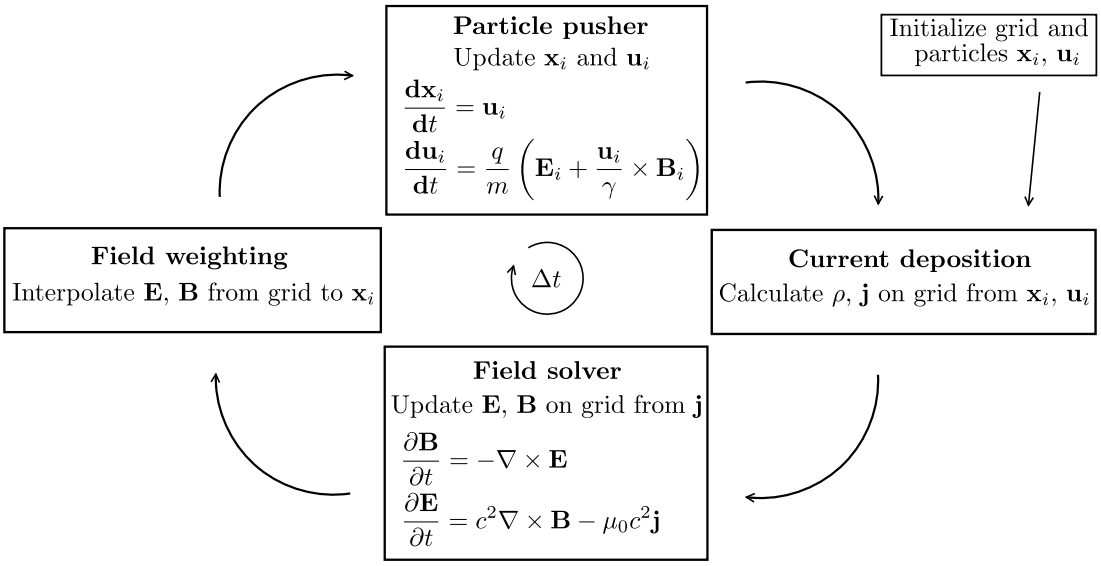

Figure 3.1: Computational PIC loop.

The PIC computational cycle in figure 3.1 illustrates how the PIC method works. It is not within the scope of this thesis to fully describe the algorithms involved within each step, so we will instead briefly describe each one of them and for details refer the kind reader to the availible literature [65], [64]. The computation begins with **grid initialization**, where we generate an equidistant rectangular grid $\boldsymbol{r}_{ijk} = (i\Delta x, j\Delta y, k\Delta z)$, we also discretize time as $t_n = (n\Delta t)$. Positions of macro-particles in phase-space are usually initialized randomly based on particle distribution function $f_s(\boldsymbol{r}, \boldsymbol{v}, t = 0)$, which is provided by the user.

Current deposition refers to the calculation of charge and current on grid points from macro-particle positions and velocities in the continuous phase-space. By substituting the macro-particle distribution function into (1.69), we get for given species s

$$\begin{aligned} \rho_s &= \sum_p^{N_s} q_s \int f_{s,p}(\boldsymbol{r}, \boldsymbol{v}, t) \mathbf{d}^3 v = \sum_p^{N_s} q_s w_p S_r(\boldsymbol{r}_{ijk} - \boldsymbol{r}_p(t_n)) \\ \boldsymbol{j}_s &= \sum_p^{N_s} q_s \int \boldsymbol{v} f_{s,p}(\boldsymbol{r}, \boldsymbol{v}, t) \mathbf{d}^3 v = \sum_p^{N_s} q_s w_p \boldsymbol{v}_p(t_n) S_r(\boldsymbol{r}_{ijk} - \boldsymbol{r}_p(t_n)) \end{aligned} \tag{3.3}$$

In addition to this calculation, current deposition also contains the evaluation of the continuity equation. If it is not satisfied, there will be errors in the Gauss' law and it is necessary to calculate charge correction from the Poisson equation and add it to (3.3). These discrete charge error correcting techniques are known as charge conservation methods [65], [66].

Field solver usually refers to the numerical method that solves Maxwell's equations, which is most commonly the *finite-difference time-domain method* (FDTD). This method utilizes *Yee's scheme*, which applies centered finite difference operators on staggered grids in space and time. This scheme has been throughout time shown to be extremely robust and numerically stable [67]. It staggers vector field components from the point (i, j, k) around a cartesian cell centered at $(i+1/2, j+1/2, k+1/2)$, as shown in figure 3.2. Current components are co-located with the electric field components and the charge is assigned at the middle of the cell $(i + 1/2, j + 1/2, k + 1/2)$. Spatial derivatives are assigned according to Yee's scheme and time derivatives according to standard leap-frog scheme [64]. In this method, divergence Maxwell's equations serve as initial conditions that must be satisfied. These equations will be fulfilled with each timestep only if continuity equation is satisfied [65], [66], [67]. This is at each timestep checked during current deposition.

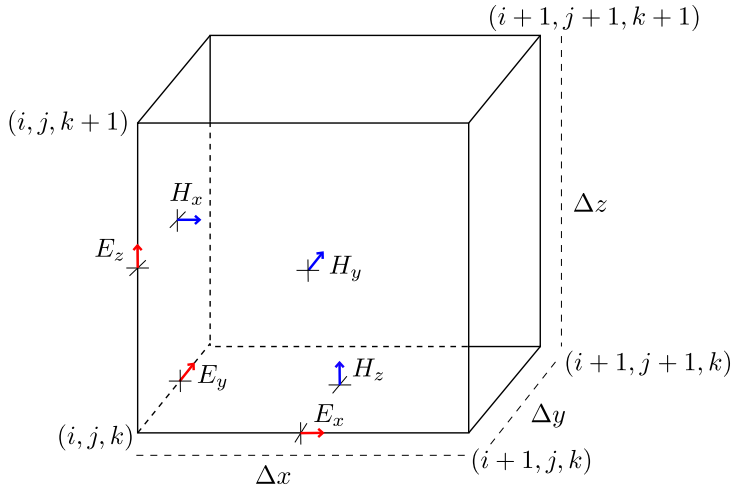

Figure 3.2: Yee's lattice used in standard FDTD. Yee's scheme staggers field components around points in the rectangular grid.

Field weighting refers to the interpolation of the grid values of fields to the spatial components of macro-particles. The interpolation is done simply by taking the spatial averages and utilizing the shape functions

$$\begin{aligned} \boldsymbol{E}_p(t_n) &= \sum_{ijk} \boldsymbol{E}(\boldsymbol{r}_{ijk}, t_n) S_r(\boldsymbol{r}_{ijk} - \boldsymbol{r}_p(t_n)) \\ \boldsymbol{B}_p(t_n) &= \sum_{ijk} \boldsymbol{B}(\boldsymbol{r}_{ijk}, t_n) S_r(\boldsymbol{r}_{ijk} - \boldsymbol{r}_p(t_n)) \end{aligned} \tag{3.4}$$

Particle pusher involves solving the equations of motion (3.2) at each time step. This can be done in multiple ways, the easiest of which is the *leap-frog algorithm* [64]. However, due to it's excellent stability, *Boris method* is generally used [68].

Numerical stability and physical resolution

Numerical scheme is stable if a numerical error caused in one timestep is not source for the increase of error in the next time step. Due to high stability of previously presented numerical schemes, stability of the PIC simulation depends mainly on the spatial and temporal resolution of the initialized grid. Discretization of continuous space into grid introduces non-physical instabilities, like numerical Cherenkov instability, which is due to the fact that particle dispersion relations $\omega(k)$ on discrete grid are not the same as in continuous space [64]. Small resolution of the spatial grid and low order of the particle shape function may lead to particles travelling faster than gridded fields, generating non-physical Cherenkov radiation. One of the worst numerical instabilities of PIC codes is however the effect of numerical heating, which causes particle temperature in the simulation to grow exponentially until the effective Debye length is similar to the grid cell size. This is due to numerical errors that are obtained from interpolation of gridded fields to particle positions and gridded currents from particle trajectories. Numerical heating can be eliminated with higher resolution or shape function order. This tells us the first condition that must be fulfilled within PIC simulations is

$$\Delta x, \Delta y, \Delta z \leq \lambda_D = \sqrt{\frac{\epsilon_0 k_B T_e}{n_e e^2}} = 7.43 \sqrt{\frac{T_e[\mathrm{eV}]}{n_e[\mathrm{cm}^{-3}]}}\ \mathrm{m} \tag{3.5}$$

where λ_D is the Debye length of quasi-neutral cold plasma at which the electric charge of a particle is effectivelly screened by the plasma. This condition makes it computationally intensive to study high density plasma phenomena within PIC codes. The Courant-Friedrichs-Lewy (CFL) condition assures that particles do not cross more than one cell during each time step [69]

$$\frac{1}{\Delta x^2} + \frac{1}{\Delta y^2} + \frac{1}{\Delta z^2} = \frac{C}{c^2 \Delta t^2} \tag{3.6}$$

The condition is satisfied when the CFL number satisfies $C \leq 1$. Physically, this condition assures that particles cannot propagate faster than light. Lastly, we need to resolve all physical frequencies in the simulation, such as plasma or laser

frequency. Nyquist-Shannon theorem states that frequency ω will be properly resolved if the time step satisfies $\Delta t \leq 2/\omega$ [70].

3.2 Radiation Calculation

In this section, we describe the numerical solution of equation (2.17). Once again, we will only briefly present the main algorithm developed in [62], where details can be found. Once we have obtained the trajectory of a particle in the form $(t, \boldsymbol{r}, \boldsymbol{p})$, we provide it as an input for the main algorithm for each time step $t_n = n\Delta t$. The main algorithm comes in three parts

Radiation Field

At each time step $t_n = n\Delta t$

1. Calculate the distance between the electron and observer $|\boldsymbol{R}(t_n)| = |\boldsymbol{r} - \boldsymbol{x}(t_n)|$.
2. Calculate the observer time $t'_n = t_n - |R(t_n)|/c$.
3. Calculate the Lorentz factor $\gamma(t_n)$ and normalized electron velocity $\boldsymbol{\beta}(t_n)$.
4. Calculate electron acceleration using forward difference method $\dot{\boldsymbol{\beta}}(t_{n+1}) = \frac{\boldsymbol{\beta}(t_{n+1}) - \boldsymbol{\beta}(t_n)}{\Delta t}$
5. Radiation field is evaluated at each time step according to (2.9), where only the second term $\boldsymbol{E}_{rad}$ is taken.

Radiation field part of the algorithm was designed for well resolved trajectories prepared by the user. However, PIC simulations often come in large discrete data dumps reaching ~ 100 GB, where each data dump is separated by a time step of ~ 10 fs. We included a 0th algorithm step that interpolates particle trajectories into smooth trajectories that are then sampled so that acceleration calculated in the 5th step is well resolved. All of this strongly depends on the type of interaction we are simulating. For example, how long does the particle accelerate along the turning points, which can be few fs. For LWFA electrons, this usually means sampling the trajectory with a sampling period $T \sim 0.01$ fs.

Radiation Spectrum

After the field is calculated, we have to apply Fourier transform according to (2.17). The algorithm can be modified to sustain coherence properties of radiation at higher computational cost by first calculating radiation field of each investigated electron and then proceed with this part of the algorithm, however in plasma betatron electrons are mostly incoherent therefore the resulting spectrum coming from an accelerated electron bunch is simply summed up for all electrons. The algorithm for calculation of radiation spectrum follows as

1. Maximum and minimum observer time t'_{min}, t'_{max} is assigned

2. Necessary amount of samples N_τ to satisfy Nyquist-Shannon theorem [70] is found by numerically finding value P, such that

$$N_\tau = 2^P \geq \left| \frac{2\mathcal{E}_{max} \cdot (t'_{max} - t'_{min})}{2\pi(h/2\pi)} \right| \tag{3.7}$$

   $\mathcal{E}_{max}$ is an expected maximum energy in the radiated spectrum, it's overestimation adversely affects performance. Correct estimate depends on correct evaluation of all relevant radiation parameters presented in Chapter 2.

3. Sampled observer time $\tau \in (t'_{max}, t'_{min})$ is created with N_τ equidistant samples

4. Radiation field $\boldsymbol{E}_{rad}$ calculated in the previous step is interpolated and resampled for N_τ samples in observer time τ.

5. Fast Fourier transform is then applied on $\boldsymbol{E}_{rad}(\tau)$ and the spectral intensity of radiation is obtained as

$$\frac{\mathbf{d}^2 W}{\mathbf{d}\Omega \mathbf{d}\omega} = \frac{c\epsilon_0}{\pi} \frac{|\mathcal{F}\left[E_{Rx} R(\tau)\right]|^2 + |\mathcal{F}\left[E_{Ry} R(\tau)\right]|^2 + |\mathcal{F}\left[E_{Rz} R(\tau)\right]|^2}{F_s} \tag{3.8}$$

   where $F_s = 1/(\Delta\tau)$ is the sampling frequency

Angular resolution in (3.8) is achieved by repeating this algorithm for each angle θ, ϕ in a solid angle $|\phi_{max} - \phi_{min}| \times |\theta_{max} - \theta_{min}|$ that is specified along with angle steps $\Delta\theta, \Delta\phi$ in the input file. The angles are used in the position vector of the observer $\boldsymbol{r} = (x, y, z)$ as

$$\begin{aligned} x &= x \\ y &= x \cdot \tan(\phi) \\ z &= x \cdot \tan(\theta) \end{aligned} \tag{3.9}$$

Radiation Algorithm Limitations

The most important things to consider when using this algorithm is the choice of expected maximum energy $\mathcal{E}_{max}$ which specifies the sampling rate F_s and the observed solid angle $|\phi_{max} - \phi_{min}| \times |\theta_{max} - \theta_{min}|$ with angle steps $\Delta\theta, \Delta\phi$. These must be initially selected by the user and incorrect estimate may result in orders of magnitude longer computation time. It is always better to analyze the situation with theory developed in Chapter 2 first and then restrict the parameters as much as possible to test the computational demands. The sampling rate dictated by the Nyquist-Shannon theorem is however necessary condition, otherwise numerical aliasing will be present in the spectrum. This calculation also neglects all QED effects mentioned in Chapter 1 or the electron losing energy due to radiation reaction. It is therefore important to use it only for regimes where these effects can

be neglected. For relativistic electrons, the dominant term in radiation reaction comes from the energy-momentum transferred to the scattered electromagnetic wave [71]. It can be estimated from the radiated power (1.42) that radiation reaction can be neglected when the number of oscillations N the electron conducts along it's trajectory satisfies [71]

$$N \ll N_{RR} = \frac{\lambda_\beta}{2\pi^2 c\tau_0 \gamma K^2} \tag{3.10}$$

where τ_0 is the interaction time scale and γ is the electron gamma factor. For current Betatron radiation experimental parameters, N_{RR} is on the order of 10^7. During LWFA, electrons usually oscillate for $N \sim 10$ with energies ranging up to $\sim$ GeV. Radiation reaction can be therefore neglected for Betatron radiation.

3.3 Results

Test simulation

To showcase that the PIC method is able to reproduce the plasma physics involved in LWFA, we've prepared a 2D simulation within the fully parallel EPOCH code with initial parameters corresponding to the non-linear relativistic regime $a_0 > 1$, for which we've presented one-dimensional analytic results in figure 1.6. The initial laser parameters were selected as $a_0 = 2.3$, $\lambda_L = 0.808$ μm, $\tau_{(1/e)} = 25$ fs, $w_0 = 5.5$ μm. The laser is in all following simulations described in paraxial approximation as a gaussian beam with gaussian temporal envelope. The gas target was prepared as a homogeneous underdense pre-ionized helium gas, which is not at all a rough approximation, since helium becomes completely ionized through barrier suppresed ionization at values above $a_0 = 0.065$ [72]. This means that within the non-linear regime, laser strength is large enough to allow for complete helium gas ionization by the laser pulse front edge. Initial plasma density was set as $n_0 = 5 \cdot 10^{18}$ cm^{-3} with temperature corresponding to $k_B T =$ 100 eV. The laser was focused at the plasma entrance. The resolution of the grid was selected to satisfy (3.5), (3.6) and resolve plasma and laser wavelengths. The number of macro-particles per cell was set as $N_{ppc} = 3$.

Results of the simulation are presented in figures 3.3, 3.4 and 3.5. In Fig. 3.3 (a), we see that at simulation time t = 90 fs, the laser is entering the plasma. At t = 170 fs (b), the laser has entered the plasma and begins to push away electrons through the ponderomotive force. 100 microns into the gas, at t = 550 fs (c), the electrons start forming the plasma wakefield due to the lower potential behind the driving laser pulse. We also notice that the plasma response is not linear and sharp density crests are alredy forming and that the laser strength a_0 has increased due to self-focusing. At t = 980 fs (d), the plasma wakefield corresponding to the bubble regime is estabilished and laser strength is diminishing due to laser energy depletion into the wakefield. The last frame at t = 4.6 ps (e) shows laser filamentation due to modulation from plasma. As laser intensity drops through pump depletion below the critical threshold for self-focusing, the laser begins diffracting and subsequently the plasma wakefield deteriorates.

In Fig. 3.5, we've plotted at t = 980 fs the longitudal and transverse components of the electric field corresponding respectively to the laser and plasma wave. The accelerating longitudal electric field E_z of the plasma wave is after 200 microns of laser pulse propagation inside the gas target reaching magnitude of 200 GV/m. This test simulation validates previously presented analytic results and extends our understanding of plasma wakefield evolution inside the target within the non-linear regime.

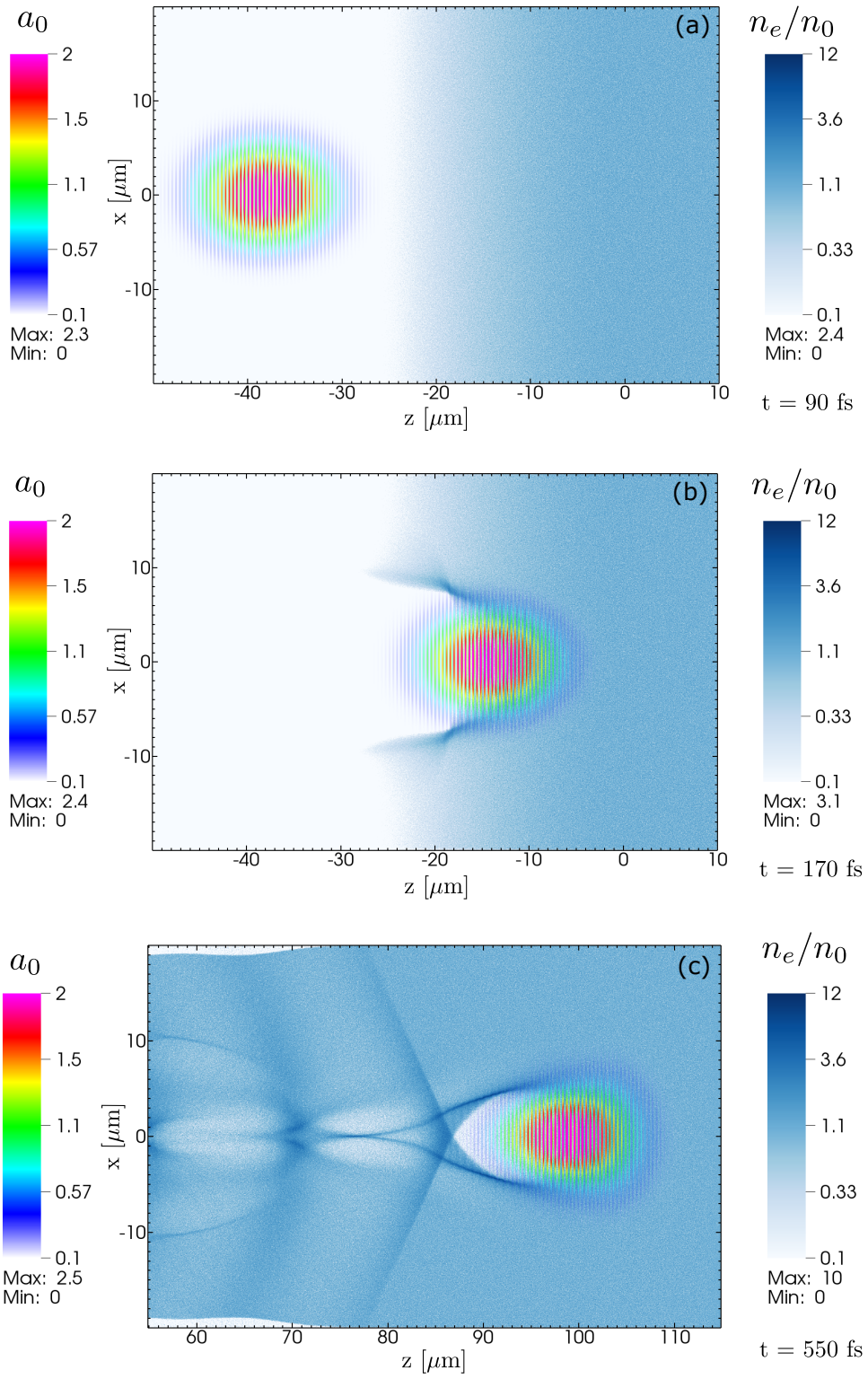

Figure 3.3: PIC simulation results in normalized units. (a) Laser pulse is entering the gas target. (b) Laser pulse has entered the gas target and formation of wakefield through ponderomotive force begins (c) Non-linear wakefield is being estabilished and the plasma response causes the laser pulse to self-focus, increasing peak a_0.

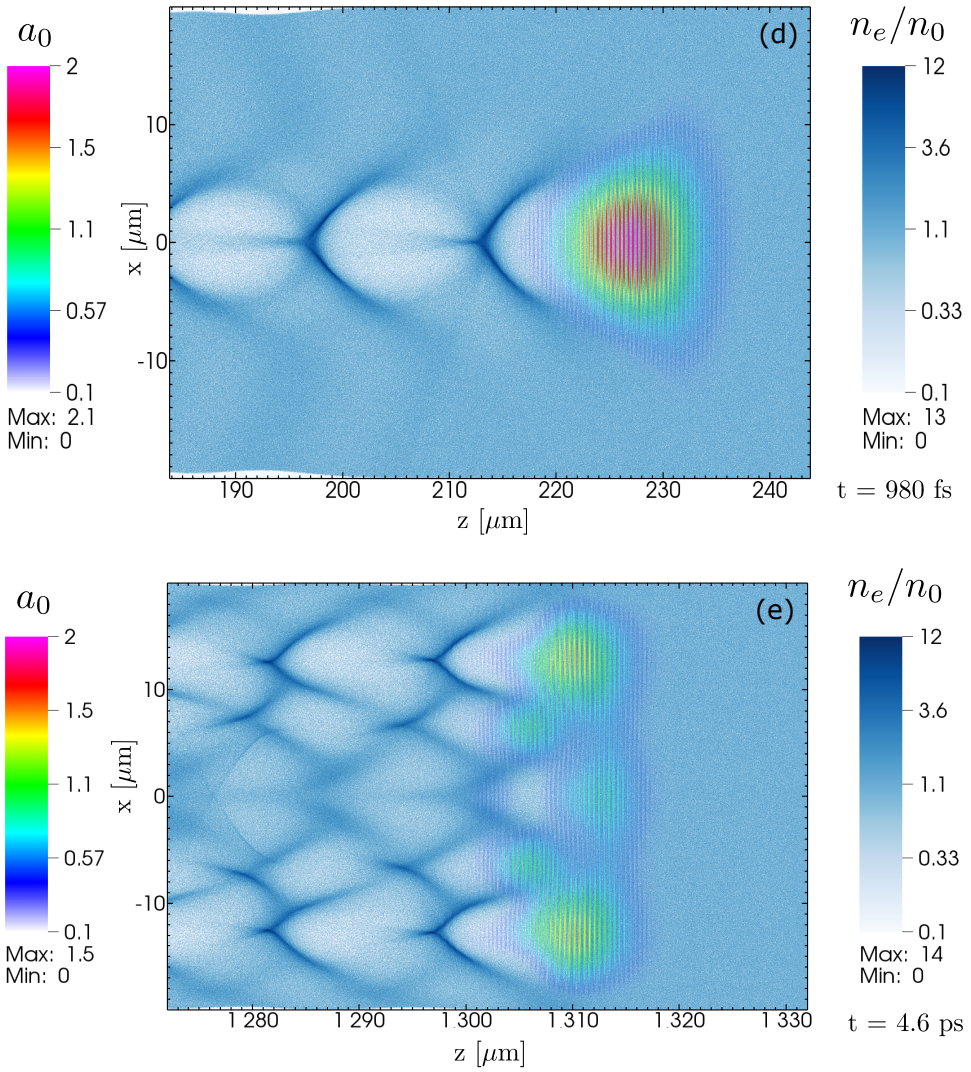

Figure 3.4: PIC simulation results in normalized units. (d) Bubble regime is estabilished. Laser pulse energy is depleted into plasma excitation. Low intensity regions of the pulse begin diffracting, unable to continue self-focusing. (e) Laser pulse is filamented and deteriorating due to low intensity from pulse depletion. Non-linear wakefield has deteriorated and follows filamentation of laser pulse.

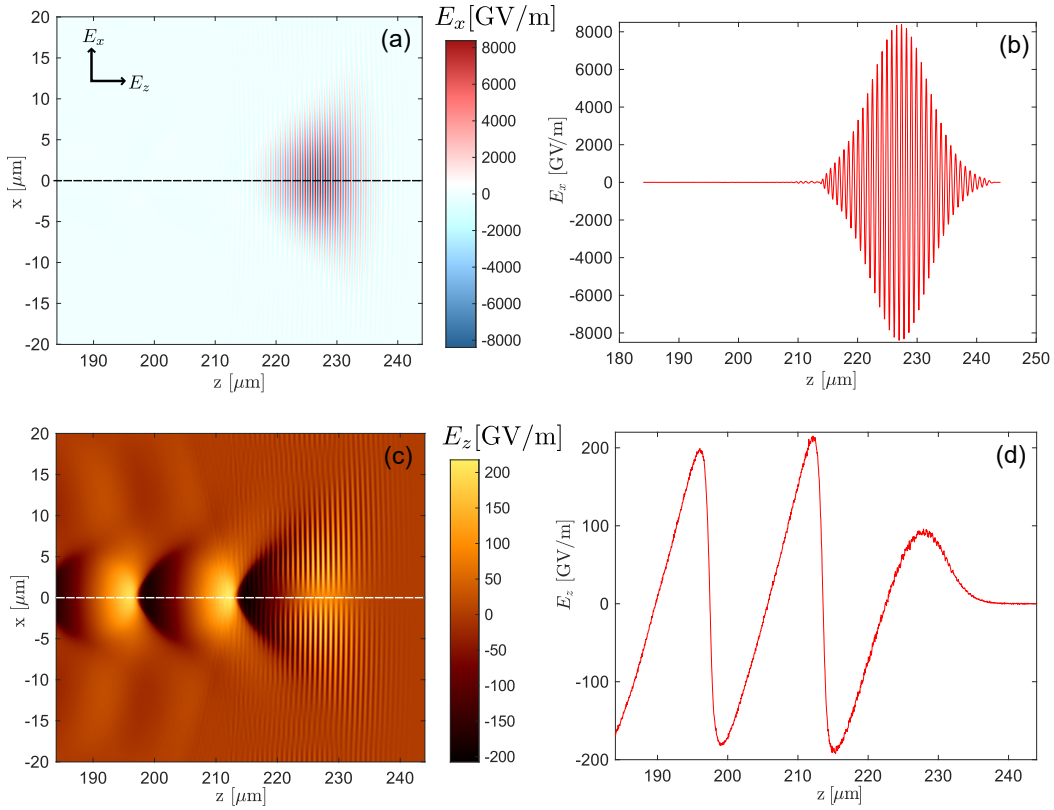

Figure 3.5: Electric intensity at t = 980 fs. (a) Transverse electric intensity E_x corresponding to the laser pulse. (b) E_x at x = 0. (c) Longitudal electric intensity E_z corresponding to the plasma wave. (d) E_z at x = 0.

Gas density scan

Our goal in this thesis is to design and numerically optimize the gas target for Betatron X-ray radiation being generated with state-of-the-art petawatt-class laser systems. In an experimental setting, changing pressure of the gas is often the simplest way to tune both the acceleration of particles and radiation generation. We've therefore set up three 2D PIC simulations with the EPOCH code with various gas densities $n_0 = 3, 5, 10 \cdot 10^{18}$ cm^{-3} and compared the results. The reason for conducting 2D instead of 3D simulations is a practical one. It is well known in literature that 2D PIC simulations only offer a qualitative insight, however 3D simulations typically require two orders of magnitude more computational resources [73]. Purpose of this work is to provide such qualitative estimate for various density cases and benchmark for future study. For the purpose of total charge estimation of the accelerated bunches, we estimated the size of the electron bunch in the missing transverse y direction to be same as in the transverse x direction. This might result in an overestimation of the total charge, which will be checked in future quantitative 3D simulations. For all of these simulations, we've selected the same laser paramaters that were simulated on target for the first stage of operation of the L3 laser system at ELI Beamlines. The focused beam parameters at diffraction limit are $a_0 = 4$, $\lambda_L = 0.808$ μm, $\tau_{(1/e)} = 28$ fs, $w_0 = 14$ μm. The corresponding peak laser intensity is $I_0 \doteq 3.4 \cdot 10^{19}$ W/m^2.

Case I

The results of the PIC simulation with the density set at $n_0 = 3 \cdot 10^{18}$ cm^{-3} is presented in Fig. 3.6 and 3.7. Fig. 3.6 shows snapshots of evolution of the plasma wakefield and the propagating laser. At the beginning of the simulation at t = 90 fs (a), we see that the laser pulse is focused upon the gas target with transverse electric intensity plotted in Fig. 3.7 (a), (b). The wakefield is very well estabilished at t = 10650 fs (b), with the magnitude of electric intensity reaching 700 GV/m as shown in Fig. 3.7 (c), (d). While the accelerating electric intensity is very high, there is negligible number of electrons injected into the wakefield and therefore this low gas density is not suitable for betatron radiation generation from self-injected electrons. It could however serve well in multi-stage targets for subsequent acceleration of injected electrons or in density tailored targets. At t = 16780 fs (c), we show the laser pulse leaving the 5 mm long gas target. It has been modulated by the plasma and positive chirp due to photon acceleration is observed in Fig. 3.7 (e), (f). To save computational resources, we didn't proceed with needless radiation calculation due to negligible injected electron charge ($Q_{total} \sim 1$ pC) into the accelerated wakefield compared to cases with higher density, as will be shown in the following.

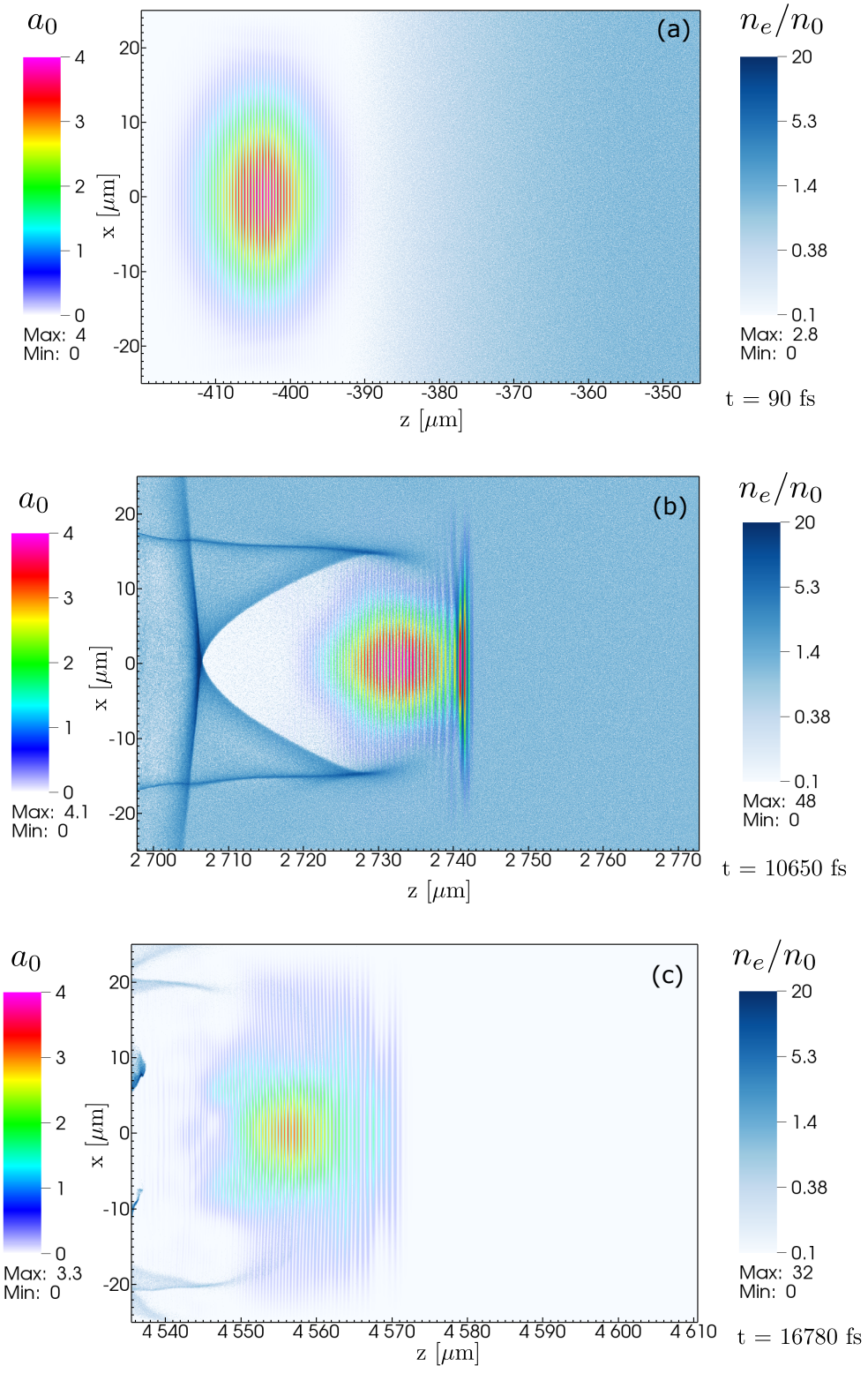

Figure 3.6: PIC simulation results in normalized units. (a) Laser pulse is entering the gas target. (b) Plasma wakefield is estabilished with high accelerating gradient, no electrons are injected. (c) Depleted and positively chirped laser pulse is leaving the gas target.

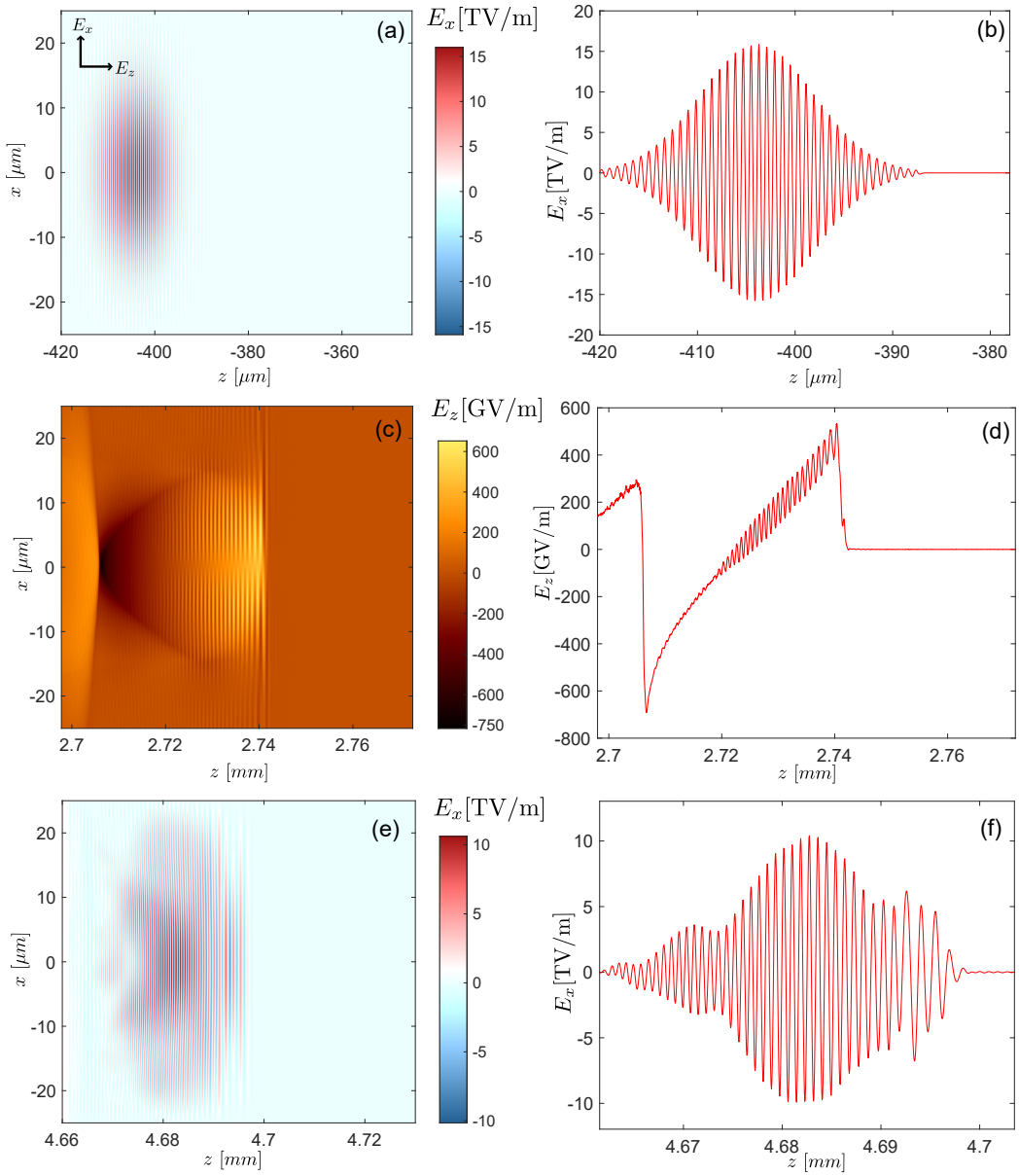

Figure 3.7: (a) Transverse electric intensity E_x corresponding to the laser pulse at t = 90 fs. (b) E_x at x = 0. (c) Longitudal electric intensity E_z corresponding to the plasma wave at t = 10650 fs. (d) E_z at x = 0. (e) Modulated transverse electric intensity E_x at t = 16780 fs. (f) E_x at x = 0.

Case II

Results of PIC simulation of the case $n_0 = 5 \cdot 10^{18}$ cm^{-3} are presented in figures 3.8, 3.9, 3.10, 3.11 and 3.12. In Fig. 3.8, we see the laser enter the gas target (a) and proceed to excite the plasma wakefield through ponderomotive force (b). The excitation in this case is much more violent and immediate compared to the previous case. This is due to higher density and therefore plasma frequency. Higher density also facilitates wavebreaking more easily and injection of electrons freed from the fluid motion of the plasma takes place very soon. At t = 2430 fs (c), we alredy observe electron bunch within the main accelerating phase gaining energy. In Fig. 3.9 at t = 5.26 ps (d), the electron bunch with total charge of 85.9 pC reaches up to $\gamma \approx 700$, the accelerating longitudal field is plotted in Fig. 3.11 (a), (b). At t = 8.51 ps (e), the accelerated bunch reaches maximum energy and starts losing energy due to dephasing. Energy spectrum of the bunch at maximum energy before dephasing at t = 8.51 ps is shown in Fig. 3.11, (d). At the same moment, we can also see a second electron bunch being self-injected through wavebreaking at the back of the bubble and proceeding to rapidly accelerate at t = 9.07 ps (f). Here we've also hidden the laser field to showcase dephasing of the first accelerated electron bunch and also highlight it's oscillatory motion during acceleration. Around t = 12.45 ps, we see that the first bunch has lost enough energy to be scattered from the wakefield by the ponderomotive and coulombic force, while electrons within the second bunch reach up to $\gamma \approx 1500$. The exiting beam divergence is $\theta \approx 15$ mrad.

The accelerating longitudal field is plotted in Fig. 3.11 (e), (f). At t = 14.2 ps (h), around 4.1 mm into the target, closely behind the second bunch we see the injection of a smaller third bunch. The total charge of these two bunches is $Q_{total} \doteq 848$ pC. Before leaving the 5 mm target at t = 16.7 ps (i), we see the accelerated electrons reaching up to $\gamma \approx 2000$. Charge density integrated along x and energy spectrum of the exiting accelerated electrons is shown in Fig. 3.12 (a), (b). In Fig. 3.12 (c), (d), we've also shown the modulated laser pulse on exit showing the energy depletion and positive chirp it suffered throughout it's propagation.

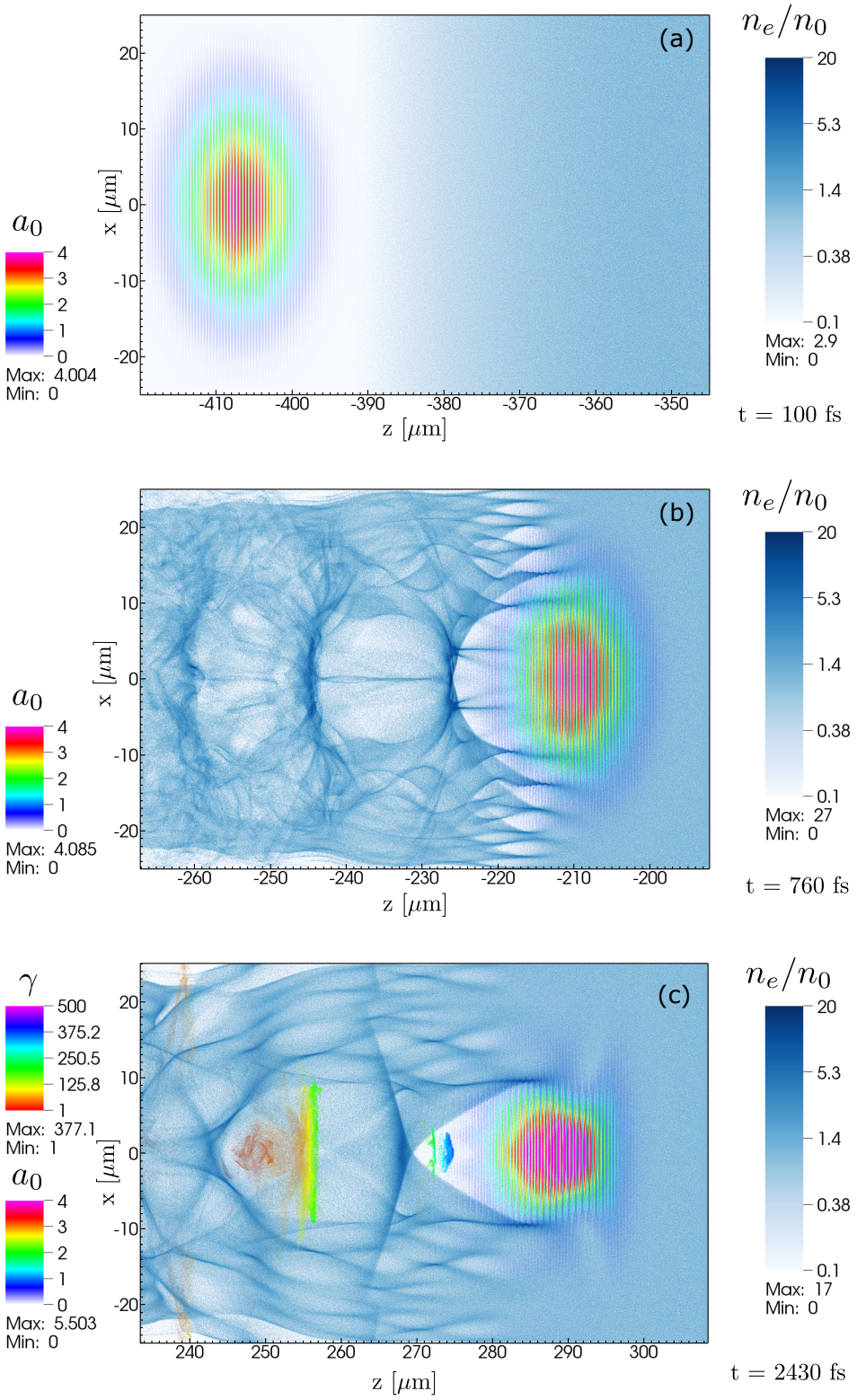

Figure 3.8: PIC simulation results in normalized units. (a) Laser pulse is entering the gas target. (b) High plasma density causes more violent response to the ponderomotive evacuation, wakefield is estabilishing with wavebreaking occuring in highest density crests. (d) Wakefield is estabilished and electrons are trapped within the accelerating phase of the wakefield.

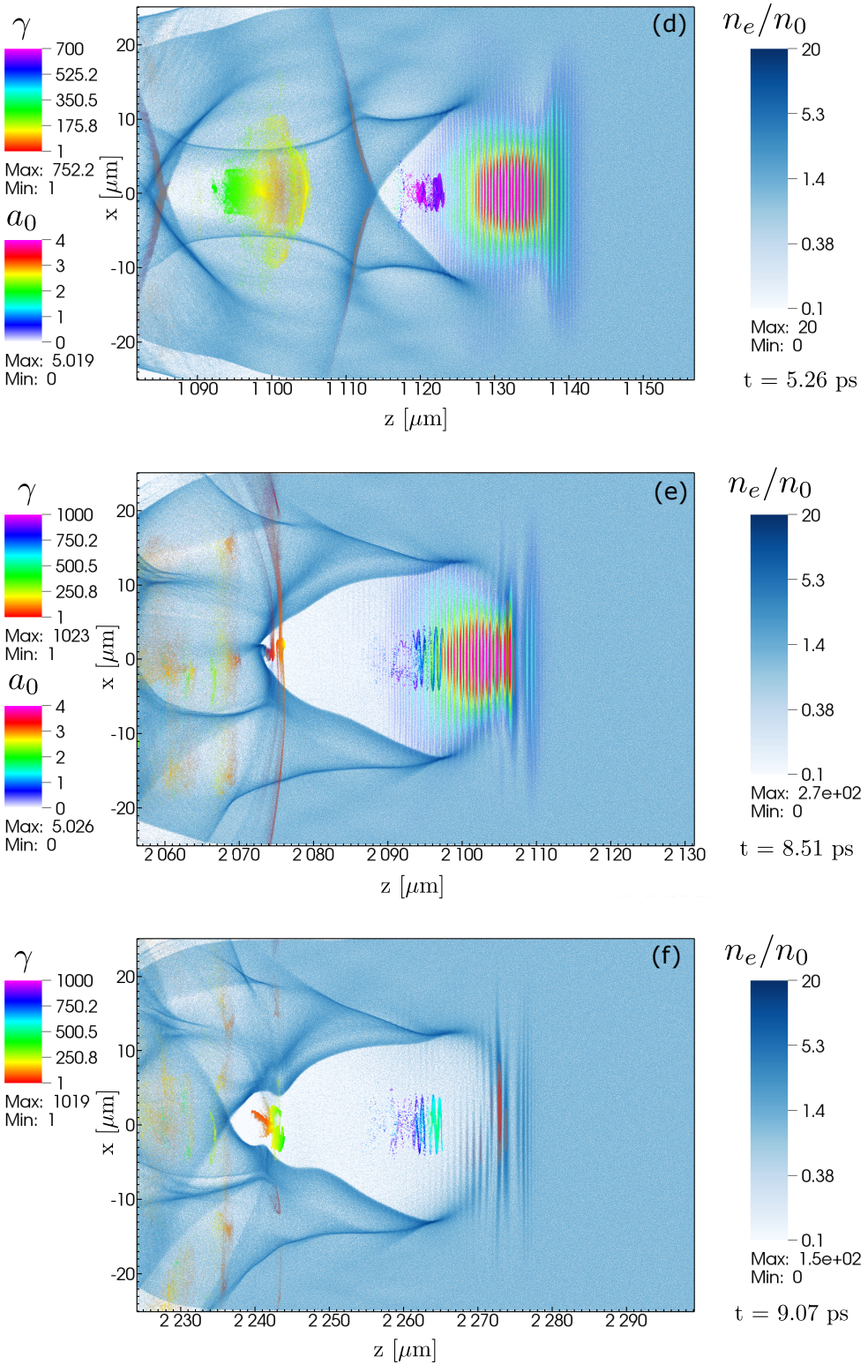

Figure 3.9: PIC simulation results in normalized units. (d) Electrons within the main bubble are reaching $\gamma \approx 750$. (e) Electrons that reached $\gamma \approx 1000$ begin dephasing and losing energy. High charge electron bunch is injected through wavebreaking at the back of the bubble. (f) Electrons from the first bunch are dephasing, electrons from the second bunch are rapidly gaining energy.

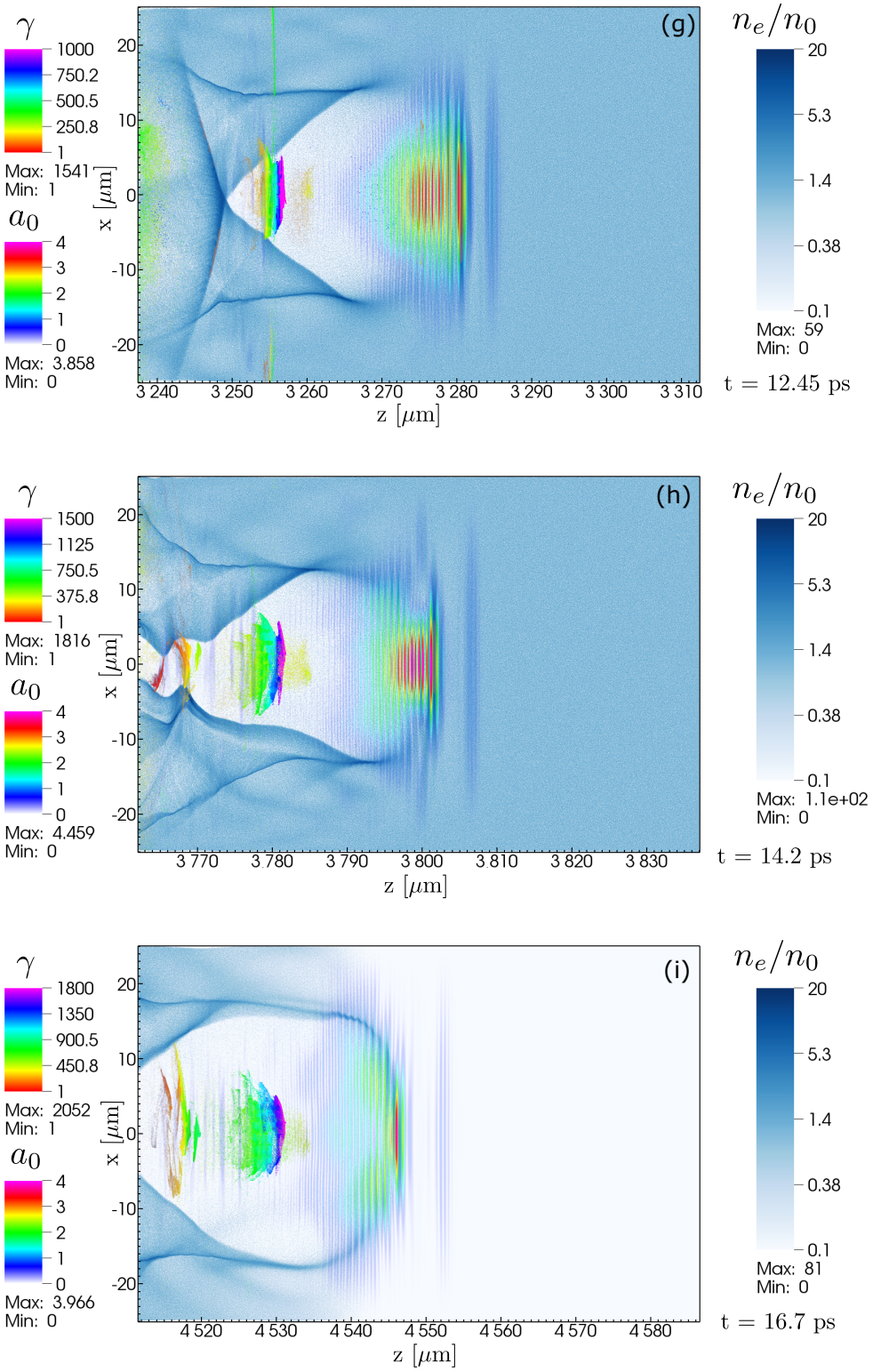

Figure 3.10: PIC simulation results in normalized units. (g) Electrons from the second bunch are quickly reaching high energies. Laser field is depleting. (h) Third electron bunch is injected at the back of the bubble. (i) High charge bunch of electrons reaching $\gamma \approx 2000$ exits the gas target. Laser pulse is depleted.

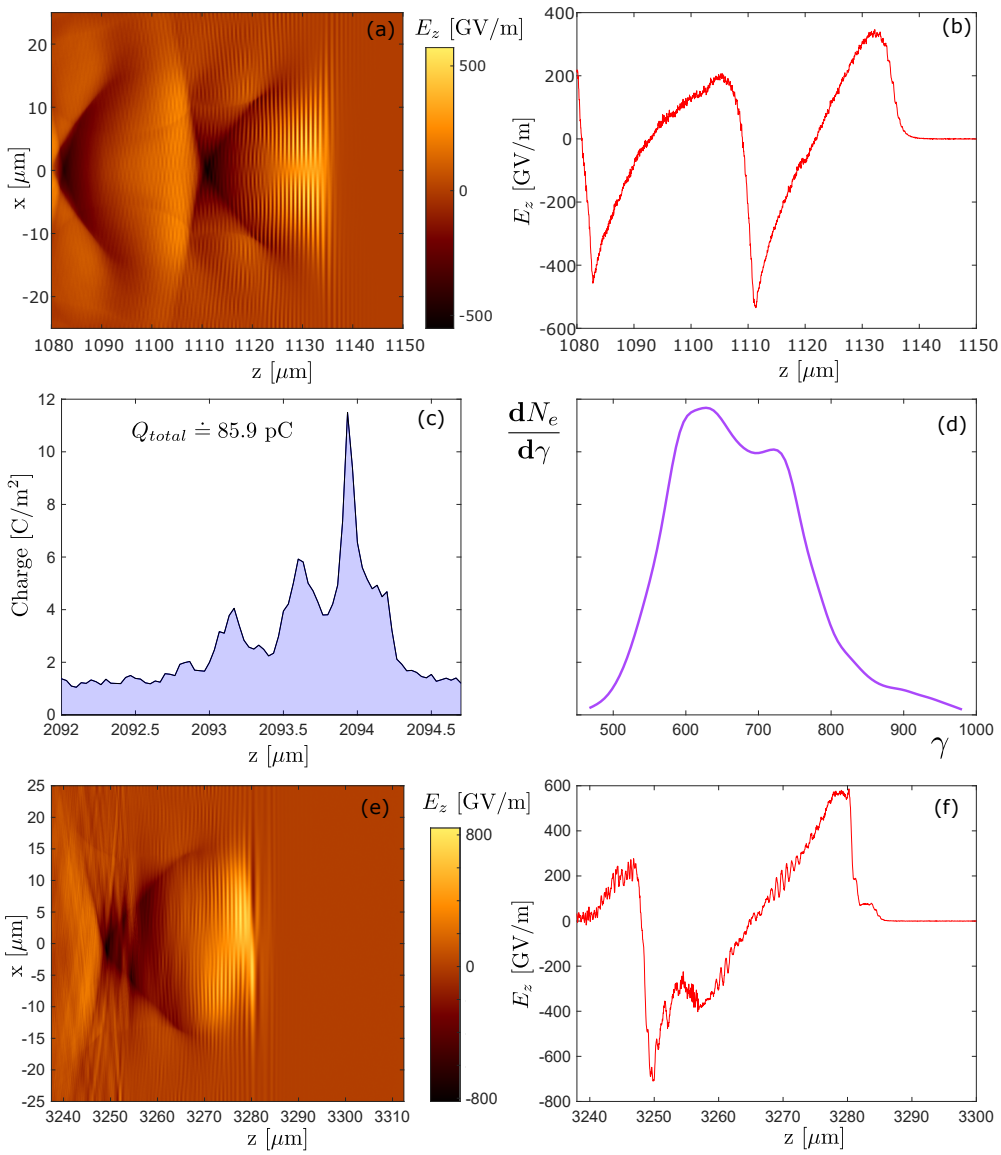

Figure 3.11: (a) Longitudal electric intensity E_z at t = 5.26 ps. (b) E_z at x = 0. (c) Charge density corresponding to the accelerated electron bunch integrated along x at t = 5.26 ps. (d) Energy spectrum of accelerated electrons in arbitrary units before dephasing t = 8.51 ps. (e) Longitudal electric intensity E_z at t = 12.45 ps. (f) E_z at x = 0.

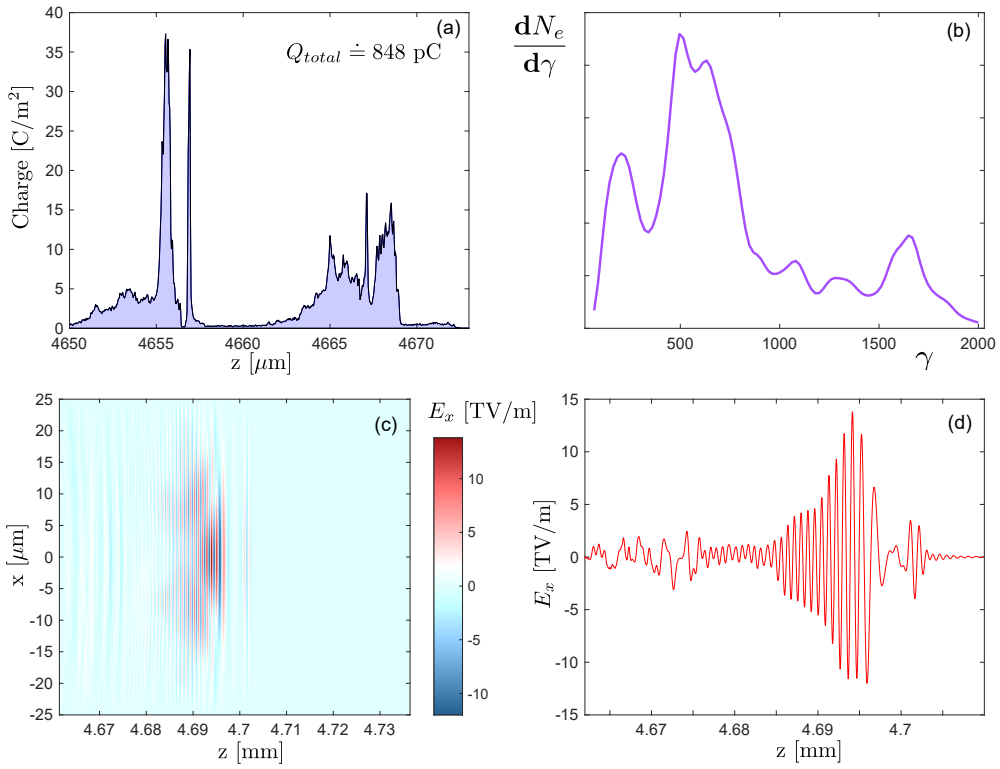

Figure 3.12: (a) Charge density corresponding to the second and third accelerated electron bunch integrated along x at t = 16.7 ps. (b) Energy spectrum of accelerated electrons in arbitrary units after exiting the gas target at t = 16.7 ps. (c) Modulated laser pulse after exiting the gas target. (d) Profile at x = 0.

According to radiation calculation algorithm presented at the beginning of this chapter, we can calculate the radiation emitted by the whole bunch, however such precision would be very computationally demanding, on the time scale of weeks. For such large number of electrons that we have in the simulation, we have instead carefully selected trajectories best characterizing electron bunches according to electron spectrum, trajectories and bunch charge results from the PIC results.

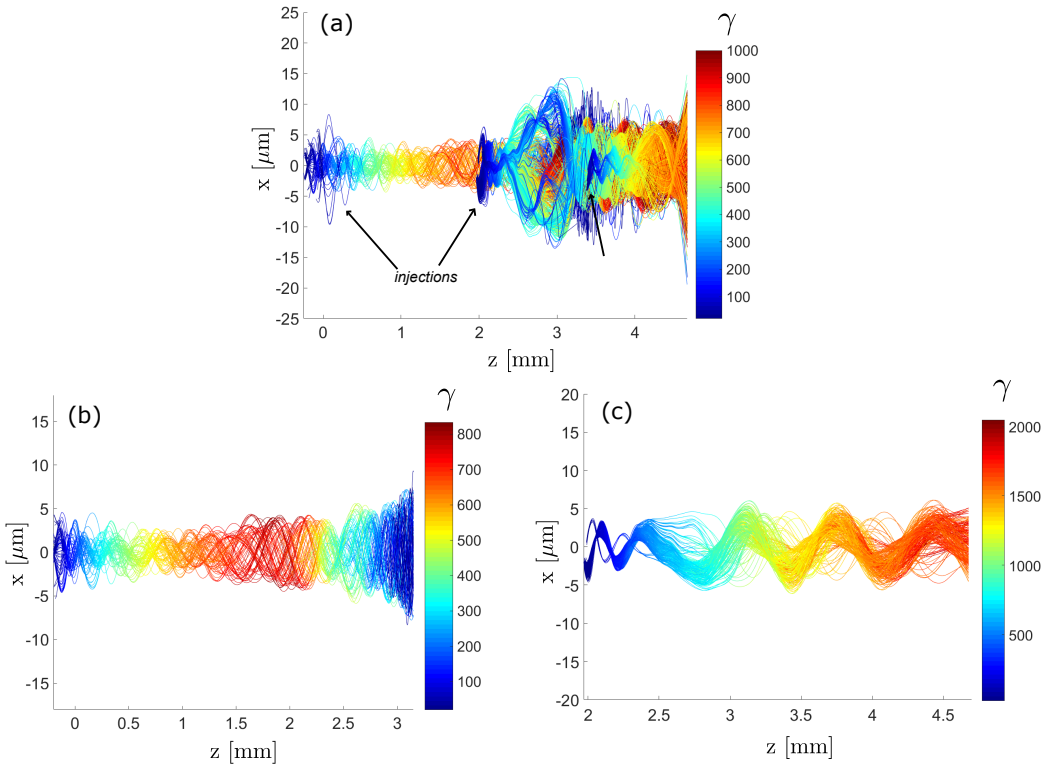

Figure 3.13: (a) Trajectories and gamma evolution of electrons. Maximum $\gamma = 1000$ to highlight distinct injection points. (b) Trajectories of the first injected electron bunch. (c) Trajectories of the second injected electron bunch.

In Fig. 3.13 (a), we've plotted trajectories of 0.1% of accelerated electrons within the PIC simulation. These post-processed trajectories highlight that, just as we've pointed out from the PIC results, there are mainly three major wave-breaking events where large numbers of electrons are injected into the accelerated phase. Trajectories of the first and the second bunch are highlighted in Fig. 3.13 (b), (c). We know from PIC results that the second bunch is roughly ten times as large as the first one, but it is also much more energetic, reaching up to 1 GeV before exiting the gas target. We also note that the trajectories follow a roughly similar evolution and therefore the radiation emitted by the electrons within the same bunch won't differ significantly. For the larger and higher energy bunch, we've selected two characteristic trajectories, results of both of which are in Fig. 3.14, 3.16. To also consider the effect of the first bunch, we present radiation results for the trajectory characteristic of the first bunch in Fig. 3.17.

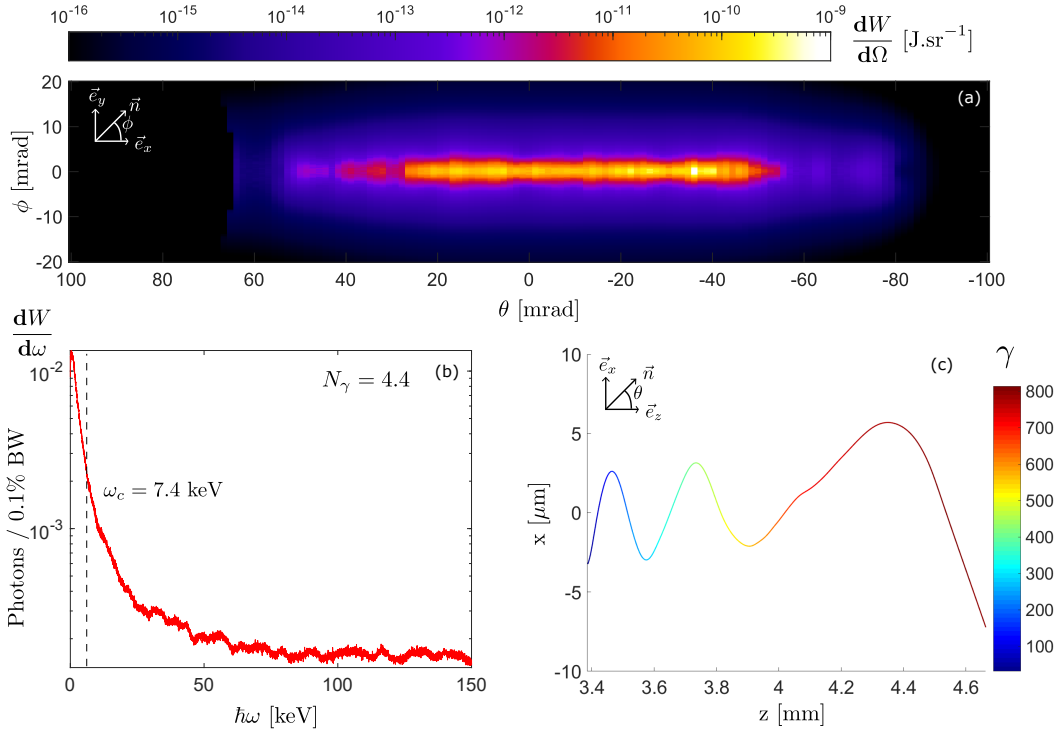

Figure 3.14: Radiation calculated for a $\gamma = 800$ electron. (a) Angular distribution of the radiated energy. (b) Radiation spectrum in logarithmic scale. (c) γ evolution of the electron.

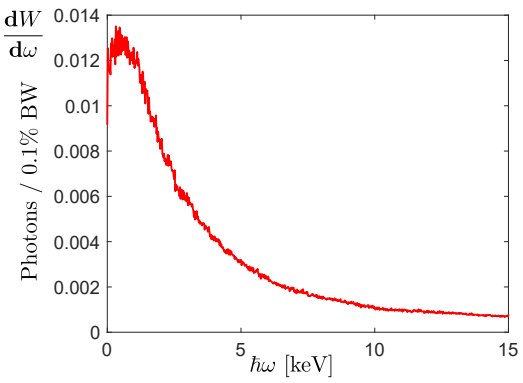

Figure 3.15: Betatron X-ray radiation spectrum in linear scale, highlighting the synchrotron-like shape.

Electron in Fig. 3.14 reaching up to $\gamma = 800$ emitted radiation with $1.7 \cdot 10^{-3}$ photons / 0.1% bandwidth at critical energy of $\omega_c \doteq 7.4$ keV. The total number of emitted photons per electron for this case is $N_\gamma \doteq 4.4$ with beam divergence at full width at half maximum of approximately ≈ 60 mrad. This trajectory characterizes the third injected bunch, which makes up the low energy part of the electron spectrum in Fig. 3.12 (b).

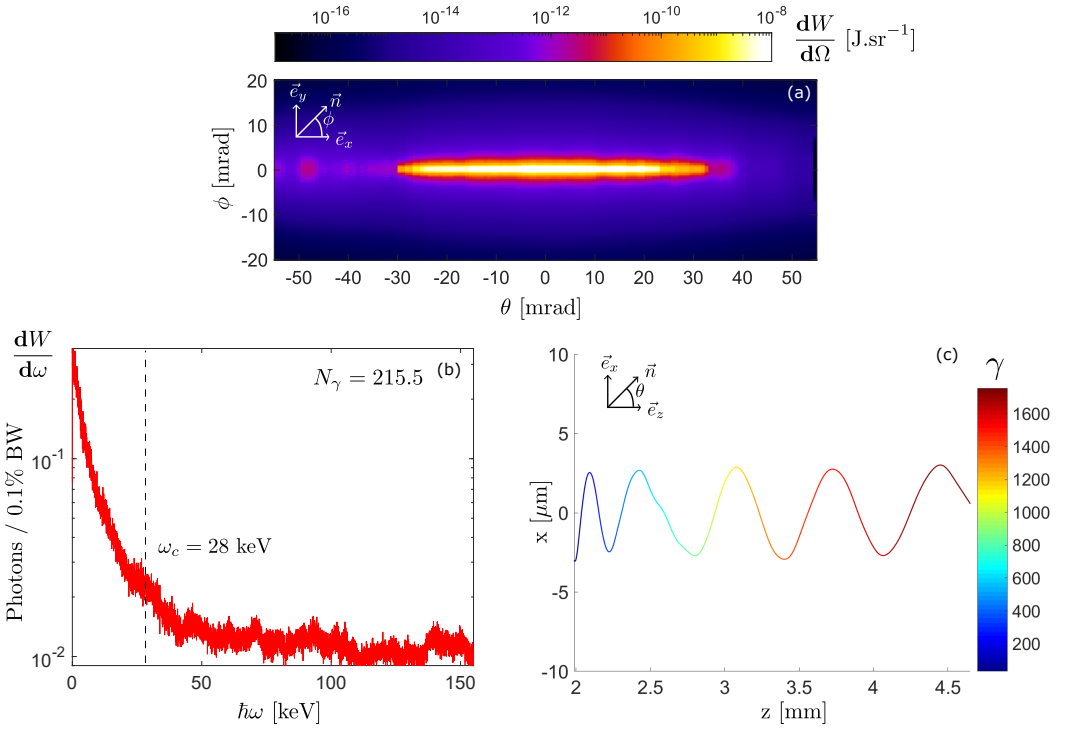

Figure 3.16: Radiation calculated for a $\gamma = 1600$ electron. (a) Angular distribution of the radiated energy. (b) Radiation spectrum in logarithmic scale. (c) γ evolution of the electron.

Electron in Fig. 3.16 reaching up to $\gamma = 1600$ emitted radiation with $2.3 \cdot 10^{-2}$ photons / 0.1% bandwidth at critical energy of $\omega_c \doteq 28$ keV. The total number of emitted photons per electron for this trajectory is $N_\gamma \doteq 215.5$ with beam divergence of approximately ≈ 20 mrad. This trajectory represents the higher energy tail of the electron spectrum in Fig. 3.12 (b), which consists of the second injected bunch. We can expect these electrons to boost the critical energy and photon flux for total emitted radiation near axis quite significantly.

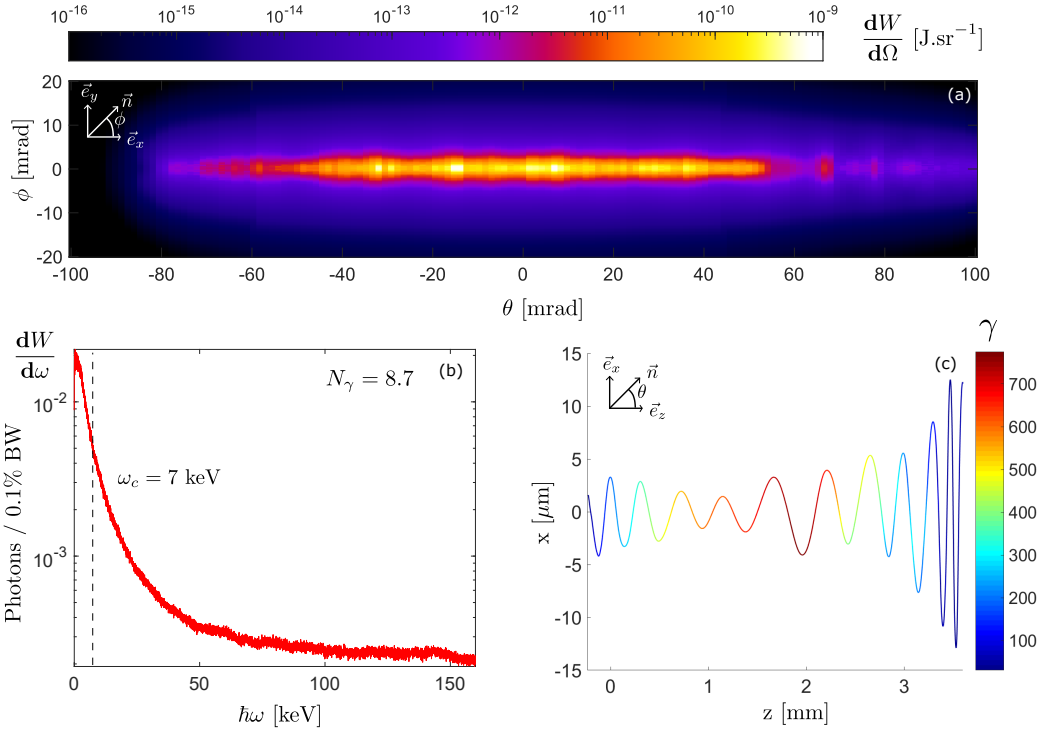

Figure 3.17: Radiation calculated for a $\gamma = 700$ electron. (a) Angular distribution of the radiated energy. (b) Radiation spectrum in logarithmic scale. (c) γ evolution of the electron.

Electron in Fig. 3.17 reaching up to $\gamma = 900$ emitted radiation with $5.4 \cdot 10^{-3}$ photons / 0.1% bandwidth at critical energy of $\omega_c \doteq 7$ keV. The total number of emitted photons per electron is $N_\gamma \doteq 8.7$ with beam divergence of approximately ≈ 60 mrad. This trajectory characterizes the first injected bunch with spectrum shown in Fig. 3.11 (d). This bunch is emitting lower energy radiation, with the spectrum however being still well above the 1 keV range with significant photon flux.

With the previous results, we can estimate the total radiation emitted per shot. With 848 pC of charge, the main bunch contains $5.29 \cdot 10^9$ electrons characterized by the first two trajectories. With the estimation that the higher energy trajectories make $\sim 20\%$ of the larger bunch, we get the total number of emitted photons per shot as $N_\gamma^{bunch} = 2.3 \cdot 10^{11}$. The smaller bunch of 84.8 pC contains only $5.29 \cdot 10^8$ electrons, contributing only $N_\gamma \approx 9$ photons per electron, that is $N_\gamma^{bunch} = 4.7 \cdot 10^9$ photons, or 2% of the total number of radiated photons. With this in mind, we conservatively estimate total emitted X-ray radiation with photon flux of $N_\gamma \doteq 2.4 \cdot 10^{11}$ photons per shot with $\sim 10^8$ photons / 0.1% bandwidth between 1 and 20 keV and $\sim 10^7$ photons / 0.1% bandwidth between 20 and 50 keV with beam divergence of $\theta \doteq 50$ mrad. The Betatron X-ray pulse length is roughly equal to the relativistic electron bunch length [71], which is in this case approximately 10 μm, making the X-ray pulse duration $\tau \approx 30$ fs. The source size is $d \approx 7$ μm.

Case III

Results of the PIC simulation for the case $n_0 = 10^{19}$ cm^{-3} are presented in figures 3.18, 3.19, 3.20 and 3.22. For this case we have omitted the snapshost of the laser pulse entering the gas jet, since it is same as the previous case. Some time into the simulation at t = 1.7 ps, the laser pulse is being sharply self-focused while exciting the plasma and we alredy see some accelerating electrons. At t = 3.4 ps (b), the wakefield is well estabilished and electrons are reaching $\gamma \approx 800$. A second wavebreaking event is triggered at approximately t = 3.82 ps (c) with the longitudal field approaching magnitude of 1000 TV/m as seen in Fig. 3.22 (a), (b). This wavebreaking triggered a continuous chain reaction where a very large number of electrons is injected, as seen at t = 6.35 ps (d). Due to the large number of electron macro-particles overlaping in the figures, we have separated two layers of electrons to highlight the energy range within the bunch with a dashed line. Presence of such large number of electrons however effectively increases the potential within the cavity, producing a shallow longitudal wakefield as seen in Fig. 3.22 (c), (d) with largest accelerating gradient at the back of the bubble. At t = 8.08 ps (e), the laser pulse is almost depleted and the electrons accelerated at the back of the bubble attained highest energy, while injection still continues. Electrons continue to accelerate in the shallow wakefield at t = 10.91 ps (f) with the laser pulse almost completely depleted. Charge of the bunch and energy spectrum are highlighted in Fig. 3.22 (e), (f) with total charge of the bunch being $Q_{total} \doteq 1.22$ nC. At t = 12.10 ps, the laser wakefield is depleted and the wakefield starts to collapse, which allows the Coulombic repulsion of the electrons to expand the bunch in transverse direction. When the wakefield is depleted, the Coulombic repulsion diverges the electrons off-axis. Divergence of the exiting electron beam is $\theta \approx 20$ mrad.

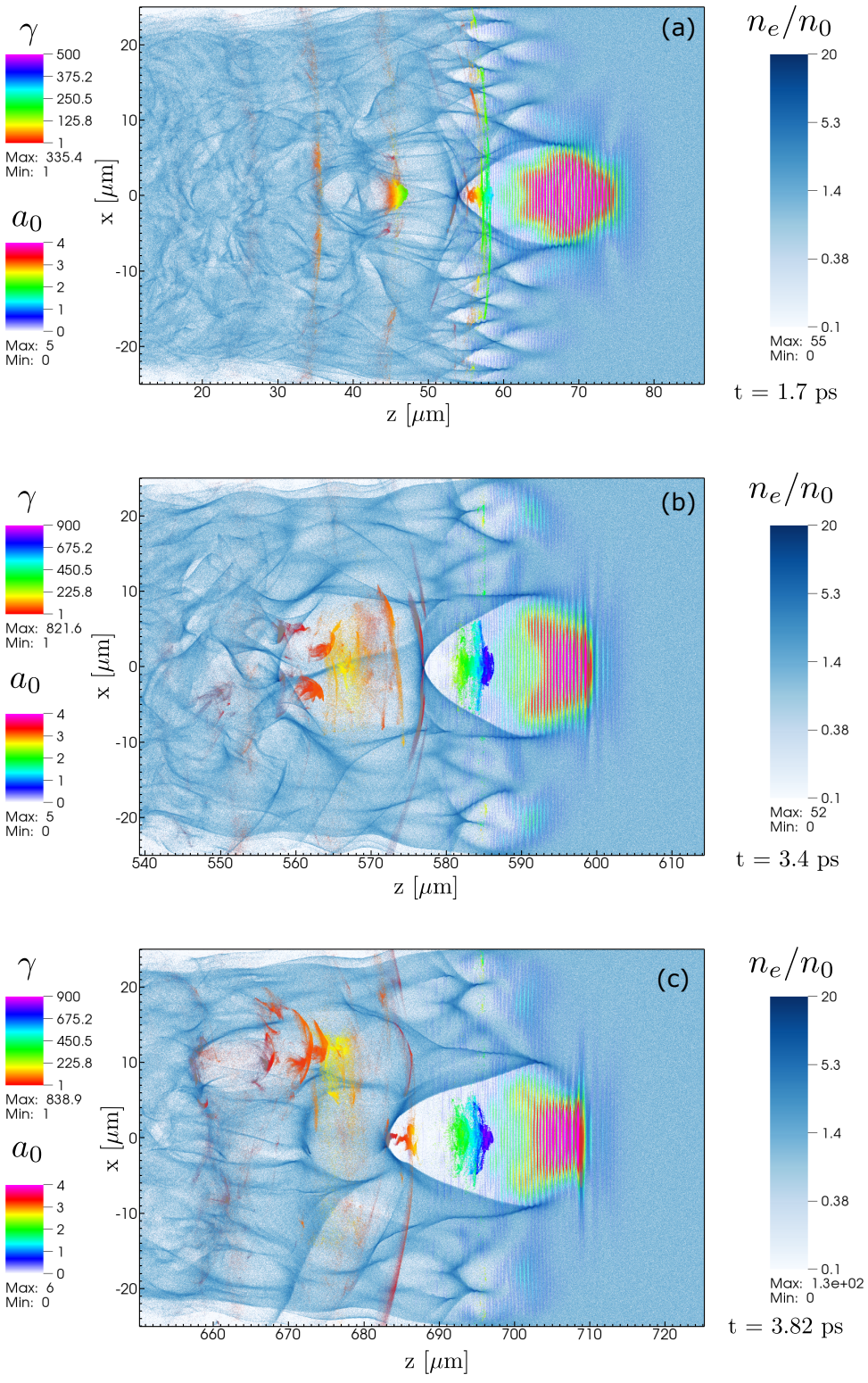

Figure 3.18: PIC simulation results in normalized units. (a) Laser pulse is exciting the plasma wakefield and undergoes self-focussing. First electrons are being accelerated. (b) Electrons are accelerated by the wakefield while the laser pulse loses energy. (c) Second large bunch is injected.

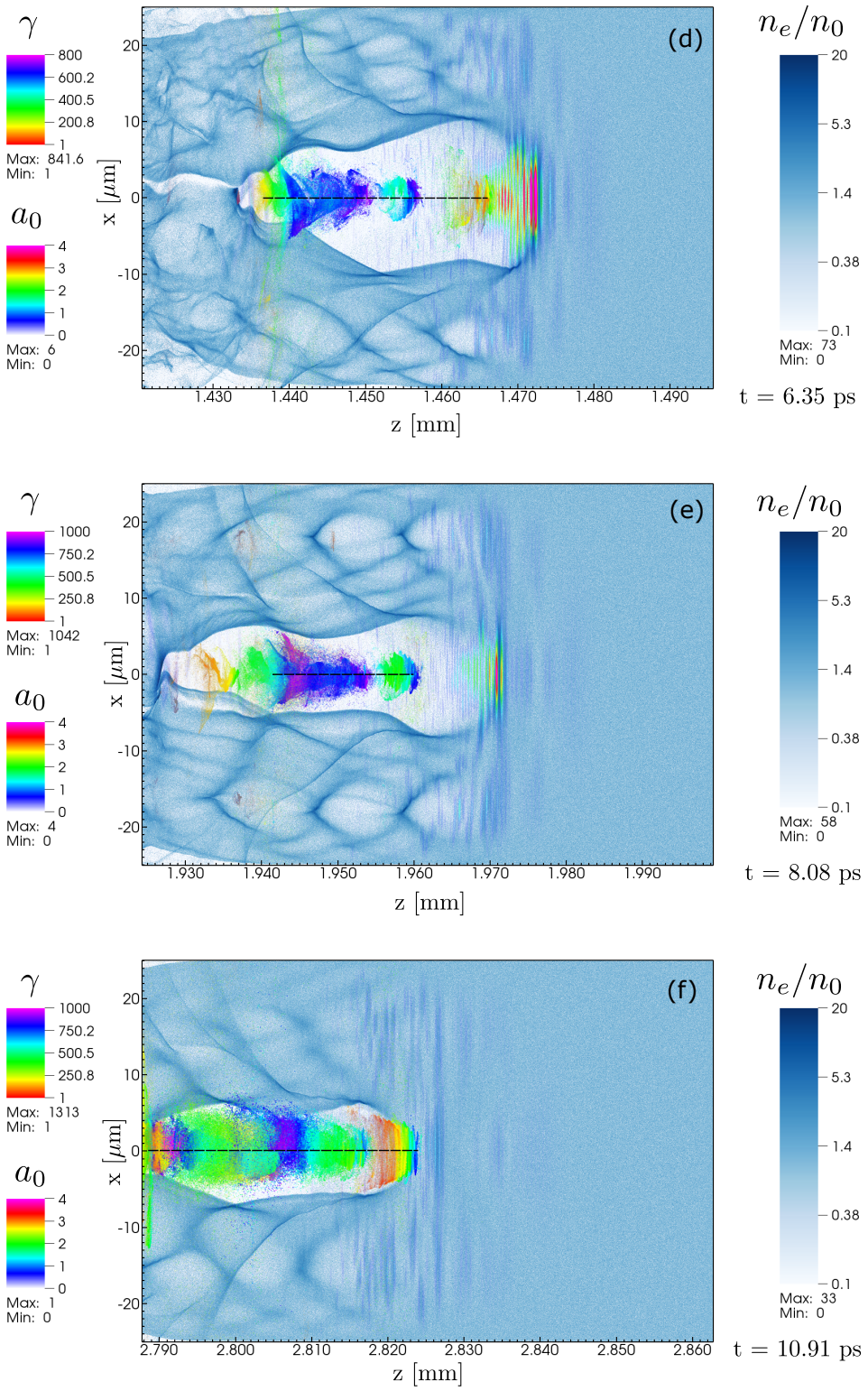

Figure 3.19: PIC simulation results in normalized units. (d) The second injection triggered chain wavebreaking, injecting large number of electrons. (e) Wavebreaking continues at the back of the wakefield, laser pulse front is depleted. (f) Large number of electrons continue to accelerate in the shallow wakefield while laser pulse is almost completely depleted.

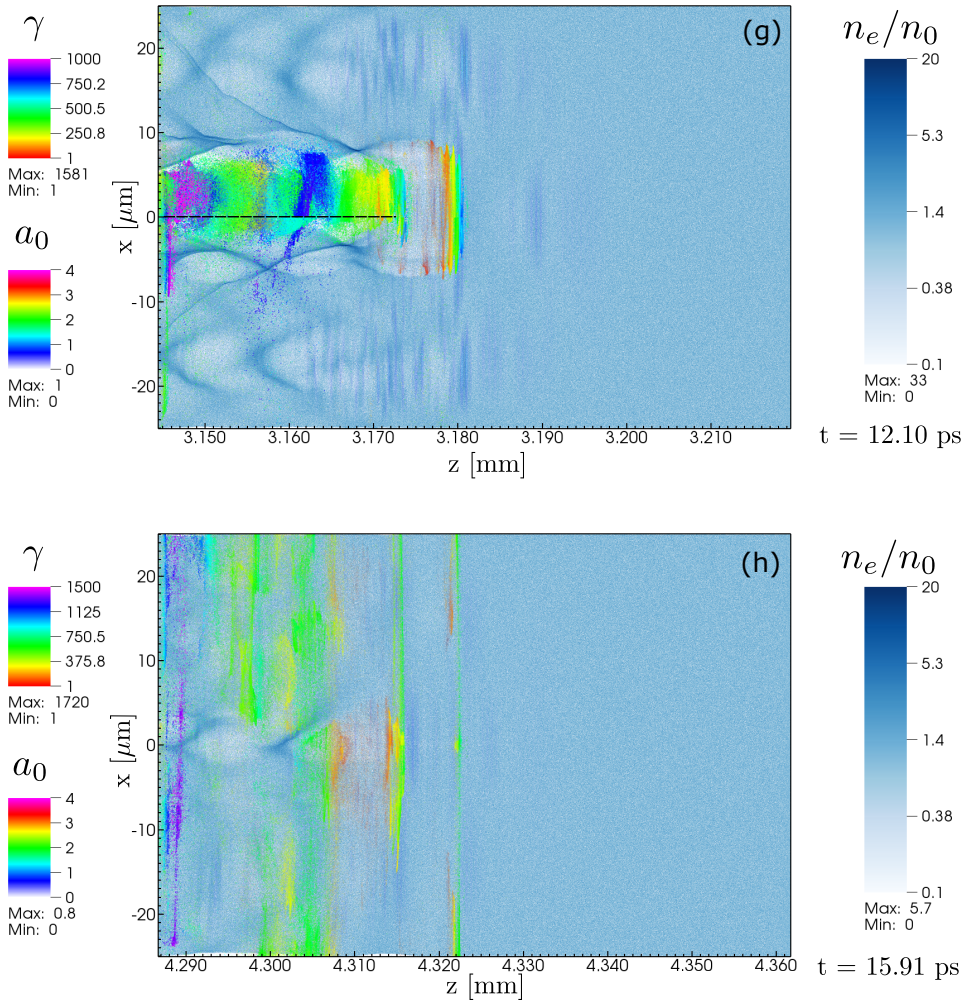

Figure 3.20: PIC simulation results in normalized units. (g) Laser is depleted and wakefield starts to collapse. (h) Wakefield is collapsed and Coulombic repulsion within the accelerated bunch causes individual electrons to diverge off axis.

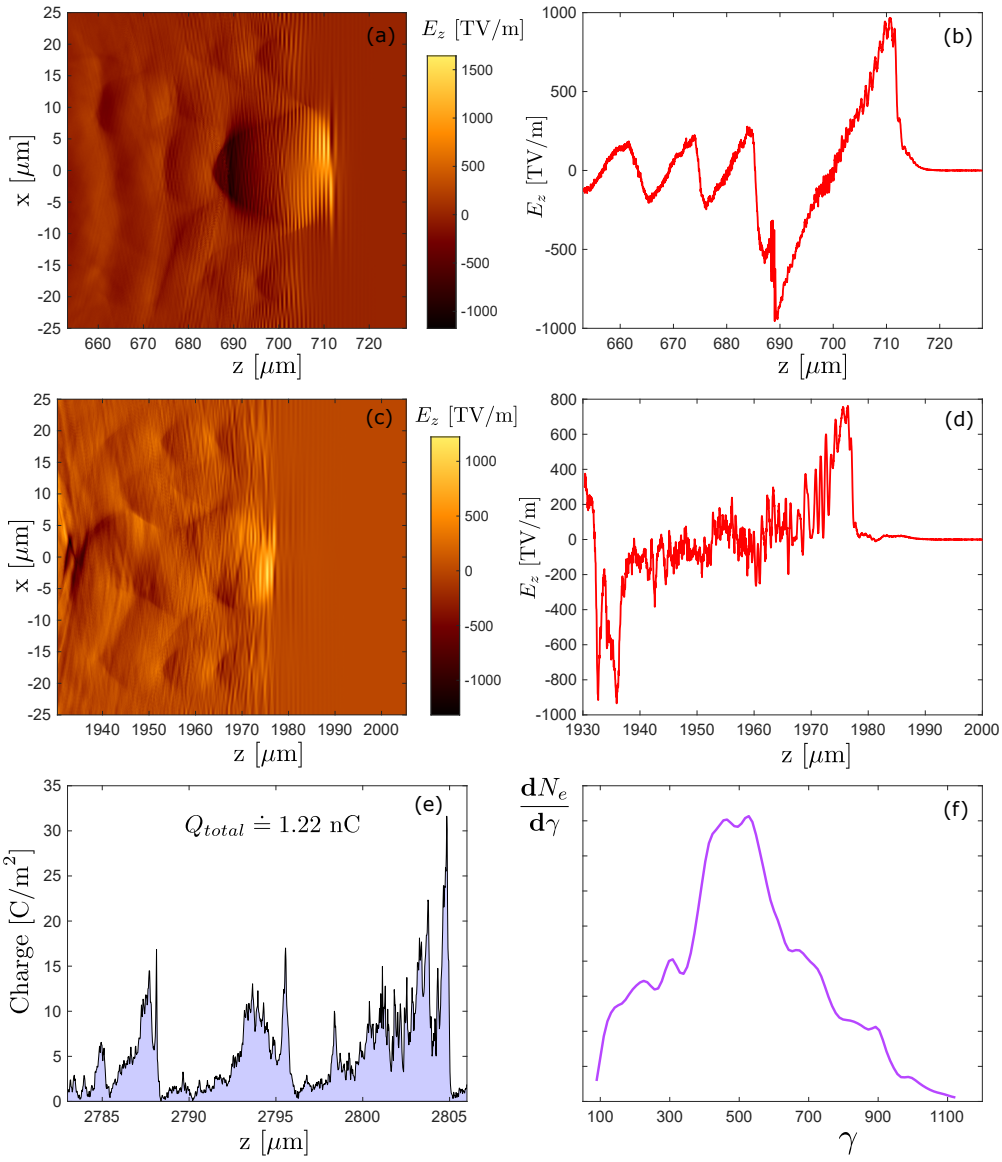

Figure 3.21: (a) Longitudal electric intensity E_z at t = 3.82 ps. (b) E_z at x = 0. (c) Longitudal electric intensity E_z at t = 8.08 ps. (d) E_z at x = 0. (e) Charge density corresponding to the accelerated electron bunch integrated along x at t = 10.91 ps. (f) Energy spectrum of accelerated electrons in arbitrary units before scattering at t = 10.91 ps.

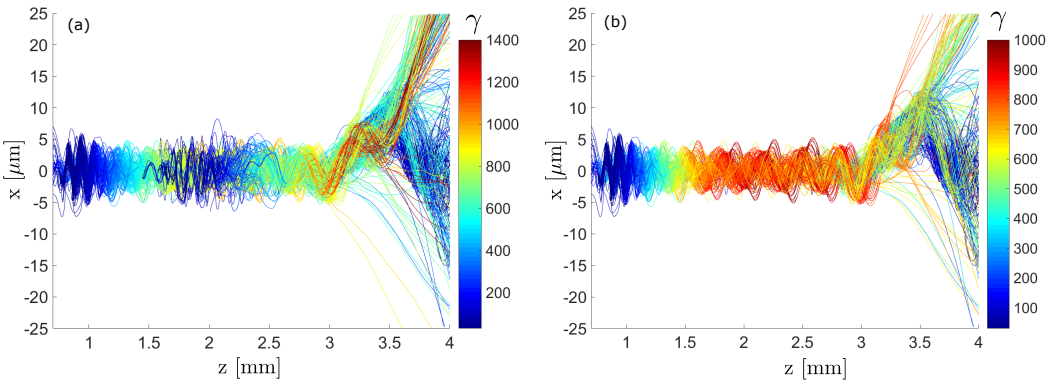

Figure 3.22: (a) Trajectories and gamma evolution of electrons. Maximum $\gamma = 1400$ to highlight distinct major injection points. (b) Trajectories of the first and major accelerated electron bunch.

Trajectories of accelerated electrons are plotted in Fig. 3.22. Trajectories of 0.1% of the accelerated electrons are shown in (a). While continuous injection was indeed happening throughout most of the propagation, we see that there are two particular wavebreaking events that injected considerable amount of particles. The larger of the two is shown in (b). Once again, we have selected characteristic trajectories representing these bunches to estimate the total emitted radiation per shot.

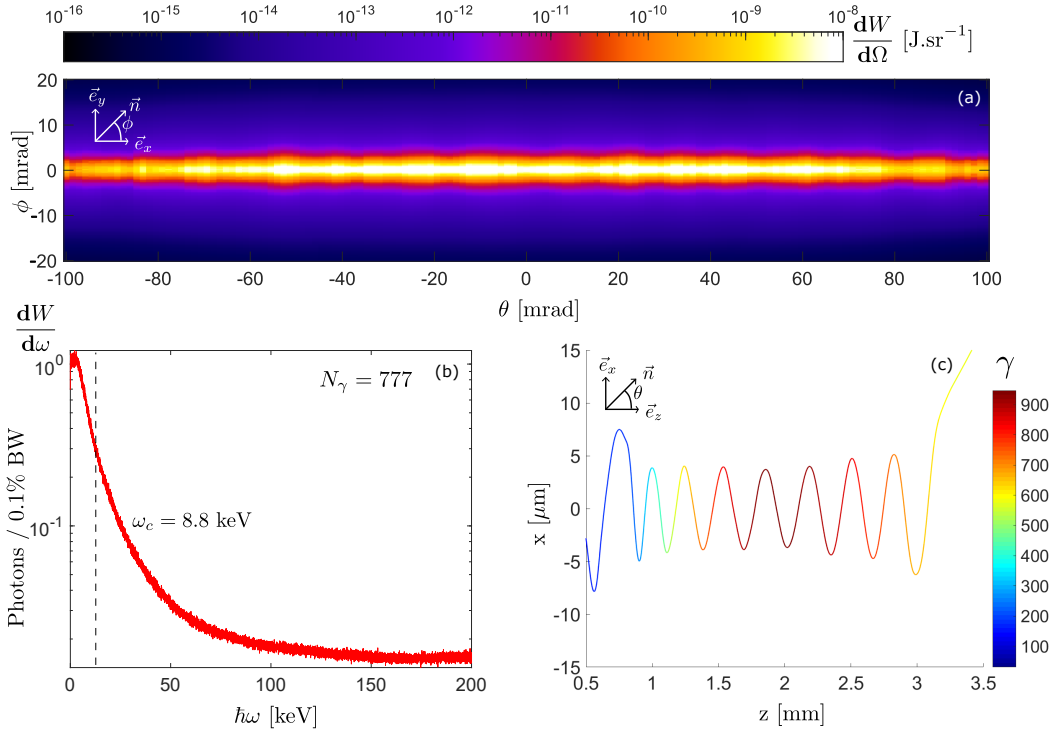

Figure 3.23: Radiation calculated for a $\gamma = 900$ electron. (a) Angular distribution of the radiated energy. (b) Radiation spectrum in logarithmic scale. (c) γ evolution of the electron.

First trajectory selected of an electron reaching $\gamma = 900$ is representative of the major bunch injected at $z \doteq 0.75$ mm highlighted in Fig. 3.22, (b). While the achieved electron energy is smaller compared to the previous density case, we have much higher number of photons emitted per electron $N_\gamma = 777$ with a significant amount of $4.7 \cdot 10^{-1}$ photons / 0.1% bandwidth emitted at critical energy $\omega_c = 8.8$ keV. The X-ray beam divergence is ≈ 120 mrad. While the betatron oscillation amplitude is similar to previous density case, all the oscillations at high energy are conducted in a much shorter length of ~ 2.5 mm, which significantly increases the deflection parameter K. That signifies sharper turns and therefore stronger transverse acceleration at these turning points, resulting in larger amounts of radiated energy.

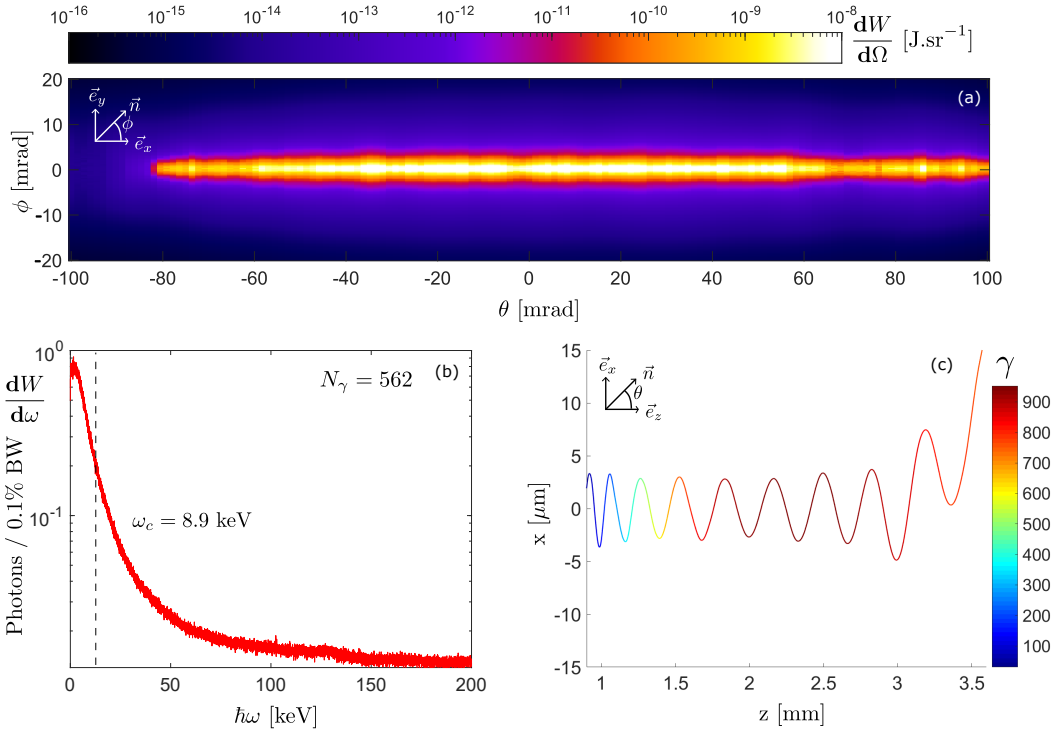

Figure 3.24: Radiation calculated for a $\gamma = 900$ electron. (a) Angular distribution of the radiated energy. (b) Radiation spectrum in logarithmic scale. (c) γ evolution of the electron.

Trajectory with $\gamma = 900$ is another one of the many almost identical trajectories of the first injected bunch of electrons at $z = 0.7$ mm. We observe $3.5 \cdot 10^{-1}$ photons / 0.1% bandwidth at critical energy $\omega_c = 8.9$ keV with total number of photons $N_\gamma = 562$. Trajectories within the first bunch seem to emit very similar radiation. Beam divergence is ≈ 100 mrad.

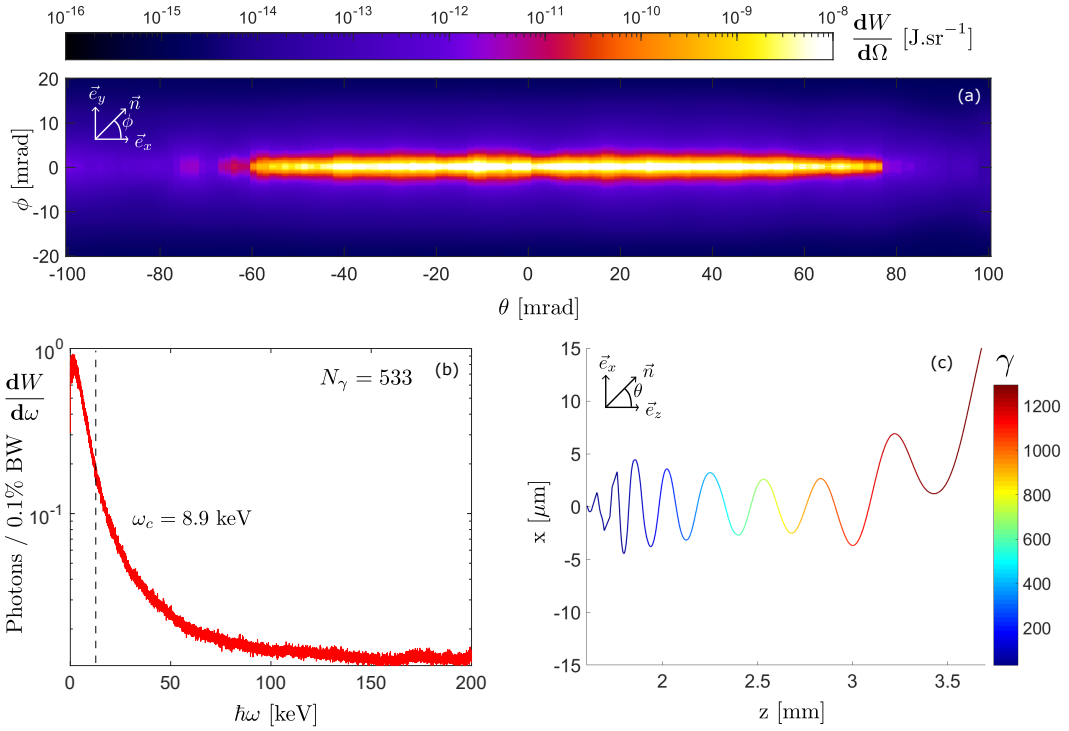

Figure 3.25: Radiation calculated for a $\gamma = 1200$ electron. (a) Angular distribution of the radiated energy. (b) Radiation spectrum in logarithmic scale. (c) γ evolution of the electron.

At last, we consider the contribution of trajectory with $\gamma = 1200$. This electron characterizes the second bunch injected at $z \approx 1.7$ mm. The radiation has divergence of ≈ 100 mrad with $N_\gamma = 533$. We observe $3.4 \cdot 10^{-1}$ photons / 0.1% bandwidth at $\omega_c = 8.9$ keV.

With the calculated photon flux of the presented trajectories, it seems reasonable to us to conservatively estimate that radiation from higher energy electrons injected within the main bunch dominates within the total radiation emitted per shot. The total charge is 1.22 nC, which is approximately $7.6 \cdot 10^9$ electrons. Electrons with γ above 600 at $t = 10.91$ ps make $\sim 40\%$ of the accelerated electrons. Considering these radiate ~ 500 photons per electron, we estimate the total emitted X-ray radiation per shot with photon flux of $N_\gamma \doteq 1.6 \cdot 10^{12}$ photons per shot with $\sim 10^9$ photons / 0.1% bandwidth between 1 and 15 keV and $\sim 10^8$ photons / 0.1% between 15 and 50 keV with beam divergence of $\theta \doteq 100$ mrad. Electron bunch length of ≈ 20 μm makes the X-ray pulse length $\tau \approx 65$ fs. The source size is $d \approx 7$ μm.

3.4 Summary

We have conducted a PIC simulation parametric scan with variable gas density. For the first case of $n_0 = 3 \cdot 10^{18}$ cm^{-3}, we have found that almost no significant charge $Q_{total} \sim pC$ is being injected into the accelerating phase due to the inability of lower gas density to promote wavebreaking in such short gas target of 5 mm. This case is however potentially of interest for multi-stage or density tailored electron accelerating setups [56] [57] due to it's large accelerating gradient and wakefield stability. This wakefield stability reflects in it's potential to accelerate electron beams over long distances, as it was shown in [21], where 5 pC charges were accelerated up to record breaking 8 GeV over 15 Rayleigh lengths with density of $n_0 = 3.4 \cdot 10^{17}$ cm^{-3}.

The second case of $n_0 = 5 \cdot 10^{18}$ cm^{-3} revealed the necessity for high density in all-optical single stage homogeneous gas targets for electron injection and betatron X-ray generation. Broadband radiation within 1 - 150 keV range with photon flux of $2.4 \cdot 10^{11}$ photons per shot was estimated. The last case of $n_0 = 10^{19}$ cm^{-3} further supports this photon flux scaling. Radiation within 1 - 200 keV range with photon flux of $1.6 \cdot 10^{12}$ photons per shot was calculated, further indicating the need for higher density in betatron X-ray radiation generation with petawatt laser systems. These results suggest that with high intensity laser pulses with peak $a_0 \sim 4$, higher densities are favorable for X-ray generation within the gas density range of 10^{18-19} cm^{-3} in homogeneous gas targets. Our results also support recent experimental work that shows that Betatron X-ray radiation with photon flux of 10^{8-10} photons/sr/0.1%BW/shot in a 10 - 40 keV energy band can be generated with petawatt scale laser systems [74]. Another recent work also indicates that X-ray photon flux with these gas targets could be further enhanced with tailored density modulation [57].

4. Experimental Design

In this chapter, we will present the design for the Betatron X-ray source in the Plasma Physics Platform (P3) vacuum chamber [75] in the E3 experimental hall at ELI-Beamlines. The driving laser for the Betatron X-ray source will be the L3 petawatt-class laser system with energy of 30 J operating at repetition rate of 10 Hz reaching up to 1 PW. Due to LWFA laser requirements discussed in Chapter 3, the laser pulse must be optimally focused on target to match the plasma density. Above critical peak power, the laser propagates through the target self-focused and oscillates around w_0 before it loses enough energy to continue self-focusing. To partially counter this and especially in the case of experiments with lower powered laser pulses, longer focusing length must be selected to mitigate diffraction [71]. Optimal X-ray generation demands larger f-number f/N, ideally above 10 with spherical mirrors, which was shown for example at Astra-Gemini ($f/17$) [76] or Texas Petawatt ($f/47$) [77].

In our case, a spherical mirror with a focusing length $f = 5$ m gives at full aperture the f-number larger than $f/20$. Optical simulation in Fig. 4.1 shows that this focusing provides a spot size close to the diffraction limit at $2w_0 \approx 40$ μm. From previously mentioned experimental works and preliminary simulations presented, we expect $\sim 10^9$ electrons with a total charge of ~ 100 pC and energy of 400 - 1500 MeV. X-ray radiation is expected with tunable critical energy up to ~ 50 keV, divergence of 20 mrad, pulse duration of sub 10 fs with a photon flux of 10^{10} per shot [78].

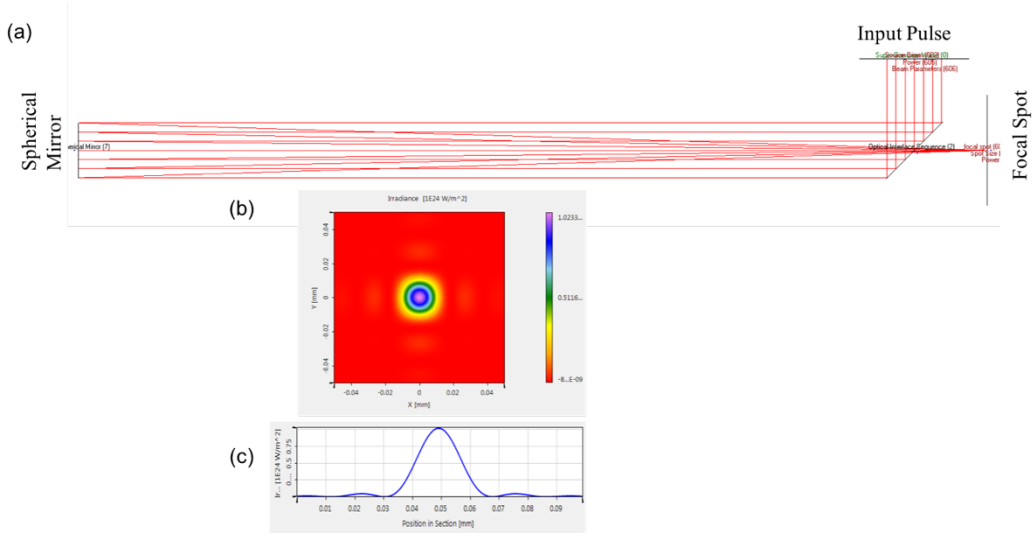

Figure 4.1: (a) Optical simulation setup in Virtual Lab optical simulation package. The L3 laser beam is reflected by the mirror with hole and reflected to the spherical mirror, which focuses it back through the mirror with hole. (b),(c) Typical focal spot and intensity profile at the focus showing the focal spot diameter of about 40 microns.

4.1 Experimental Setup

The experimental setup in P3 chamber is shown in Fig. 4.2 including the spherical mirror. Close-up of the experimental layout in P3 chamber is highlighted in Fig. 4.3. The L3 beam (yellow) enters from the bottom of the P3 chamber (at 6 o'clock), and is reflected by a mirror with a hole upon the long focal length spherical mirror (f = 5 m) in the adjacent vacuum chamber. The beam is then focused onto the gas target accelerating electrons and generates betatron X-ray radiation. Multiple diagnostics are used to characterize the interaction. A vacuum compatible integrated charge circuit is placed behind the gas target to measure electron bunch charge. A dipole magnet with scintillating screen is placed in laser propagation direction behind the gas target to deflect the electrons, serving as electron spectrometer. Part of the L3 beam is transmitted from the laser beam through the mirror with a hole. This split off beam (green) is used for plasma diagnostics such as shadowgraphy or interferometry, since it is in phase with the main beam. Focal spot diagnostics (purple) and Thomson scattering (top view, red) are also included to serve as additional diagnostics, providing information on laser and plasma behaviour. The betatron X-ray beam (blue) is transmitted through a laser reflecting foil and recorded by a back-illuminated X-ray CCD camera or X-ray detecting screen viewed by a CCD camera. X-ray spectrometers covering the broadband Betatron radiation from few keV to 100s of keV are placed before the X-ray detector.

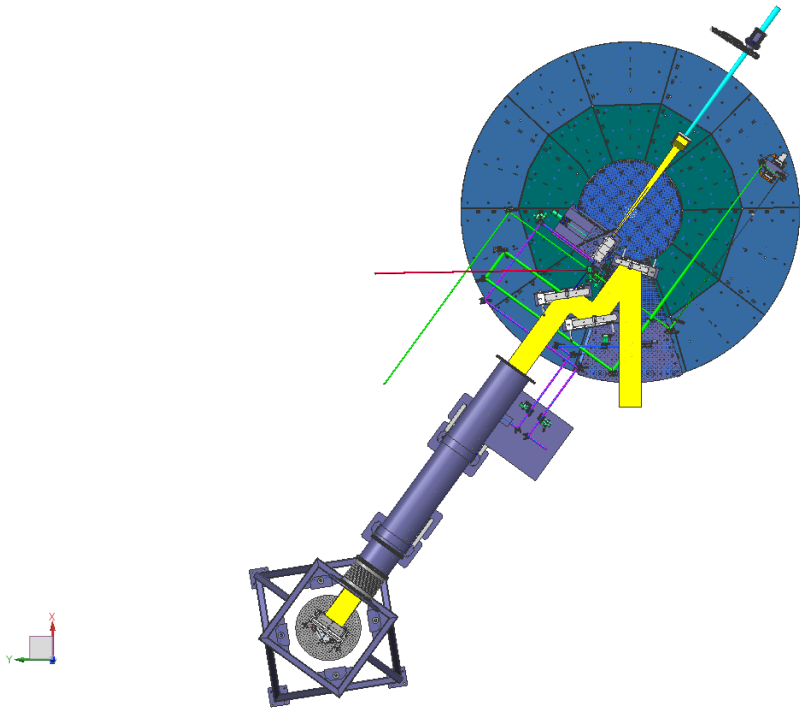

Figure 4.2: 3D model of the experimental setup in P3 chamber. L3 beam (yellow) enters from the bottom of the chamber and continues onto the spherical mirror in adjacent vacuum chamber.

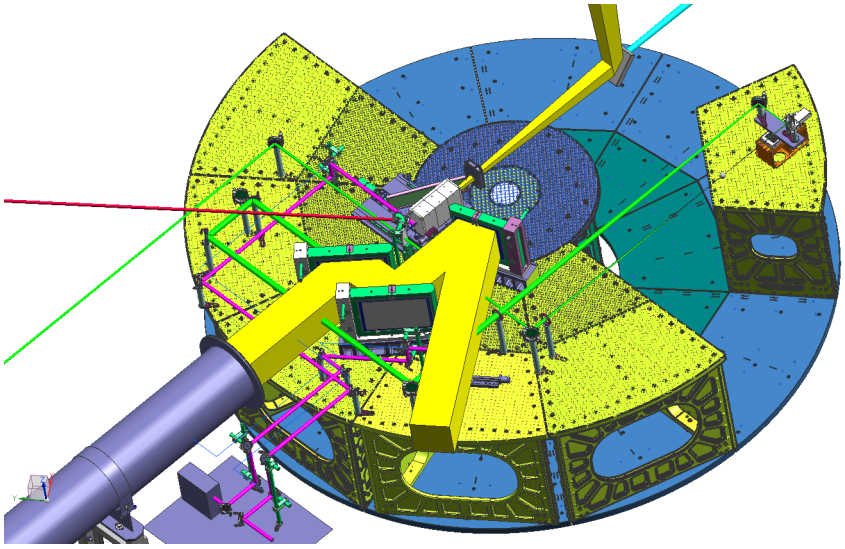

Figure 4.3: Close-up of the experimental layout for the betatron generation with diagnostics. L3 beam (yellow), interferometry beam (green), L3 diagnostics (purple), Thomson scattering (red), X-ray beam (blue).

4.1.1 Gas Target

The gas jet has been designed to provide either sub or supersonic flows appropriate for a repetition rate of 10 Hz. The gas target can be characterized with a Mach-Zehnder or Wollaston prism interferometer. This provides information about gas density of the target, which allows us to compare the experiment with simulations in greater detail. The nozzles are mounted on solenoid valves triggered and opened for ≈ 10 ms before the laser pulse arrives. Typical density ranges between $10^{18} - 10^{19}$ cm^{-3}. This density is set by proper backing pressure of the gas jet, which is remote controlled by pressure regulators.

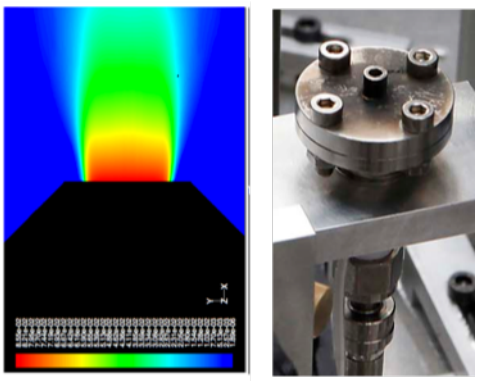

Figure 4.4: Left: Density profile of a cylindrical 4 mm de Laval nozzle. Right: Typical supersonic gas jet system.

4.1.2 Thomson Scattering

The laser pulse is scattered by free electrons through Thomson scattering. The intensity of scattered radiation depends linearly on laser intensity, which makes the measurement of Thomson scattering useful to monitor the laser propagation and electron density inside the gas target. The plasma is imaged by an achromatic doublet with magnification that will depend on the selected nozzle. The magnification may vary from 2 to 10.

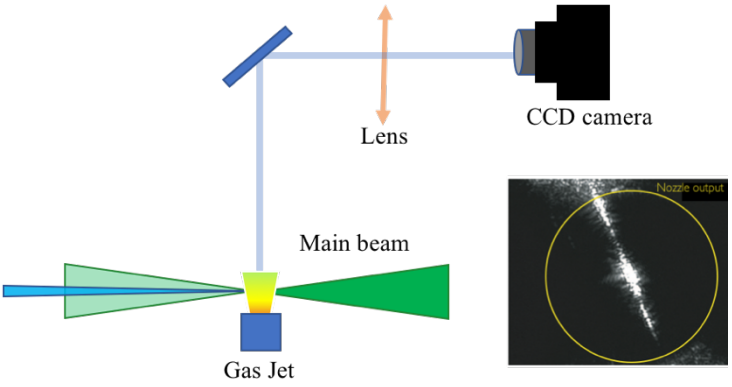

Figure 4.5: Thomson scattering (top view) imaging setup. Inset: Typical topview image.

4.1.3 Interferometry / Shadowgraphy

Information about plasma density is obtained through interferometry. Either the Mach-Zehnder or Wollaston prism interferometer can be selected for this purpose. Each can be chosen based on the availible space within the interaction chamber for a given experiment. Shadowgraphy provides us the laser position inside the plasma as a function of time. Both shadowgraphy and interferometry use the same setup. The plasma is imaged once again with an achromatic doublet with a magnification ranging from 2 to 10.

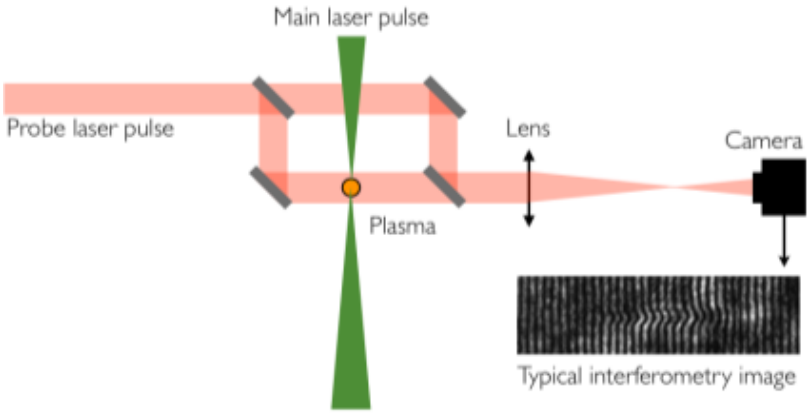

Figure 4.6: Mach-Zehnder interferometry setup.

4.1.4 Electron Diagnostics

A turbo integrated charge circuit (ICT) with a dynamic range of 80 dB capable of resolving fC scale pulsed charges is placed beyond the gas target to measure the charge of the electron bunch. The stability and divergence of the outcoming accelerated electron beam is measured through shot-to-shot pointing stability with the use of a scintillator screen and CCD camera along the beam path. A thin metallic filter is placed before the scintillator to block the laser radiation. The scintillator mostly emits green light around 546 nm. A bandpass filter for this wavelength is utilized to reduce noise. A 30 cm long magnetic spectrometer is used to deflect electrons with energies up to 1.5 GeV onto a scintillator screen viewed by a 14-16 bit CCD camera. The on-axis magnetic field is roughly 1.1 T for a 10 cm long segment. Three such modules are combined to produce a 30 cm long field that allows good resolution up to 1.5 GeV. The distance from the magnet to the 60 cm wide scintillator is around 10 cm.

Figure 4.7: Vacuum compatible turbo integrated charge circuit.

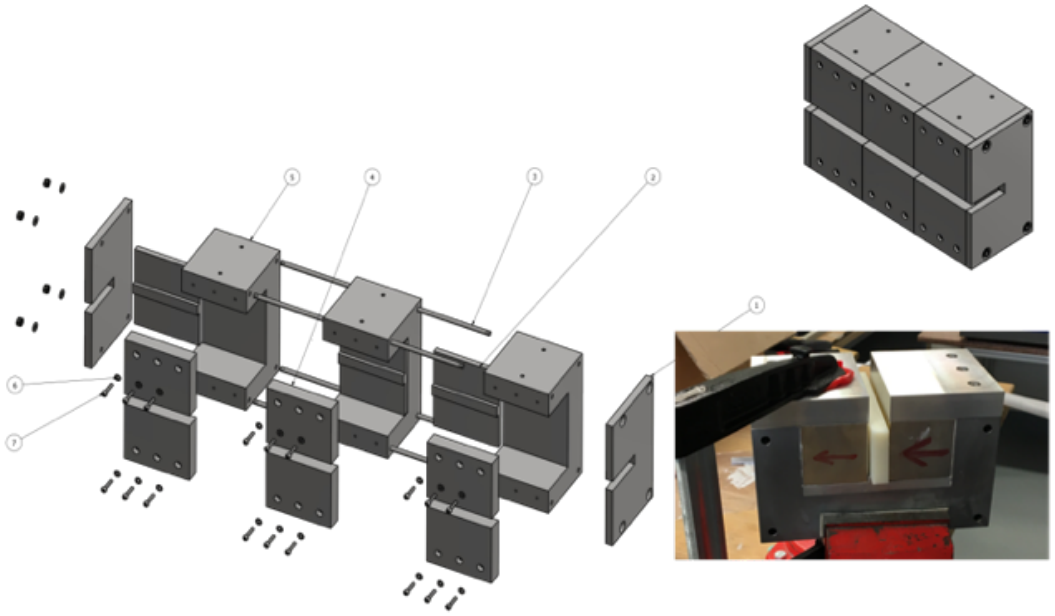

Figure 4.8: Design and assembly of the modular magnetic spectrometer. Inset: one 10 cm modular piece of the spectrometer.

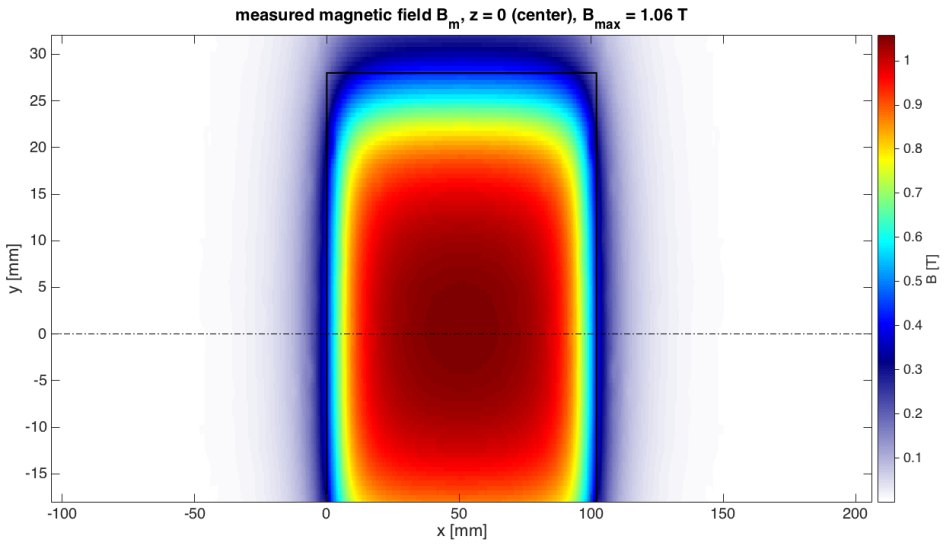

Figure 4.9: Magnetic field inside the 10 cm long module measured with a Hall sensor.

4.1.5 X-ray Diagnostics

The profile of the X-ray beam is measured with various tools depending on the energy of the radiation. X-ray cameras can directly image radiation up to 10 keV or even 20 keV for deep depletion chip types. Hard X-ray camera with scintillator can be used for indirect detection of radiation with energy up to the MeV range. Scintillator screens with various thickness and material or crystals can also be used depending on energy of the source.

For a source below 30 keV, single photon counting CCD will be used with filters in front of the detector to attentuate the X-ray signal and detect less than one photon per 10 pixels. In that case, the signal produced by one photon is directly proportional to it's energy and spectrum is obtained. For radiation below 100 keV, spectrum is measured using Ross filter pairs. The transmission difference in each filter pair allows to extract the radiation in a limited spectral band. By using multiple pairs with various materials, we can obtain spectrum up to 100 keV with 10 spectral bands. The X-ray spectrum is reconstructed using the knowledge of the filter transmission and fitting with the synchrotron radiation function. For X-rays over 100 keV, transmission through a thick filter will be used.

Figure 4.10: X-ray camera for the measurement of beam profile.

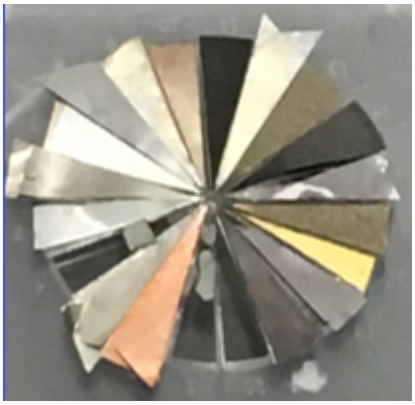

Figure 4.11: High energy X ray Ross filter spectrometer developed at ELI Beamlines. The spectrometer consists of 19 filters, which makes 10 spectral bands covering the spectrum from 5 keV to 88 keV.

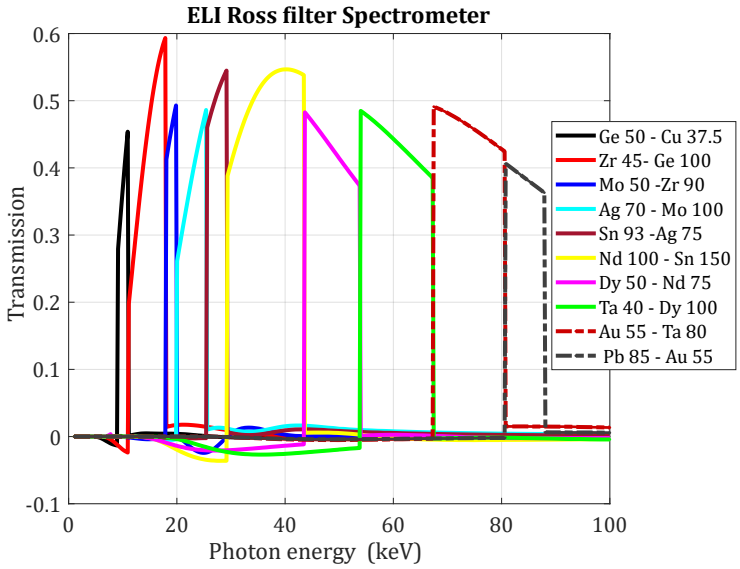

Figure 4.12: The spectrometer consists of 19 filters, which makes 10 spectral bands covering the spectrum from 5 keV to 88 keV.

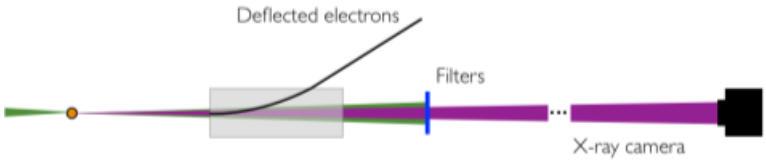

Figure 4.13: Schematic for the spectral characterization of the X-ray source through Ross filter pairs.

5. Imaging Applications

Compared to visible light, shorter wavelengths of X-ray radiation allow it to penetrate thicker structures and resolve finer details. These properties make X-ray radiation an ideal tool for crystallography, biological and medical imaging [79]. However, radiation damage is a factor that must be taken into consideration with X-ray sources. The nature of Betatron X-ray radiation generation through acceleration of μm scale electron bunches makes the Betatron source an ideal candidate for X-ray absorption and phase contrast imaging due to it's small source size [79]. In this chapter, we will present various imaging methods and consider their viability for the expected parameters of the Betatron source generated with L3 laser system at ELI Beamlines. The necessity for a small source size in imaging methods can be seen from a simple geometric consideration, which is highlighted in Fig. 5.1 with the maximum geometric unsharpness U given in terms of source size f, distance from source to sample a and distance from sample to detector b as

$$U = \frac{f \cdot b}{a} \tag{5.1}$$

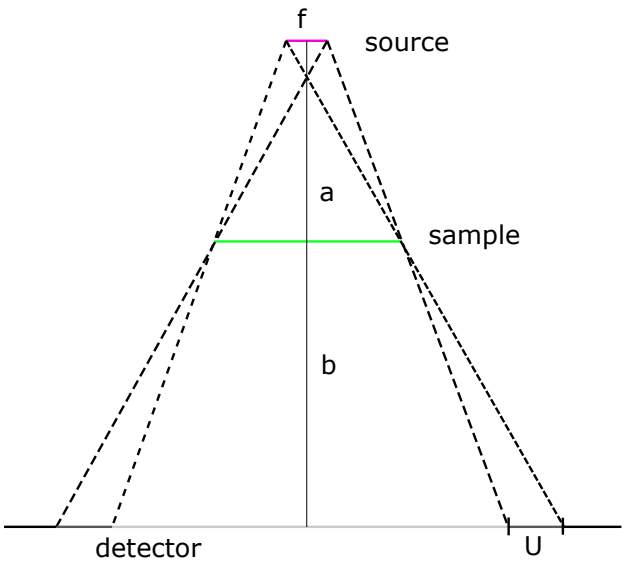

Figure 5.1: Schematic for the derivation of geometric unsharpness.

An ideal point source $f \to 0$ is therefore best for obtaining sharpest details and therefore good resolution of the sample.

5.1 Absorption-Contrast Imaging

This technique utilizes the fact that an X-ray beam passing through a sample of different components, for example a biological cellular structure, suffers attentuation due to absortpion corresponding to the imaginary part of the refractive index, which varies for each component of the sample. This attentuation generates contrast within the transmitted beam, producing an image of the sample on the detector. As presented in Fig. 5.1, small source size is desirable for increased spatial resolution, as well as sufficient radiation exposure. Absorption contrast imaging with high contrast is however limited to dense tissues, for example bone tissue. Contrast can be enhanced with radioopaque and radiolucent agents in living soft tissue through invasive applications [80]. We expect that our Betatron X-ray source with photon flux greater than 10^9 photons / 0.1% BW with micron scale source size and critical energy tunable beyond 10 keV should provide sufficient brightness and resolution for single shot image acquisition.

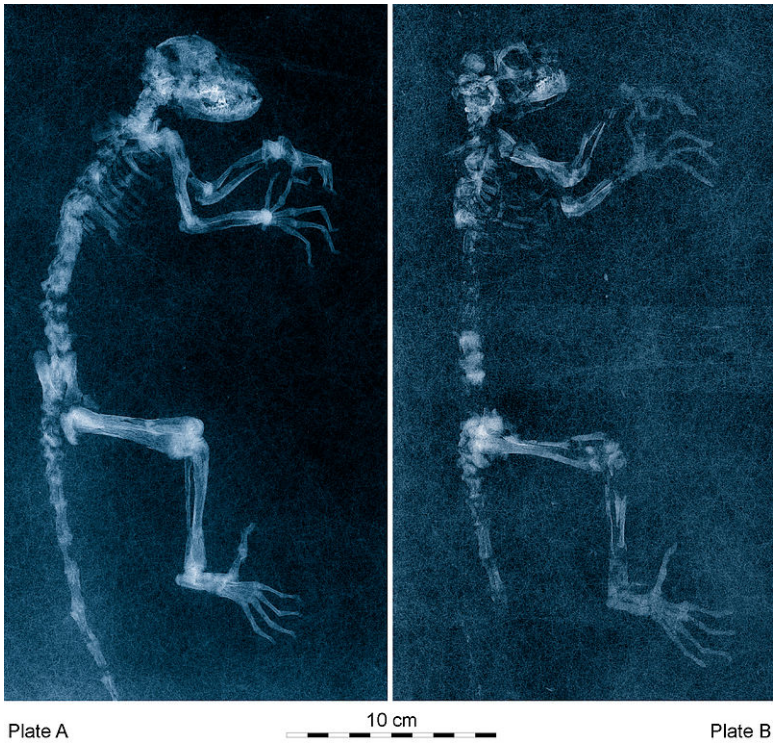

Figure 5.2: Radiography imaging used in paleontology. Radiographs of two specimen of Darwinius masillae. Reprinted from [80].

5.2 Phase-Contrast Imaging

The small source size of Betatron X-ray radiation makes it an ideal tool for X-ray Phase-Contrast Imaging (XPCI). This technique utilizes the spatial coherence of the small source for much improved resolution and image quality compared to standard absorption radiography [81]. While absorption contrast imaging relies on differences of absorption coefficient in different components of the sample, phase contrast imaging relies on the differences of refractive index within the sample, causing bending of the wavefront. Phase contrast imaging therefore sidesteps the need for radioopaque agents to visualize soft tissue. Dosage can be also reduced with XPCI compared to standard radiography by using harder X-rays [82]. XPCI has been alredy realized with a Betatron X-ray source in many cases [81] [82] [83]. Results of [81] are shown in Fig. 5.3, where the Betatron source had critical energy of 10 keV. To detect disturbanes within the wavefront properly, the X-ray source requires excellent spatial coherence. We will give a simple estimate for the transverse coherence length of our source from the properties of Fourier transform, since $\Delta \boldsymbol{x} \cdot \Delta \boldsymbol{k} \geq 1/2$. If the relative spectral bandwidth of the source $\Delta\lambda/\lambda = \Delta k/k$ is small, then the uncertainity in wavevector is mostly due to uncertainity in direction θ, which means $\Delta k = k\Delta\theta$. The radiation occupies the smallest phase space volume when equality is reached. Physically, that means that source size is indiscernable beyond the value set by the inequality. If we identify the source diameter as $d = 2\Delta x$, and the divergence half-angle θ with the uncertainity in direction $\Delta\theta$, as shown in Fig. 5.5, we have the condition for a spatially coherent source given as

$$\boxed{d \cdot \theta = \lambda/2\pi} \tag{5.2}$$

Radiation satisfying (5.2) is said to be *diffraction limited*. At some propagation distance z from the source, the transverse coherence length is $L_{transverse} = z\theta$, where the angle is set by (5.2). Phase-contrast imaging can be implemented in free-space propagation, crystal analyser-based and crystal or grating interferometer based techniques [84]. Free-space propagation is the often chosen and easiest technique for microscopy applications with micron scale resolution, with the only requirement being that the transverse coherence length at detector satisfies [84]

$$L_{transverse} \geq 2\sqrt{\frac{\lambda D}{2}} \tag{5.3}$$

where $D = a \cdot b/(a + b)$ is the defocusing distance with a being the source-sample distance and b being the sample-detector distance. Acquistion of projected X-ray phase contrast images with a Betatron X-ray source has been also realized in a tomographic setting, which allowed for 3D reconstruction of trabecular bone sample, as presented in Fig. 5.4. These results suggest that our micron scale Betatron source should be viable for XPCI.

Figure 5.3: X-ray absorption contrast image of an orange tetra fish (a) and damselfly (b). X-ray phase contrast image of a damselfly (c) and a yellow jacket (d). Reprinted from [81].

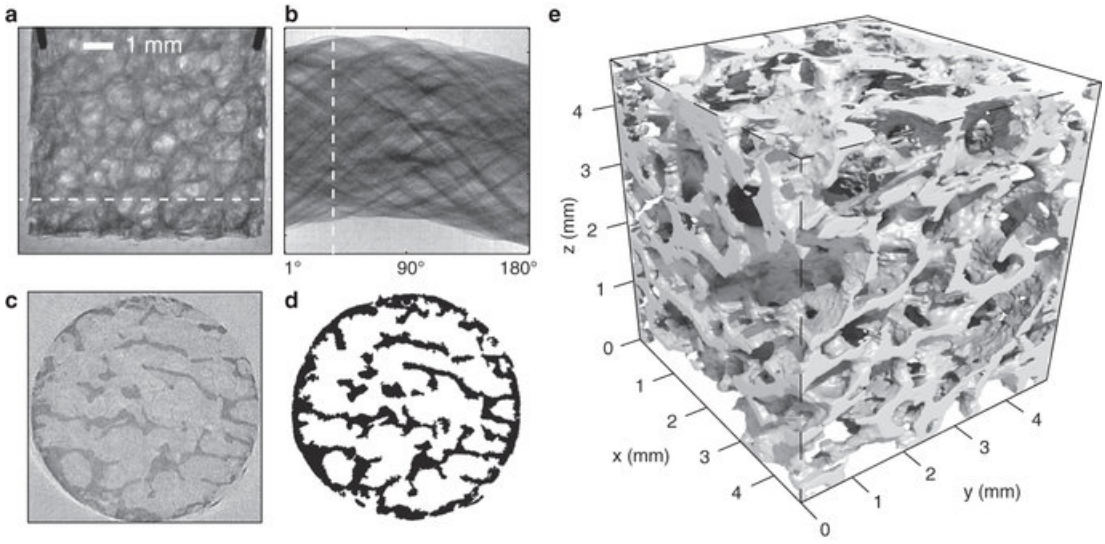

Figure 5.4: Tomographic reconstruction of a trabecular bone sample. (a) Raw image recorded on X-ray camera. (b) A sinogram of a particular row in the image, generated by stitching together 180 images at 1 degree intervals. (c) Application of inverse Radon transform to the sinogram in (b) generates a 2D reconstruction of a one-pixel horizontal slice of the sample. (d) Classification of pixels as bone (black) or vacuum (white). (e) 3D voxel map of the bone sample obtained by stacking together 1300 slices. Reprinted from [83].

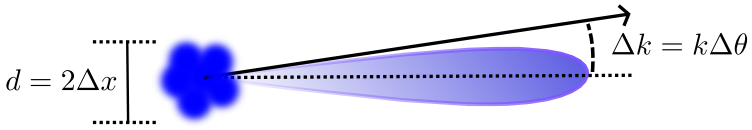

Figure 5.5: A schematic for the derivation of condition for diffraction limited radiation based on Fourier transform properties.

5.3 Ghost Imaging

Ghost imaging, also known as two-photon or correlated-photon imaging [85], was first realized in 1995 with visible light [86]. Ghost imaging has a rich history of research [86], [87], [85]. In this method, image is produced through measurement of second degree (intensity) correlation function. Setup of first realization of pure quantum ghost imaging with two entangled photons of visible light produced through parametric down-conversion [86] is shown in Fig. 5.6.

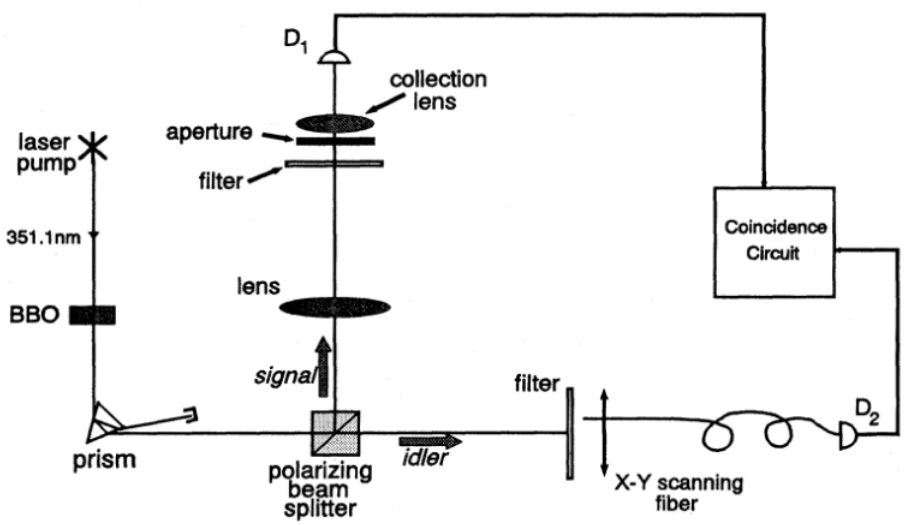

Figure 5.6: Experimental setup for quantum ghost imaging. Reprinted from [86].

In this scheme, a laser photon is converted through parametric down conversion in a BBO crystal into two photons of lower energy, *signal* and *idler*. Signal continues down one arm of the experimental setup to interact with the sample (aperture in Fig. 5.6) and is then collected by the single pixel detector D_1. Idler is sent onto a multi-pixel detector D_2, which records both spatial position and intensity. Coincidence circuit calculates the intensity correlation which produces the "ghost" image, which is produced due to the known location and intensity of *idler*, known intensity of *signal* and their spatial correlation. This works only if signal and idler are correlated, otherwise no image will be resolved. Since the first realization, there have been many advances in ghost imaging, which is now realized in both quantum and classical settings. In the quantum setting, the correlation is a result of the conservation of energy and momentum of the photon pair generated, for example in down-conversion. In a classical setting, spatial correlations are for example introduced by creating a random speckle pattern in the beam profile as shown in Fig. 5.7. There is also computational ghost imaging, where we pre-record the speckled patterns in the idler arm, eliminating it completely from the setup during imaging of the object, as shown in Fig. 5.8. Within the quantum regime, high efficiency CCDs allow for sub shot noise imaging below the diffraction limit [88].

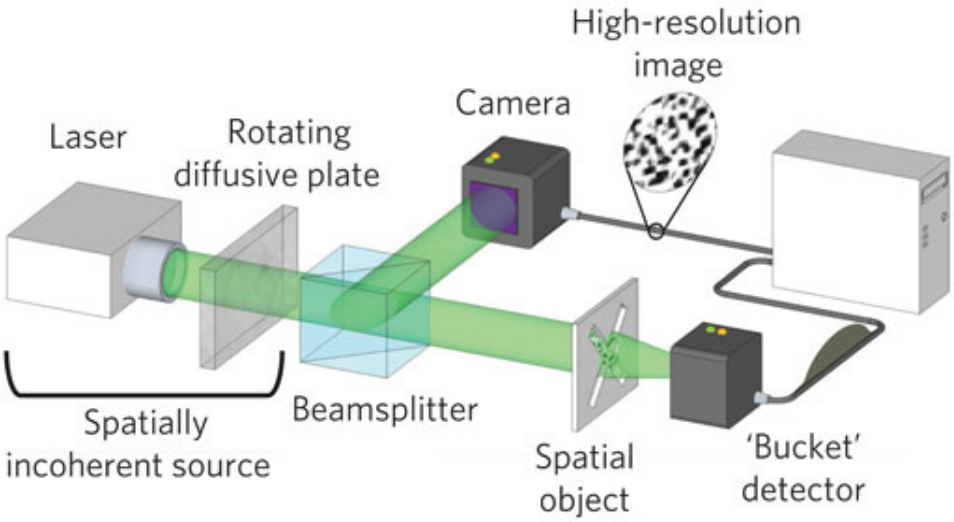

Figure 5.7: Experimental setup for classical ghost imaging where correlations are produced in the beam profile by a rotating diffuser. Reprinted from [89].

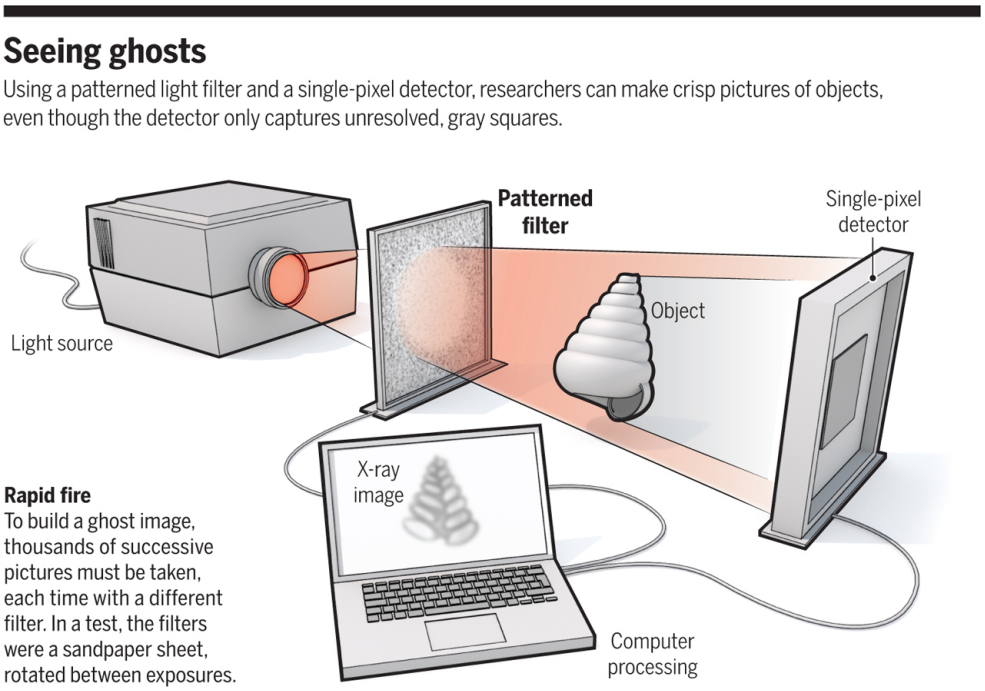

Figure 5.8: Experimental setup for classical computational X-ray ghost imaging where speckled beam is pre-recorded with a set of patterned filters, eliminating the need for expensive X-ray CCDs and optics for the user. Illustration by C. Bickel for article *Seeing Ghosts* in *sciencemag.org*

While there is great interest for these features within the X-ray imaging community, X-ray ghost imaging is still in it's infancy with great scope for optimization and further development [90]. It was recently shown that X-ray ghost imaging could potentially significantly reduce costs of X-ray imaging within a compact tabletop imaging setting, while also significantly reducing radiation exposure in biological samples [90]. Currently, the biggest issue with X-ray ghost imaging lies in producing a suitable beam splitter. Bragg or Laue diffraction in

crystals is often used, treating one of the diffracted beams as a separate path, however there is often loss of intensity due to absorption and the split is not 50/50, further reducing image quality [91]. Recent development of kinoform X-ray beam splitters may be used for ghost imaging in the future [91], [92]. Sharing most features with Synchrotron sources, Betatron source could potentially be used for X-ray ghost imaging. Excellent spatial coherence of the source could also be used for phase sensitive X-ray ghost imaging, which is a method that is currently being researched [93].

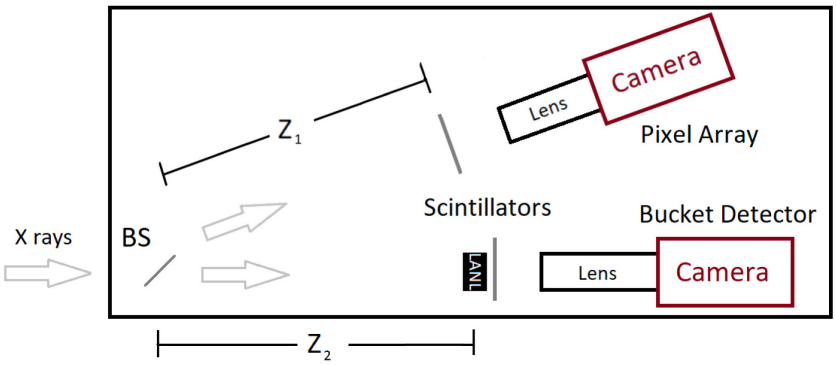

Figure 5.9: Setup for X-ray ghost imaging with a thermal X-ray source, like Betatron or Synchrotron radiation, with crystals serving as beamsplitters and short decay time scintillators with cameras for high-repetition operation. The sample aperture "LANL" is not seen by the pixel array camera. Reprinted from [91].

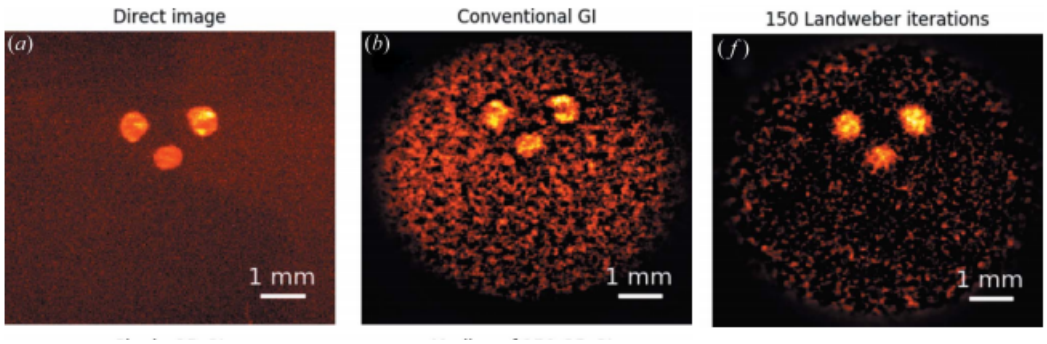

Figure 5.10: X-ray ghost imaging with a synchrotron source. (a) Direct image of the sample when illuminated by speckled X-ray beam. (b) Ghost image produced with 5000 measurements. (f) Image refined with 150 Landweber iterations. Reprinted from [90].

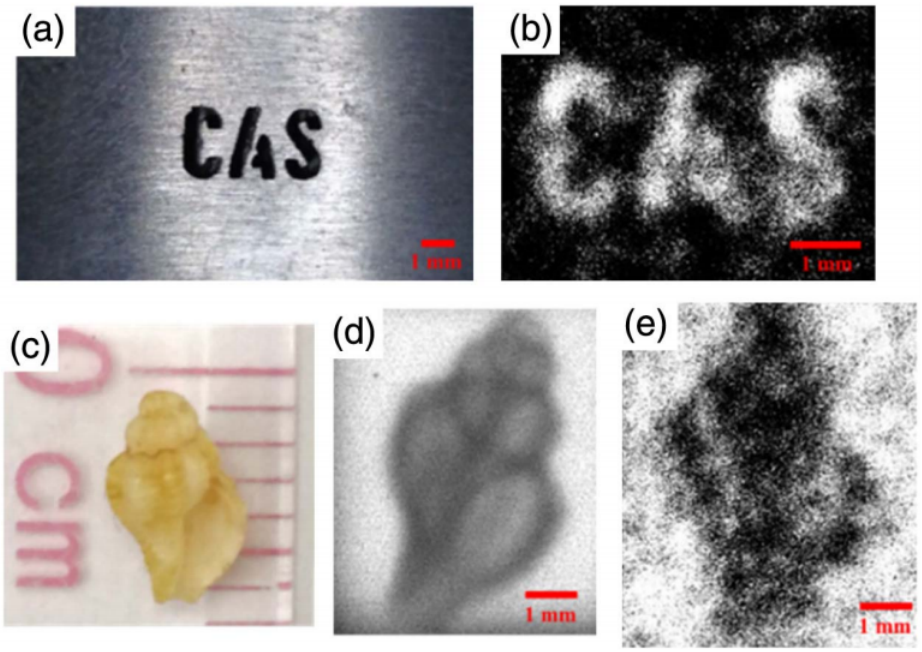

Figure 5.11: X-ray ghost imaging with realized with X-ray tube. (a) Direct photo of the "CAS" sample. (b) Ghost image of the "CAS" sample for 10^4 exposures. (c) Photo of a shell. (d) Projection X-ray image of the shell taken with CCD under 10 s exposure. (e) Ghost image of the shell for 10^4 exposures. Reprinted from [94].

Conclusion

In this thesis, I have presented a summary of literature and theory on radiation from relativistic laser wakefield accelerated electrons in **Chapters 1** and **2**. In **Chapter 3**, I have presented our work on numerical simulation and calculation of radiation emitted by these electrons. I have predicted that for a laser pulse with $a_0 = 4$, $\lambda_L = 0.808$ μm, $\tau_{(1/e)} = 28$ fs, $w_0 = 14$ μm interacting with a homogeneous gas target with density $n_0 = 5{\cdot}10^{18}$ cm^{-3}, we can expect broadband X-ray radiation with photon flux of $N_\gamma \doteq 2.4{\cdot}10^{11}$ photons per shot with energies extending up to 150 keV with pulse duration of $\tau \approx 30$ fs, beam divergence of 50 mrad and source size less than 10 mrad. Subsequently, I have predicted that interaction of the same laser pulse with gas target of density $n_0 = 10^{19}$ cm^{-3} will result in broadband X-ray radiation with photon flux of $N_\gamma \doteq 1.6 \cdot 10^{12}$ photons per shot with energies extending up to 200 keV with pulse duration of $\tau \approx 65$ fs, beam divergence of 100 mrad and source size less than 7 μm. In **Chapter 4**, I have presented experimental design, of which I was a part of, for the upcoming experiment with the L3 laser system at ELI Beamlines. In the last **Chapter 5**, I have presented currently employed X-ray imaging techniques and their requirements, concluding that the X-ray Betatron source generated with the L3 laser system will be a viable source for these imaging methods.

The numerical results within this thesis further motivate towards full 3D PIC simulations to quantitatively analyze total charge and energy of accelerated electrons and to account for subtleties arising in 3D space. Following experimental results of [57], [58], it seems that there is an increasing desire for both theoretical and experimental exploration of non-trivial target geometries and gas density distributions due to their potential for X-ray generation enhancement with improved shot-to-shot stability. One of the goals of future study should be to consider various laser and non-homogeneous gas target simulation setups to pave road for future experiments involving Betatron X-ray generation in advanced setups.

Bibliography

[1] ATLAS Collaboration. Observation of a new particle in the search for the standard model higgs boson with the ATLAS detector at the LHC. *Phys. Lett. B.*, 716:1–29, 2012.

[2] T. Feder. Accelerator school travels university circuit. *Phys. Today*, 63:20–22, 2010.

[3] Wilhelm Conrad Roentgen. Ueber eine neue Art von Strahlen. *Sitzungsberichte der Wuerzburger Physik.-Medic.-Gesellschaft*, 1895.

[4] William D. Coolidge. A powerful Röntgen ray tube with a pure electron discharge. *Physical Review*, 2:1–22, 1913.

[5] D. Iwanenko and I. Pomeranchuk. On the Maximal Energy Attainable in a Betatron. *Phys. Rev.*, 65:343–343, Jun 1944.

[6] R. Widerøe. Uber ein neues Prinzip zur Herstellung hoher Spannungen. *Arch. Elektrotech.*, 21:387–406, 1928.

[7] Ernest O. Lawrence and M. Stanley Livingston. The Production of High Speed Light Ions Without the Use of High Voltages. *Phys. Rev.*, 40:19–35, Apr 1932.

[8] D. W. Kerst. Acceleration of Electrons by Magnetic Induction. *Phys. Rev.*, 58:841–841, Nov 1940.

[9] Massachusetts Springfield. Radio-Craft. *Radcraft Publications*, 18:23, June 1947.

[10] McGraw-Hill Publishing Co. Electronics magazine. *New York*, 18:22, February 1942.

[11] V. I. Veksler. A new method of accelerating relativistic particles. *Comptes Rendus (Dokaldy) de l'Academie Sciences de l'URSS*, 43:329–331, 1944.

[12] E. M. McMillan. The Synchrotron – A Proposed High Energy Accelerator. *Phys. Rev.*, 68, 1945.

[13] J. Schwinger. On Radiation by Electrons in a Betatron. *World Scientific Series in 20th Century Physics — A Quantum Legacy*, pages 307–331, 2000.

[14] J. Schwinger. On The Classical Radiation of Accelerated Electrons. *Phys. Rev.*, 68, 1945.

[15] F. R. Elder, A. M. Gurewitsch, R. V. Langmuir, and H. C. Pollock. Radiation from Electrons in a Synchrotron. *Phys. Rev.*, 71:829–830, Jun 1947.

[16] John M. J. Madey. Stimulated Emission of Bremmstrahlung in a Periodic Magnetic Field. *Journal of Applied Physics*, 42:1906, 1971.

[17] Jr. S. Humphries. *Principles of Charged Particle Acceleration*. John Wiley and Sons, 1999.

[18] V. I. Veksler. Proc. CERN Symp. *FIAN Reports*, 80, 1951, 1952.

[19] Ya. B. Fainberg. Acceleration of Charged Particles in a Plasma. *Usp. Fiz. Nauk*, 93:617–631, Dec 1967.

[20] T. Tajima and J. M. Dawson. Laser Electron Accelerator. *Phys. Rev. Lett.*, 43:267–270, Jul 1979.

[21] A. Gonsalves et al. Petawatt Laser Guiding and Electron Beam Acceleration to 8 GeV in a Laser-Heated Capillary Discharge Waveguide. *Physical Review Letters*, 122, 02 2019.

[22] A. Rousse et al. Production of a keV X-ray Beam from Synchrotron Radiation in Relativistic Laser-Plasma Interaction. *Physical Review Letters*, 93:1–4, 2004.

[23] E. Esarey et al. Synchrotron radiation from electron beams in plasma-focusing channels. *Physical Review E., pages = 056505*, 65, 2002.

[24] S. Fourmaux et al. Demonstration of the synchrotron-type spectrum of laser-produced Betatron radiation. *New Journal of Physics*, 13, 2011.

[25] L. M. Chen et al. Bright betatron X-ray radiation from a laser-driven clustering gas target. *Sci. Rep.*, 3:1912, 2013.

[26] Wenchao Yan et al. Concurrence of monoenergetic electron beams and bright X-rays from an evolving laser-plasma bubble. *PNAS*, 111:5825–5830, 2014.

[27] J. Faure et al. Controlled injection and acceleration of electrons in plasma wakefields by colliding laser pulses. *Nature*, 444:737, 2006.

[28] John David Jackson. *Classical Electrodynamics*. Wiley, New York, 3rd ed. edition, 1999.

[29] Peter Mulser and Dieter Bauer. *High Power Laser-Matter Interaction*. Springer, 2010.

[30] J. Larmor. Proc. 5th. Int. Congress of Mathematics 1. *Cambridge 1913*, page 197, 1912.

[31] P. A. M. Dirac. Classical Theory of Radiation Reaction. *Fortschr. Phys.*, 9:343–392, 1961.

[32] D. A. Burton and A. Noble. Aspects of elecrtomagnetic radiation reaction in strong fields. *Contemp. Phys.*, 55:110–121, 2014.

[33] L. D. Landau and E. M. Lifshitz. *The Course of Theoretical Physics*. Butterworth-Heinemann, 2nd volume edition, 1987.

[34] A. Di. Piazza. Exact solution of the Landau-Lifshitz equation in a plane wave. *Lett. Math. Phys.*, 83:305–313, 2008.

[35] A. Macchi. *A Superintense Laser-Plasma Interaction Theory Primer*. Springer Netherlands, 2013.

[36] Anton Ilderton and Greger Torgrimsson. Radiation reaction in strong field QED. *Physics Letters B*, 725(4):481 – 486, 2013.

[37] Shen C. S. and White D. Energy straggling and radiation reaction for magnetic bremmstrahlung. *Phys. Rev. Lett.*, 28:455–459, 1972.

[38] Chiuderi C. and Velli M. *Basics of Plasma Astrophysics*. Springer, 2015.

[39] L. V. Keldysh. Ionization in the field of a strong electromagnetic wave. *Sov. Phys. JETP*, 20:1307–1314, 1965.

[40] Cheng Jin. *Introduction to High-Order Harmonics*. Springer, Cham, 2013.

[41] E. Esarey, P. Sprangle, and A. Ting. The Overview of Plasma-based Accelerator Concept. *IEEE Trans. Plasma Science*, 24:252, 1996.

[42] J. Faure et al. Effects of pulse duration on self-focusing of ultra-short lasers in under-dense plasmas. *Phys. Plasmas*, 9:756–759, 2002.

[43] J. Faure et al. Observation of laser-pulse shortening in nonlinear plasma waves. *Phys. Rev. Lett.*, 95:205003, 2005.

[44] C. D. Murphy et al. Evidence of photon acceleration by laser wake fields. *Physics of Plasmas*, 13:033108, 2006.

[45] J. Schreiber et al. Complete temporal characterization of assymetric pulse compression in a laser wakefield. *Phys. Rev. Lett.*, 105:235003, 2010.

[46] R. Duclous et al. Monte Carlo calculations of pair production in high-intensity laser-plasma interactions. *Plasma Phys. Control. Fusion*, 53:015009, 2011.

[47] C. P. Ridgers et al. Modelling gamma-ray photon emission and pair production in high-intensity laser-matter interactions. *Journal of Comp. Phys.*, 260:273–285, 2014.

[48] G. Genoud. Laser-driven plasma waves for particle acceleration and X-ray production. *Lund University, Sweden*, PhD thesis, 2011.

[49] A. I. Akhiezer et al. Theory of Wave Motion of an Electron Plasma. *JETP Lett.*, 3:696–705, 1956.

[50] W. Lu and M. Tzoufras et al. Generating Multi-GeV electron bunches using single stage laser wakefield acceleration in a 3d nonlinear regime. *Phys. Rev. ST Accel. Beams*, 10:061301, 2007.

[51] E. Esarey et al. Trapping and acceleration in nonlinear plasma waves. *Phys. Plasmas*, 2:1432, 1995.

[52] F. S. Tsung et al. Near-GeV-energy laser-wakefield acceleration of self-injected electrons in a centimeter-scale plasma channel. *Phys. Rev. Lett.*, 93:1–4, 2004.

[53] S. P. D. Mangles et al. Self-injection threshold in self-guided laser wakefield accelerators. *Phys. Rev. ST Accel. Beams*, 15:011302, 2012.

[54] A. Modena et al. Electron acceleration from the breaking of relativistic plasma waves. *Nature*, 377:606, 1995.

[55] A. Pak et al. Injection and trapping of tunnel-ionized electrons into laser-produced wakes. *Phys. Rev. Lett.*, 104:737, 2010.

[56] Thaury C., Guillaume E., Lifschitz. A., Phuoc K., K.T. Hansson, M. Grittani, and Malka V. Shock-assisted ionization injection in laser-plasma accelerators. *Scientific Reports*, 5:16310, 2015.

[57] Kozlova M., Andriyash I., Gautier J., Sebba S., Smartsev S., Jourdain N., and Oubreire K. Hard X-rays from Laser-Wakefield Accelerators in Density Tailored Plasmas. *Physical Review X*, 10:16310, 2020.

[58] M. Hansson et al. Down-ramp injection and independently controlled acceleration of electrons in a tailored laser wakefield accelerator. *Physical Review Special Topics - Accelerators and Beams*, 18:071303, 2015.

[59] D. Atwood and A. Sakdinawat. X-rays and extreme ultraviolet radiation. 2017.

[60] A. G. R. Thomas. Algorithm for calculating spectral intensity due to charged particles in arbitrary motion. *Phys. Rev. ST Accel. Beams*, 13:020702, 2010.

[61] D. F. Alferov, Yu. A. Bashmakov, and E. G. Bessonov. Undulator Radiation. *Tech. Phys.*, 18:1336–1339, 1974.

[62] T. Kerepecky. Inverse Compton scattering by laser-accelerated electrons. *Master Thesis, Czech Technical University*, 2017.

[63] J. P. Verboncoeur. Particle simulation of plasmas: review and advances. *Plamsa Physics and Controlled Fusion*, 47:A231, 2005.

[64] C. K. Birdsall and A. B. Langdon. *Plasma Physics via Computer Simulation. Series in Plasma Physics.* CRC Press, 2004.

[65] R. W. Hockney and J. W. Eastwood. *Computer Simulaton Using Particles.* CRC Press, 2010.

[66] J. W. Eastwood. The virtual particle electromagnetic particle-mesh method. *Computer Physics Communications*, 64:252–266, 1991.

[67] K. Yee. Numerical solution of initial boundary value problems involving Maxwell's equations in isotropic media. *IEEE Transactions on Antennas and Propagation*, 14, 1966.

[68] J. P. Boris. Relativistic plasma simulation-optimization of a hybrid code. *Proc. Fourth Conf. Num. Sim. Plasmas, Naval Res. Lab, Wash. DC.*, pages 3–67, 1970.

[69] R. Courant. On the partial difference equations of mathematical physics. *IBM J. Res. Dev.*, 11:215–234, 1967.

[70] C. E. Shannon. Communcation in the presence of noise. *Proceedings of the IRE*, 37:10–21, 1949.

[71] S. Corde et al. Femtosecond x-rays from laser-plasma accelerators. *Reviews of Modern Physics*, 85, 2013.

[72] Burnett et al. Atoms in ultra-intense laser fields. *Journal of Physics B: Atomic, Molecular and Optical Physics*, 4, 1993.

[73] S. Sinigardi, J. Babaei, and G. Turchetti. TNSA proton maximum energy laws for 2D and 3D PIC simulations. *Nuclear Instruments and Methods in Physics Research Section A: Accelerators, Spectrometers, Detectors and Associated Equipment*, 909:438–440, 2018.

[74] S. Fourmaux, E. Hallin, U. Chaulagain, S. Weber, and J. C. Kieffer. Laser-based synchrotron X-ray radiation experimental scaling. *Optics Express*, 28:3147–3158, 2020.

[75] S. Weber et al. P3: An installation for high-energy density plasma physics and ultra-high intensity laser–matter interaction at ELI-Beamlines. *Matter and Radiation at Extremes*, 2:149–176, 2017.

[76] S. Cipiccia et al. Gamma-rays from harmonically resonant betatron oscillations in a plasma wake. *Nature Physics*, 7:867–871, 2011.

[77] Wang et al. Quasi-monoenergetic laser-plasma acceleration of electrons to 2 GeV. *Nature Communications*, 4, 2013.

[78] Chaulagain U., Boháček K., Vančura J., Lamač M., Yan W., Gu Y., and Nejdl J. LWFA-Driven Betatron Source for Plasma Physics Platform at ELI Beamlines. *International Conference on X-ray Lasers, Springer, Cham*, 28:117–123, 2018.

[79] Collin Nave. A comparison of absorption and phase contrast for X-ray imaging of biological cells. *Journal of Synchrotron Radiation*, 25:1490–1504, 2018.

[80] Jens L. Franzen et al. Complete Primate Skeleton from the Middle Eocene of Messel in Germany: Morphology and Paleobiology. *PLOS One*, 2009.

[81] S. Kneip et al. X-ray phase contrast imaging of biological specimens with femtosecond pulses of betatron radiation from a compact laser plasma wakefield accelerator. *Applied Physics Letters*, 99:093701, 2011.

[82] U. Chaulagain et al. X-ray phase contrast imaging of biological samples using a betatron X-ray source generated in a laser wakefield accelerator. *SPIE Proceedings Optics and Optoelectronics, Prague*, 10240, 2017.

[83] J. Cole et al. Laser-wakefield accelerators as hard x-ray sources for 3d medical imaging of human bone. *Scientific Reports*, 5:13244, 2015.

[84] J. Wenz and S. Schleede et al. Quantitative X-ray phase-contrast microtomography from a compact laser-driven betatron source. *Nature Communications*, 6, 2015.

[85] David S. Simon, Gregg Jaeger, and Alexander V. Sergienko. *Quantum Metrology, Imaging, and Communication*. Springer, 2016.

[86] T. B. Pittman, Y. H. Shih, D. V. Strekalov, and A. V. Sergienko. Optical imaging by means of two-photon quantum entanglement. *Phys. Rev. A*, 52, 1995.

[87] Yanhua Shih. The Physics of Ghost Imaging. *arXiv:0805.1166*, 2009.

[88] Marta Gilaberte Basset, Frank Setzpfandt, Fabian Steinlechner, Erik Beckert, Thomas Pertsch, and Markus Gräfe. Perspectives for Applications of Quantum Imaging. *Laser and Photonics Reviews*, 13, 2019.

[89] P. Ryczkowski, M. Barbier, Ari T. Friberg, John M. Dudley, and G. Genty. Ghost imaging in the time domain. *Nature Photonics*, 10:167–170, 2016.

[90] Pelliccia D., Olbinado Margie P., Rack Alexander, Kingston Andrew M., Myers Glenn R., and Paganin David M. Towards a practical implementation of X-ray ghost imaging with synchrotron light. *IUCrJ*, 5(4):428–438, Jul 2018.

[91] Thomas A. Smith, Yanhua Shih, Zhehui Wang, Xuan Li, Bernhard Adams, Marcel Demarteau, Robert Wagner, Junqi Xie, Lei Xia, Ren-Yuan Zhu, Liyuan Zhang, and Chen Hu. From optical to X-ray ghost imaging. *Nuclear Instruments and Methods in Physics Research Section A: Accelerators, Spectrometers, Detectors and Associated Equipment*, 935:173 – 177, 2019.

[92] M. Lebugle, G. Seniutinas, F. Marschall, V. A. Guzenko, D. Grolimund, and C. David. Tunable kinoform x-ray beam splitter. *Opt. Lett.*, 42(21):4327–4330, Nov 2017.

[93] Phase sensitive X-ray ghost imaging. *arXiv:1903.08345*.

[94] Ai-Xin Zhang, Yu-Hang He, Ling-An Wu, Li-Ming Chen, and Bing-Bing Wang. Tabletop x-ray ghost imaging with ultra-low radiation. *Optica*, 5(4):374–377, Apr 2018.

List of Figures

A. Appendix

A.1 Relativistic Euler-Lagrange equations

We can simplify the derivation of relativistc Euler-Lagrange equations by assuming that virtual world lines $x^{\mu *} = x^\mu + \delta x^\mu$ are, instead of their own proper times τ^*, all parametrized by the proper time of the real world line τ. This simplifies the variation of action, since then we have $\delta \mathbf{d}\tau = 0$ producing

$$\begin{aligned}
\delta S &= \int_{\tau_1}^{\tau_2} \delta\mathcal{L}\mathbf{d}\tau + \mathcal{L}\delta\mathbf{d}\tau = \int_{\tau_1}^{\tau_2} \left(\frac{\partial \mathcal{L}}{\partial x^\mu}\delta x^\mu + \frac{\partial \mathcal{L}}{\partial u^\mu}\delta u^\mu \right) \mathbf{d}\tau + 0 \\
&= \int_{\tau_1}^{\tau_2} \left(\frac{\partial \mathcal{L}}{\partial x^\mu}\delta x^\mu + \frac{\partial \mathcal{L}}{\partial u^\mu}\frac{\mathbf{d}\delta x^\mu}{\mathbf{d}\tau} \right) \mathbf{d}\tau = \int_{\tau_1}^{\tau_2} \left[\frac{\partial \mathcal{L}}{\partial x^\mu}\delta x^\mu - \frac{\mathbf{d}}{\mathbf{d}\tau}\left(\frac{\partial \mathcal{L}}{\partial u^\mu} \right) \delta x^\mu \right] \mathbf{d}\tau \\
&= \int_{\tau_1}^{\tau_2} \left[\frac{\partial \mathcal{L}}{\partial x^\mu} - \frac{\mathbf{d}}{\mathbf{d}\tau}\left(\frac{\partial \mathcal{L}}{\partial u^\mu} \right) \right] \delta x^\mu \mathbf{d}\tau = 0
\end{aligned}$$

Where we've used per partes in the fourth equality. Since the variation δx^μ is arbitrary, Hamilton's principle for the evolution in non-trivial time interval is given by the Euler-Lagrange equations

$$\frac{\partial \mathcal{L}}{\partial x^\mu} - \frac{\mathbf{d}}{\mathbf{d}\tau}\left(\frac{\partial \mathcal{L}}{\partial u^\mu} \right) = 0$$

As we've mentioned previously, u^μ is the four-velocity only along the real world line, therefore we can use the normalization of four-velocity $u^\mu u_\mu = -c^2$ only after substituting into the Euler-Lagrange equations.

A.2 Maxwell's Equations

Euler-Lagrange equations can be used to derive equations of motion for fields with infinite number of degrees of freedom, we simply have to consider the fields themselves as the canonical coordinates. This produces Euler-Lagrange equations in the form

$$\frac{\partial \mathcal{L}}{\partial A_\mu} - \partial_\mu \left[\frac{\partial \mathcal{L}}{\partial(\partial_\nu A_\mu)} \right] = 0$$

with the Minkowski metric $\eta_{\mu\nu} = \eta^{\mu\nu} = diag(-1, +1, +1, +1)$, the four-gradient is $\partial^\nu = \partial/\partial_\nu = (-\partial_t/c, \nabla)$ and therefore with the field Lagrangian density 1.7 we have for the derivatives

$$\frac{\partial \mathcal{L}}{\partial A_\nu} = J^\nu$$

and for the second term

$$\begin{aligned} \frac{\partial \mathcal{L}}{\partial(\partial_\nu A_\mu)} &= -\frac{1}{4\mu} \frac{\partial}{\partial_\nu A_\mu} \left(F_{\alpha\beta} \eta^{\alpha\lambda} \eta^{\beta\sigma} F_{\lambda\sigma} \right) \\ &= \frac{1}{4\mu} \eta^{\alpha\lambda} \eta^{\beta\sigma} \left[(F_{\lambda\sigma}(\delta^\nu_\alpha \delta^\mu_\beta - \delta^\nu_\beta \delta^\mu_\alpha) + F_{\alpha\beta}(\delta^\nu_\lambda \delta^\mu_\sigma - \delta^\nu_\sigma \delta^\mu_\lambda) \right] \\ &= \frac{F^{\mu\nu}}{\mu} \end{aligned}$$

where we've used the definition and anti-symmetry of the electromagnetic tensor in the third equality. Substituting into the Euler-Lagrange equations gives the first set of Maxwell's equations

$$\partial_\mu F^{\mu\nu} = \mu J^\nu \iff \nabla \times \boldsymbol{H} = \boldsymbol{J} + \frac{\partial \boldsymbol{D}}{\partial t} \ , \ \nabla \cdot \boldsymbol{D} = \rho$$

the two equations arise for $\mu = 0$ and $\mu = i$. The second set of source-less equations

$$F_{[\mu\nu,\rho]} = 0 \iff \nabla \times \boldsymbol{E} = -\frac{\partial \boldsymbol{B}}{\partial t} \ , \ \nabla \cdot \boldsymbol{B} = 0$$

these two equations arise for $\mu\nu\rho = 0jk$ and $\mu\nu\rho = 123$. They are produced identically due to the definition of electromagnetic tensor

$$F_{[\mu\nu,\rho]} = F_{\mu\nu,\rho} + F_{\rho\mu,\nu} + F_{\nu\rho,\mu} = A_{\nu,\mu\rho} - A_{\mu,\nu\rho} + A_{\mu,\rho\nu} - A_{\rho,\mu\nu} + A_{\rho,\nu\mu} - A_{\nu,\rho\mu} = 0$$

A.3 Lagrangian of a Free Particle

For the simplest Lagrangian of a free particle, we assumed a most logical choice where the particle is simply described by it's resting energy

$$\mathcal{L}_{free} = -m_0 c^2$$

where the sign of the Lagrangian is determined by the signature of the metric tensor. According to our comments in A.1, we can't use the normalization $u_\mu u^\mu = -c^2$ before we substitute into the E-L equations, which means that we can use this normalization only after we calculate the derivatives. For simplicity, we didn't want to trouble the kind reader with nuances of relativistic electrodynamics within the main text, so we will validate our results with a quick computation with the proper lagrangian

$$\mathcal{L}_{free} = -m_0 c\sqrt{-u_\mu u^\mu}$$

Substituting into the Euler-Lagrange equations, we get

$$\frac{\partial \mathcal{L}}{\partial u^\mu} = m_0 c \frac{u_\mu}{\sqrt{-u_\nu u^\nu}} = m_0 u_\mu = p_\mu$$

with the interacting term included $L_{int} = J^\mu A_\mu$, we get

$$\frac{\partial \mathcal{L}}{\partial u^\mu} = m_0 c \frac{u_\mu}{\sqrt{-u_\nu u^\nu}} + qA_\mu = m_0 u_\mu + qA_\mu = p_\mu + qA_\mu$$

where we have now correctly used the normalization $u_\mu u^\mu = -c^2$. For the second term

$$\frac{\partial \mathcal{L}}{\partial x^\mu} = qA_{\nu,\mu} u^\nu$$

substituting these results into the E-L equations produces the Lorentz force law result (1.11)

$$\frac{\mathbf{d}p_\mu}{\mathbf{d}\tau} = q(A_{\nu,\mu} - A_{\mu,\nu})u^\nu = qF_{\mu\nu}u^\nu$$

A.4 Derivation of Radiation Reaction Force

Let us assume that there is a radiation reaction force term $\mathcal{F}^{\mu}_{rr}$ describing the loss of energy-momentum due to emitted radiation, then the equations of motion become

$$\frac{\mathbf{d}p_{\mu}}{\mathbf{d}\tau} = qF_{\mu\nu}u^{\nu} + \mathcal{F}^{\mu}_{rr}$$

To derive the form of the radiation reaction term, let us first consider a scalar product of a general force term F^{μ} with four-velocity u^{ν}

$$\begin{aligned}\eta_{\mu\nu}F^{\mu}u^{\nu} &= \eta_{\mu\nu}\frac{\mathbf{d}p^{\mu}}{\mathbf{d}\tau}u^{\nu} = \eta_{\mu\nu}\frac{\mathbf{d}(m_0u^{\mu})}{\mathbf{d}\tau}u^{\nu} \\ &= \eta_{\mu\nu}\frac{\mathbf{d}m_0}{\mathbf{d}\tau}u^{\mu}u^{\nu} + \eta_{\mu\nu}m_0\frac{\mathbf{d}u^{\mu}}{\mathbf{d}\tau}u^{\nu} = -c^2\frac{\mathbf{d}m_0}{\mathbf{d}\tau} + \eta_{\mu\nu}m_0a^{\mu}u^{\nu} = -c^2\frac{\mathbf{d}m_0}{\mathbf{d}\tau}\end{aligned}$$

where we've used the fact that four-velocity and four-acceleration are orthogonal, since

$$0 = \frac{\mathbf{d}}{\mathbf{d}\tau}(-c^2) = \frac{\mathbf{d}}{\mathbf{d}\tau}(\eta_{\mu\nu}u^{\mu}u^{\nu}) = \eta_{\mu\nu}(a^{\mu}u^{\nu} + u^{\mu}a^{\nu}) = 2\eta_{\mu\nu}a^{\mu}u^{\nu}$$

these results tells us that unless the $F^{\mu}u_{\mu} = 0$, the rest mass of the particle will change. Geometrically, this means that four-velocity is parallel along a world line and since four-acceleration is it's rate of change, it is always orthogonal to it. We can therefore proceed with our derivation of the radiation reaction force by demanding that the force term $\mathcal{F}^{\mu}_{rr}$ is a tensor product of some general vector y^{μ} and the projecting tensor $P^{\mu\nu} = \eta^{\mu\nu} - u^{\mu}u^{\nu}/c^2$, which projects a four-vector to hyper-plane orthogonal to the four-velocity. To include the jerk dynamic of the radiation reaction, four-vector y^{μ} must be at least of the form

$$y^{\mu} = Au^{\mu} + B\frac{\mathbf{d}u^{\mu}}{\mathbf{d}\tau} + C\frac{\mathbf{d}^2u^{\mu}}{\mathbf{d}\tau^2}$$

We can set A = 0 due to orthogonality of u^{μ} to the projection tensor $P^{\mu\nu}$ within the force term. By shifting the term with B on left side of the equation of motion, we can renormalize the mass into the physically observable mass as $m = m_0 - B$. To reproduce the Larmor formula, the last constant must be $C = q^2/6\pi\epsilon_0c^3$. These conditions for the tensor product produce the final form of Abraham-Lorentz radiation reaction force as

$$\mathcal{F}^{\mu}_{rr} = \frac{q^2}{6\pi\epsilon_0c^3}\left(\frac{\mathbf{d}a^{\mu}}{\mathbf{d}\tau} + \frac{u^{\mu}}{c^2}(a^{\nu}a_{\nu})\right)$$

A.5 Four-Potential of a Point Charge

Here we evaluate the four-potential (2.4) for a point charge. The four-current term J^ν is given by (2.5) as

$$J^\nu(\boldsymbol{r},t) = (q\delta(\boldsymbol{r}-\boldsymbol{x}(t)), qc\boldsymbol{\beta}(t)\delta(\boldsymbol{r}-\boldsymbol{x}(t))) = B^\nu(t)\delta(\boldsymbol{r}-\boldsymbol{x}(t))$$

where we've defined the four-vector $B^\nu(t) = (q, qc\boldsymbol{\beta}(t))$. The four-potential is therefore

$$\begin{aligned} A^\nu(\boldsymbol{r},t) = \mu(G \star J^\nu) &= \frac{\mu}{4\pi}\int \frac{B^\nu(t')}{|\boldsymbol{r}-\boldsymbol{r'}|}\delta(\boldsymbol{r'}-\boldsymbol{x}(t'))\delta\left(t-t'-\frac{|\boldsymbol{r}-\boldsymbol{r}'|}{c}\right)\mathbf{d}t'\mathbf{d}^3r' \\ &= \frac{\mu}{4\pi}\int \frac{B^\nu(t')}{|\boldsymbol{r}-\boldsymbol{x}(t')|}\delta\left(t-t'-\frac{|\boldsymbol{r}-\boldsymbol{x}(t')|}{c}\right)\mathbf{d}t' \end{aligned}$$

The last integral can be evaluated if we note that for functions $f(t), g(t)$ we have the following equality

$$\int f(t')\delta(t-g(t'))\mathbf{d}t' = \int f(t'(g))\delta(t-g)\frac{\mathbf{d}t'}{\mathbf{d}g}\mathbf{d}g = \int \frac{f(t'(g))}{\dot{g}(t'(g))}\delta(t-g)\mathbf{d}g = \frac{f(t'(t))}{\dot{g}(t'(t))}$$

where we've used the fact that $\mathbf{d}t = \frac{\mathbf{d}t}{\mathbf{d}g}\mathbf{d}g = \frac{1}{\frac{\mathbf{d}g}{\mathbf{d}t}}\mathbf{d}g$. We recognize the functions $f(t), g(t)$ as

$$\begin{aligned} f(t) &= \frac{B^\nu(t)}{|\boldsymbol{r}-\boldsymbol{x}(t)|} = \frac{B^\nu(t)}{|\boldsymbol{R}|} \\ g(t) &= t + \frac{|\boldsymbol{r}-\boldsymbol{x}(t)|}{c} \\ \dot{g}(t) &= 1 - \boldsymbol{\beta}(t)\frac{\boldsymbol{r}-\boldsymbol{x}(t)}{|\boldsymbol{r}-\boldsymbol{x}(t)|} = 1 - \boldsymbol{\beta}\cdot\boldsymbol{n} \end{aligned}$$

where we've defined the distance between observer and particle $|\boldsymbol{R}| = |\boldsymbol{r}-\boldsymbol{x}(t)|$ and the direction towards observer $\boldsymbol{n} = \boldsymbol{R}/|\boldsymbol{R}|$. The four-potential therefore becomes

$$A^\nu(\boldsymbol{r},t) = \frac{\mu}{4\pi}\frac{B^\nu(t)}{|\boldsymbol{R}|(1-\boldsymbol{\beta}\cdot\boldsymbol{n})}$$

which encompasses the famous Liénard-Wiechert potentials (2.6) and (2.7).

A.6 Critical Frequency Dependence on Deflection Parameter

As we've shown in (2.34), the critical frequency for an electron travelling along bending trajectory with $K \gg 1$ is

$$\omega_c = \frac{3c}{2\rho}\gamma^3$$

where ρ is the local radius of curvature. We can calculate dependence of critical frequency on the deflection parameter K by simply calculating the radius of curvature of a sinusoidal trajectory of the form (2.26)

$$r = r_\beta \sin(\omega_\beta t) = \frac{K}{\gamma k_\beta}\sin(k_\beta z)$$

The second equality is simply following from the definition of deflection parameter K, which resulted for Betatron oscillations as (2.31). The formula for the radius of curvature is given as

$$\rho(z) = \left|\frac{[1 + r'^2(z)]^{3/2}}{r''(z)}\right| = \left|\frac{[1 + (K/\gamma)^2\cos^2(k_\beta z)]^{3/2}}{(Kk_\beta/\gamma)\sin(k_\beta z)}\right|$$

Since most radiation is emitted along the turning points, we are interested in the smallest radius of curvature. The minimum is attained at turning points satisfying $k_\beta z = \pi/2 + \pi Z$ where Z is a whole number, which gives the minimum radius of curvature as

$$\rho_{min} = \frac{\gamma}{Kk_\beta}$$

substituting into the critical frequency, we get the dependence on the deflection parameter K, generalized for any sinusoidal trajectory as

$$\omega_c = \frac{3}{2}K\gamma^3\omega_\beta$$